System Optimization and Performance Enhancement of Active Magnetic Regenerators

by

Reed Teyber
B.Eng., University of Victoria, 2015

A Dissertation Submitted in Partial Fulfillment of the
Requirements for the Degree of

DOCTOR OF PHILOSOPHY

in the Department of Mechanical Engineering

System Optimization and Performance Enhancement of Active Magnetic Regenerators

by

Reed Teyber
B.Eng., University of Victoria, 2015

Supervisory Committee

Dr. A. Rowe, Supervisor
(Department of Mechanical Engineering)

Dr. M. Akbari, Departmental Member
(Department of Mechanical Engineering)

Dr. P. Agathoklis, Outside Member
(Department of Electrical Engineering)

Supervisory Committee

Dr. A. Rowe, Supervisor
(Department of Mechanical Engineering)

Dr. M. Akbari, Departmental Member
(Department of Mechanical Engineering)

Dr. P. Agathoklis, Outside Member
(Department of Electrical Engineering)

ABSTRACT

Energy conversion devices using solid-state magnetocaloric materials have the potential to reduce energy consumption and mitigate environmental pollutants. To overcome the limited magnetic entropy change of magnetocaloric materials, magnetic refrigeration devices typically use the active magnetic regenerator (AMR) cycle. AMR devices have demonstrated promising performance, however costs must be reduced for broad market penetration. Although the magnet cost is of greatest importance for commercialization, literature has decoupled magnet design from AMR optimization. And while multilayered regenerators can improve performance without increasing cost, a number of questions remain unanswered as a result of the prohibitive parameter space.

This dissertation explores methods of improving AMR performance and decreasing cost both at the subsystem level, namely the magnetocaloric regenerator, fluid flow system and magnetic field source, and the device level by coupling the regenerator and magnet design problems in a cost optimization framework. To improve AMR performance, multilayered regenerators with second-order magnetocaloric materials are experimentally and numerically investigated, yielding insight on how individual layers behave and interact over a wide range of regenerator compositions and operating parameters. An efficient AMR modeling approach is presented where individual

layers are treated as cascaded AMR *elements*, and simulations are in excellent agreement with experiments. Insights from the computationally efficient model are used to inform device modifications, and a no-load temperature span of 40 K is measured in close proximity to the simulated optimum; one of the highest in literature.

To simultaneously decrease AMR costs, a permanent magnet optimization framework is explored that is conducive to nonlinear objectives and constraints. This is used to investigate the optimal design of permanent magnet structures with reduced rare-earth permanent magnet materials. The regenerator and magnet design problems are then coupled in a permanent magnet topology optimization to minimize the combined capital and operating costs of an AMR. The optimal magnetic field waveform and the optimal means of producing this waveform are simultaneously obtained. The lifetime ownership costs of the optimized AMR device are shown to be in the realm of existing entry-level cooling devices. The presented cost optimization framework is of interest to both scientists and engineers, and demonstrates the importance of fast AMR models in identifying system designs, regenerator compositions and operating regimes that increase AMR performance and decrease cost.

Contents

List of Tables

List of Figures

Nomenclature

Roman

B	magnetic flux density [T]
$\not{c}$	cost per unit exergy [$/kWh]
$\dot{C}_{\mathrm{Q}}$	cost rate of cooling [$/h]
C	specific heat [J/kg-K]
$\dot{E}x_{\mathrm{Q}}$	exergetic cooling power [W]
F	Helmholtz free energy [J/kg]
H	magnetic field strength [A/m]
M	magnetization [A/m]
$2p$	magnet poles [-]
$\dot{Q}$	cooling capacity or heat rejection [W]
R	radius [m]
s	entropy [J/kg-K]
T	temperature [K]
$\dot{W}$	work [W]
x	regenerator spatial coordinate [m]
Z	capital costs [$]

Greek

ϵ	passive regenerator effectiveness [-]
μ	magnetic permeability [H/m]
η_{II}	second law efficiency [-]

Subscripts and Superscripts

ad	adiabatic temperature change
app	applied field
C	cold reservoir or cold side
cj	intrinsic coercivity
f	final field
H	hot reservoir or hot side
HB	hot blow
high	high field
i	initial field
int	internal field
M	magnetic
MCM	magnetocaloric material
net	net work
PMM	permanent magnet material
rem	remanence
span	temperature span

ACKNOWLEDGEMENTS

I would like to thank:

Andrew Rowe, for being an outstanding supervisor. This dissertation would not have been possible without your ongoing support and inspiration. The opportunities you have created for me will always be remembered and appreciated.

Paulo Trevizoli, for being a friend and mentor. You taught me how to navigate a maze of information, and in doing so, showed me how to be a researcher.

My parents, Dr. Kathy Pezdek and Dr. Edward Teyber, for instilling curiosity and teaching me to always chase my dreams.

My wonderful girlfriend, Alyona Ivanova, for our wonderful years together and for your unwavering support.

Rodney Katz, for being a friend and mentor. Thank you for everything over the years.

Susan Walton and Pauline Shepherd, for your friendship and support.

The Cryofuels team, for the years of great memories.

Daniel Barrera-Medrano and Florian Scharf (BASF), for your friendship and support.

Jamelyn Holladay, John Barclay and Kerry Meinhardt (PNNL), for your friendship and support.

NSERC, for your financial support.

To my wonderful my parents, Dr. Kathy Pezdek and Dr. Edward Teyber

Chapter 1

Introduction

According to the U.S. Energy Information Administration's annual residential energy consumption survey [4], 40% of residential electricity is consumed for refrigeration, air conditioning and heating applications, where vapor compression devices have dominated the marketplace for over 100 years. Other estimates for OECD countries including North America and the European Union exceed 65% [5]. In the commercial sector, approximately 42% of energy is consumed for these services [6]. The Kigali agreement (2016), a recent ammendment to the Montreal Protocol, mandates the phase-out of hydrofluorocarbons (R134A, R404A, R507A, R410A) in addition to chlorofluorocarbons (R11, R12) and hydrochlorofluorocarbons (R22, R402A). Although this terminates the production of materials with strong ozone depletion and global warming potentials, the debate over refrigerant replacements is ongoing and unresolved [7, 8].

Hydrocarbons such as propane (R290), propene (R1270) and isobutane (R600a) are high-performance refrigerants with a low global warming potential [9, 5], however they are highly flammable and pose explosive safety concerns in the case of leaks or refrigerant contamination. Carbon dioxide has been reconsidered as a refrigerant, but its low boiling temperature requires high operating pressures that translate directly into increased costs [8]. Due to these concerns, hydrofluoroolefins (R1234YF) have taken the spotlight as a drop-in replacement for R134A; however, they are flammable, have higher global warming potential than hydrocarbons, are more expensive than existing offerings and reduce refrigeration performance [10, 8, 5].

Energy conversion devices using solid-state magnetocaloric materials have been attracting interest due to their potential to reduce energy consumption and mitigate environmental pollutants. In constrast with harmful fluorinated refrigerants, mag-

netic refrigeration devices can utilize water as a working fluid and operate in near silence. Although magnetic refrigeration devices have demonstrated commercially relevant performance, costs must be reduced for broad market penetration.

1.1 Magnetocaloric effect

Magnetic refrigeration utilizes the magnetocaloric effect; the reversible temperature increase of a magnetocaloric material upon application of a magnetic field [11, 12, 13, 14]. The magnetocaloric effect is driven by the entropy change of the electronic spin system as a function of the temperature, initial and final field, $\Delta s(T, H_i, H_f)$. Depending on the thermodynamic process, the magnetocaloric effect can manifest either as an adiabatic (isentropic) temperature change or an isothermal entropy change as shown in Fig. 1.1.

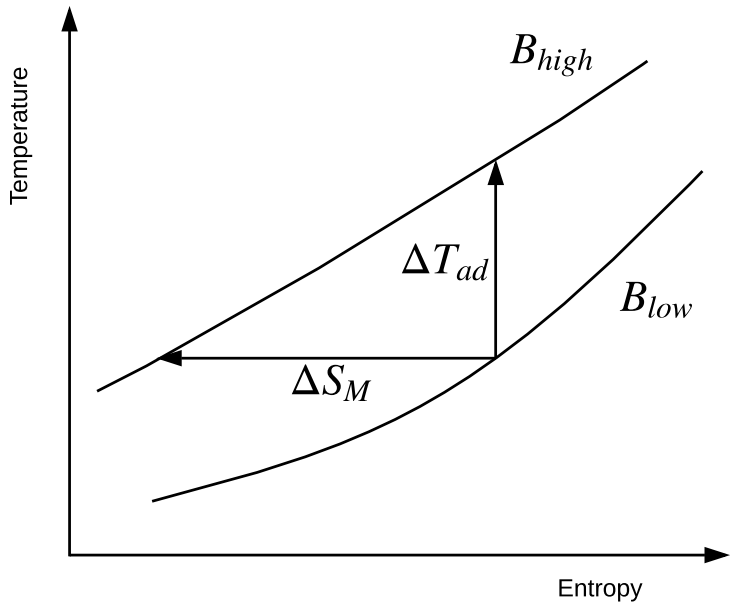

Figure 1.1: Manifestation of magnetocaloric effect as adiabatic temperature change or isothermal entropy change.

Consider first the isothermal entropy change. The differential of the free energy, F can be written as [12]:

$$dF = -SdT - \mu_0 MdH \tag{1.1}$$

As the second derivative $(\partial^2 F/\partial T \partial H)$ is independent of the order of differentia-

tion, the following Maxwell relation is found:

$$\left(\frac{\partial S}{\partial H}\right)_T = \mu_0 \left(\frac{\partial M}{\partial T}\right)_H \tag{1.2}$$

Integration leads to the entropy change upon application of a magnetic field:

$$\Delta S(T, H_i, H_f) = \mu_0 \int_{H_i}^{H_f} \left(\frac{\partial M}{\partial T}\right)_H dH \tag{1.3}$$

The reversible, adiabatic (i.e. isentropic) temperature change, $\Delta T_{ad}(T, H_i, H_f)$, can be found from the differential variation in entropy:

$$dS = 0 = \left(\frac{\partial S}{\partial T}\right)_H dT + \left(\frac{\partial S}{\partial H}\right)_T dH \tag{1.4}$$

Using the well-known thermodynamic relation:

$$\left(\frac{\partial S}{\partial T}\right)_H = \frac{C_H(T, H)}{T} \tag{1.5}$$

and the Maxwell relation above (Eq. 1.2) yields the adiabatic temperature change along an isentrope:

$$\Delta T_{ad}(T, H_i, H_f) = -\mu_0 \int_{H_i}^{H_f} \frac{T}{C_H(T, H)} \left(\frac{\partial M}{\partial T}\right)_H dH \tag{1.6}$$

The magnetocaloric effect is driven by a magnetization change ($\partial M/\partial T$) which is greatest across the ferromagnetic-paramagnetic phase transition defined as the Curie temperature. The adiabatic temperature change and isothermal entropy change can be derived from magnetization measurements as a function of temperature and applied field [12]. Alternatively, the magnetization can be derived from molecular mean field models. Further details on mean field theory (MFT) and the thermomagnetic properties used in the present dissertation are outlined in Appendix B.

1.2 Active Magnetic Regenerator

While the vapor-compression process creates considerable temperature spans, the magnetocaloric effect is on the order of several degrees Kelvin. The rare-earth element Gadolinium produces an adiabatic temperature change of only 3 K when the field is increased from 0 to 1 T [15]. To overcome the limited magnetic entropy change, magnetic refrigeration devices typically use the active magnetic regenerator (AMR) cycle which was first proposed and patented by Dr. John Barclay and Dr. William Steyert at Los Alamos National Laboratory in 1982 [16].

The AMR uses a magnetocaloric material as the solid matrix material in a thermal regenerator, where each differential section of the regenerator undergoes independent Brayton refrigeration cycles. A representative T-S diagram for a differential section of an AMR is shown in Fig. 1.2 (a). The cycle starts with magnetization, where increasing the applied field from B_{low} to B_{high} isentropically raises the solid temperature along all sections of the regenerator (ΔT_{ad}). The magnetization step is followed by a cold blow, where fluid is displaced from the cold end towards the hot end of the regenerator. In this process, the temperature is decreased in all sections of the regenerator. Removal of the applied field (demagnetization) causes the solid temperature to decrease to the corresponding isofield line (B_{low}). The subsequent hot blow displaces fluid through the cooled solid matrix towards the cold end, resulting in a refrigeration effect.

The AMR cycle is unique, however, in that each differential section of the regenerator undergoes independent Brayton refrigeration cycles. This is shown in Fig. 1.2 (b), where each differential section cools the previous section (x^-) and rejects heat to the following section (x^+). The cycle-averaged heat rejection from a section is determined from an energy balance ($\dot{Q}_H^{x^0} = \dot{Q}_C^{x^0} + \dot{W}_{net}^{x^0}$), where the net work consists of pump work from driving heat transfer fluid through a porous network and magnetic work from magnetizing and demagnetizing a magnetic material. Energy conservation between sections equates the heat rejection from a layer x^0 to the heat absorption of a following layer x^+ ($\dot{Q}_H^{x^0} = \dot{Q}_C^{x^+}$), illustrated in Fig. 1.2 (b), yielding cascaded magnetic brayton cycles producing temperature spans several times the adiabatic temperature change (ΔT_{ad}) of the magnetic refrigerant. While the AMR macroscopically operates as a conventional refrigerator (Fig. 1.2 (c)), absorbing heat from a cold thermal reservoir ($\dot{Q}_C, T_C$) and rejecting heat to room temperature ($\dot{Q}_H, T_H$) while consuming work ($\dot{W}_{net}$), it is a thermodynamically unique cycle with no direct analogy to

vapor-compression cycles.

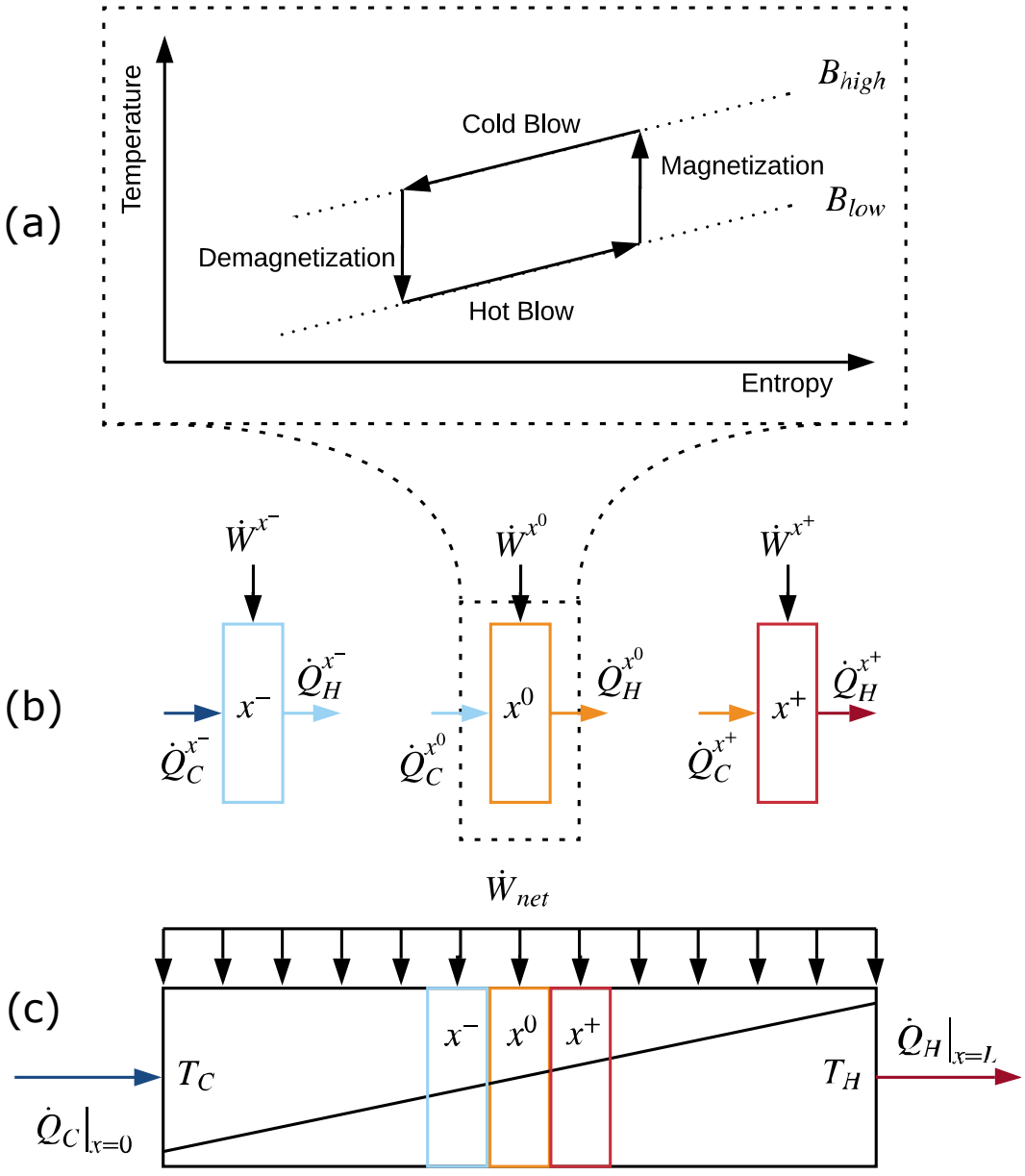

Figure 1.2: (a) Representative T-S diagram of magnetic Brayton refrigeration cycle. (b) Interaction of each differential regenerator section performing independent magnetic Brayton cycles. (c) AMR Macroscopic energy balance.

To perform the AMR cycle, a device is required consisting of a switchable magnetic field source, a fluid flow system and a regenerator consisting of porous magnetocaloric material. The general AMR device is depicted in Fig. 1.3, however a large number of configurations exist [17]. Having a general understanding of the AMR cycle, each component is discussed in an effort to identify a path to improved magnetic refrigeration devices.

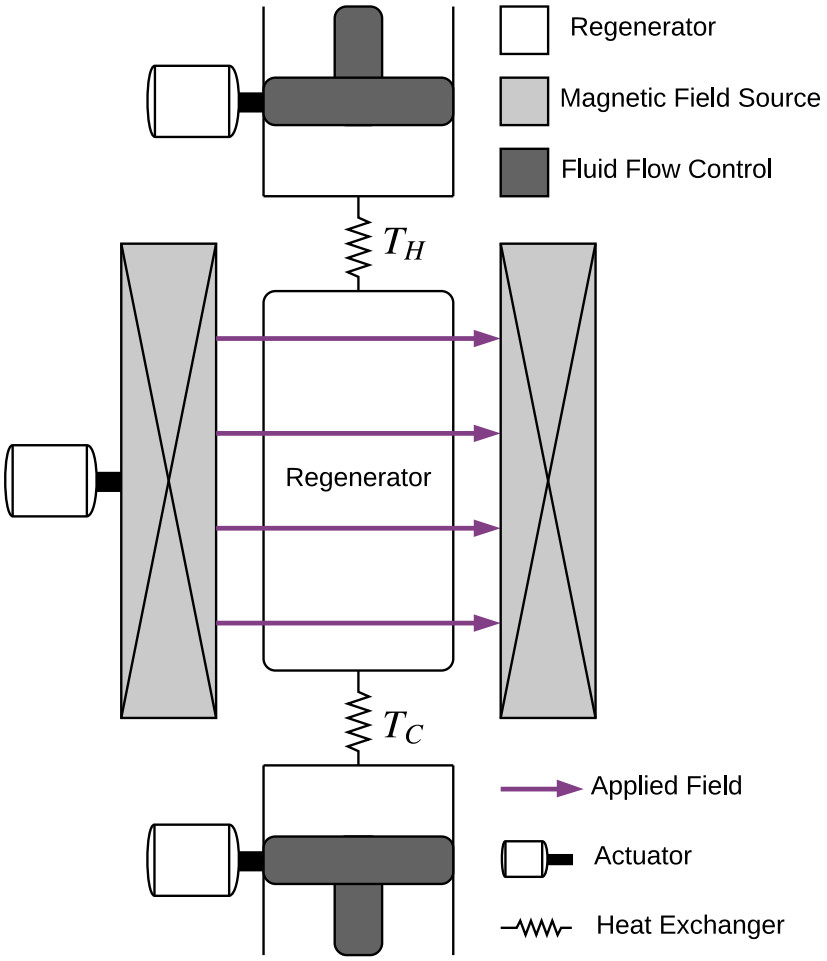

Figure 1.3: Generic depiction of AMR device showing magnetocaloric regenerator, magnetic field source and fluid flow system.

1.2.1 Regenerator

The regenerator consists of the magnetocaloric material in a porous structure in which heat transfer fluid is displaced. Packed spherical particles and parallel plates [18, 19], shown in Fig. 1.4 (a) and (c), are the most common regenerator matrices, however screens [20], pins [21] and 3D printed lattice structures (Fig. 1.4 (b)) are gathering increased interest. The best experimental results to date in regards to temperature span [22], cooling power [23] and efficiency [24] have been reported with packed spherical particles.

An *effective* regenerator is required to obtain high temperature spans. The passive regenerator effectiveness is a measure of the rate at which heat is transferred between the fluid and solid phases in a given blow. The hot-blow regenerator effectiveness is defined as [25]:

$$\epsilon = \frac{\dot{Q}_{HB}}{\dot{Q}_{max}} = 1 - \frac{\bar{T}_{HB} - T_C}{T_H - T_C} \tag{1.7}$$

Finite convection, heat transfer area and thermal mass result in regenerator *ineffectiveness* which manifests as a heat leak from the hot to the cold side [26] (Fig. 1.9 (c)). With small temperature spans, the heat transfer problem is less important as AMR performance is driven primarily by magnetocaloric mass and magnetic field strength. While the thermal-magnetic properties influence the effectiveness, it is overwhelmingly a thermal heat transfer problem which has been studied extensively due to regenerators broad application in catalytic reactors, cryogenics and energy storage applications. The dissertation of Trevizoli was dedicated to the development of thermal regenerators for magnetic cooling applications [27]. Efforts to maximize magnetic refrigeration efficiency and performance must incorporate regenerator geometries, heat transfer structures and operating parameters known to maximize regenerator effectiveness.

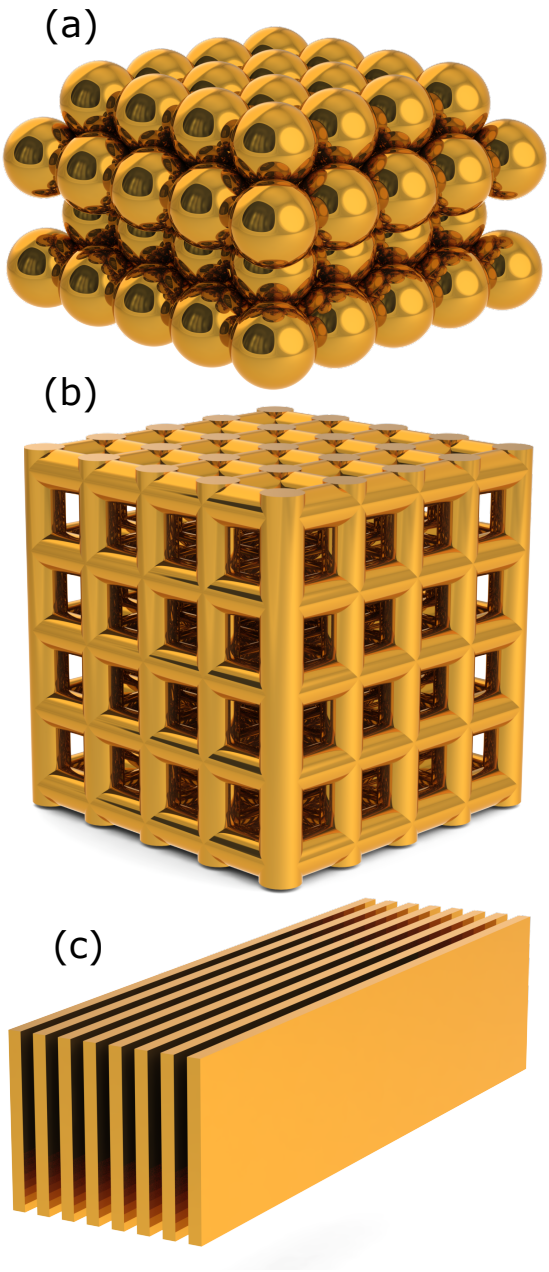

Figure 1.4: (a) Packed spherical, (b) 3-D printed lattice and (c) parallel plate regenerator matrices. Heat transfer fluid occupies void region around magnetocaloric material.

Multilayering

The magnetocaloric effect in real materials is a strong function of temperature and, as shown for gadolinium in Fig. 1.5, occurs only in a narrow region near the Curie temperature. This gives rise to the concept multilayering, where a regenerator is cascaded with ferromagnetic refrigerants of sequentially decreasing Curie temperature. Consider the illustrative example in Fig. 1.5, where a partitioned regenerator allows two different magnetocaloric materials to be packed. If the cold layer is replaced with a lower Curie temperature magnetocaloric material (e.g. replacing the red dashed line with the solid blue line), the average magnetocaloric effect is increased.

Although multilayering is conceptually simple, a number of issues remain unresolved [12, 14]. In the illustrative example above, the 40 K temperature span (T_{C}= 260 K, T_{H}= 300 K) requires a 20 K span across each layer. It is not guaranteed that the warm layer can produce this 20 K temperature span, and if it does not, the multilayered regenerator may under-perform the single layer regenerator. Furthermore, for regenerators consisting of many layers, it is uncertain how layer lengths and Curie temperatures should be distributed.

Multilayering requires numerical models capable of predicting the performance and interaction of individual layers as a function of the device configuration (e.g. magnetic field strength, regenerator geometry, matrix parameters, parasitic heat leaks) and operating parameters (e.g. device frequency, displaced fluid volume, heat rejection temperature). The ability to simultaneously optimize a regenerator composition and AMR device for targeted applications remains an area of ongoing research, and requires efficient AMR modeling tools capable of exploring the extensive parameter space.

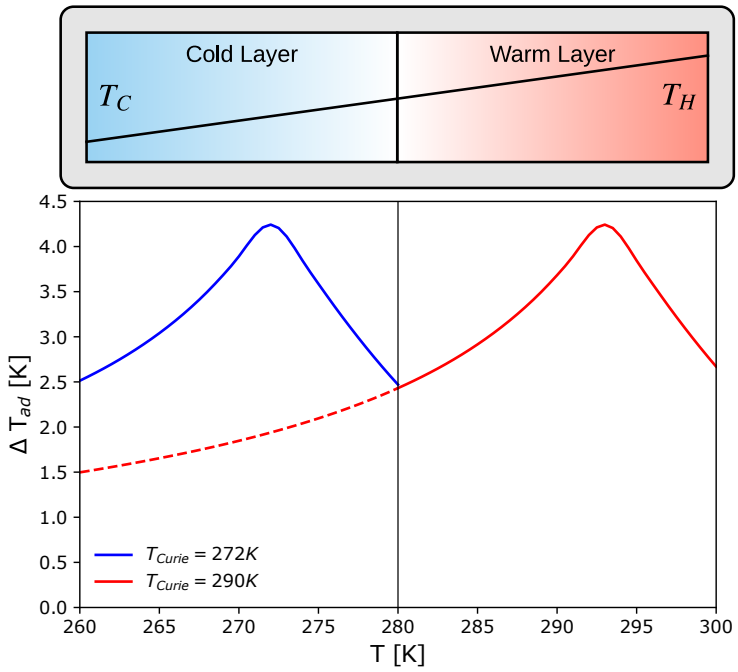

Figure 1.5: Illustration of how the two-layer regenerator increases the average adiabatic temperature change over a single-layer regenerator. Adiabatic temperature change of gadolinium with 0-1 T internal field variation shown.

1.2.2 Magnetic field source

The AMR cycle requires application and removal of a magnetic field source. This magnetic field can be created with permanent magnets or electromagnets, where the latter typically use windings of superconducting materials. Traditionally, room-temperature magnetic refrigeration devices with an emphasis on acceptable capital cost use permanent magnets while large-scale liquefiers for hydrogen or natural gas use superconducting magnets to attain higher efficiencies.

Permanent magnets

Permanent magnets are created by applying intense magnetic fields to crushed powders of elemental constituents [28] (e.g. Dy-NdFeB, SrFeO). Individual grains physically rotate until the magnetically preferred axis is aligned with the applied field, producing a magnetization that persists after the applied field has been removed. This is shown in Fig. 1.6 for a Dy-NdFeB permanent magnet, where in the absence of an external field (H), a flux density of B_{rem} remains. In high energy-product permanent magnet materials, this induced magnetization is stable. Intense fields can be applied (moving left on the X axis), however as long as the magnetization does not change direction (i.e. exceeding the polarization coercive strength, H_{cj}), the permanent magnet will return back to the original remanence strength.

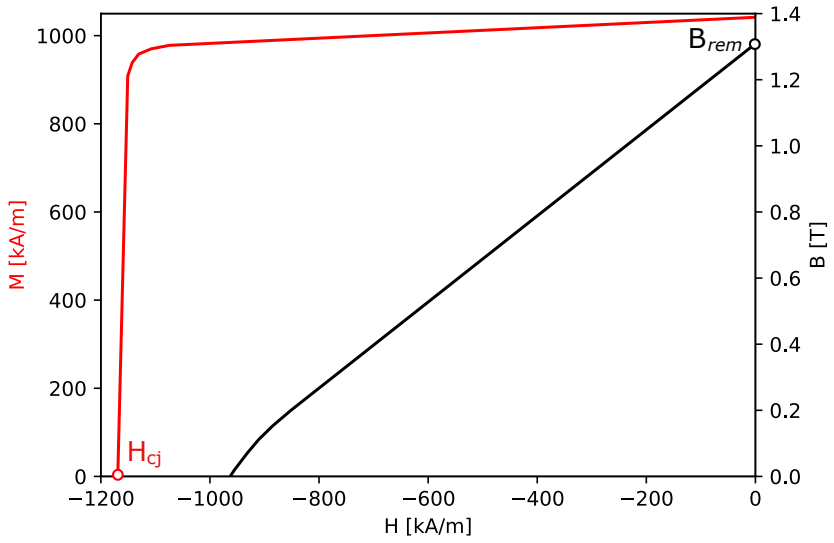

Figure 1.6: B-H (black, right axis) and M-H (red, left axis) curves for NdFeB permanent magnet material. Data from K&J Magnetics [2].

Permanent magnets are arranged into variable-strength magnetic circuits [29, 30, 31], and while the C-shape or horseshoe magnet structures remain popular, the benchmark magnetic circuit for magnetic refrigeration applications is the cylindrical Halbach array [28]:

$$(B_{rem,r}, B_{rem,\theta}) = B_{rem}(\cos(p\theta), \sin(p\theta)) \tag{1.8}$$

where $2p$ is the number of poles, r and θ are the polar coordinate axis and B_{rem} is the magnitude of the remanent flux density. Analytical field solutions are known [32], and the long dipolar Halbach cylinder ($p = 1$) produces a homogeneous field strength of:

$$B = B_{rem}\ln\left(\frac{R_o}{R_i}\right) \tag{1.9}$$

The remanence distribution and flux density of the dipolar Halbach array is shown in Fig. 1.7 below with $B_{rem} = 1.28$ T and $R_o/R_i = 4$ (Appendix C describes the numerical simulation of Halbach arrays using a finite difference scheme). While useful for design intuition and engineering calculations, real permanent magnet arrays must be constructed from finite segments with homogenous magnetization directions [33, 34]. Optimization methods have been proposed for permanent magnet structures [35, 36, 37, 38, 39, 40, 41], and the dissertations of Rasmus Bjørk and Andrea Insinga were dedicated to the development and optimization of permanent magnet field generators for magnetic cooling applications [42, 43].

Although the costs associated with the permanent magnet structure have been identified as the Achilles heel of magnetocaloric energy conversion devices [175, 70, 71], magnet design has been decoupled from AMR operation and commercially oriented magnetic field generators have not been optimized for cost. In addition, as permanent magnet topology optimization has not constrained coercivity, the optimal design of low-cost permanent magnet materials remains largely uninvestigated.

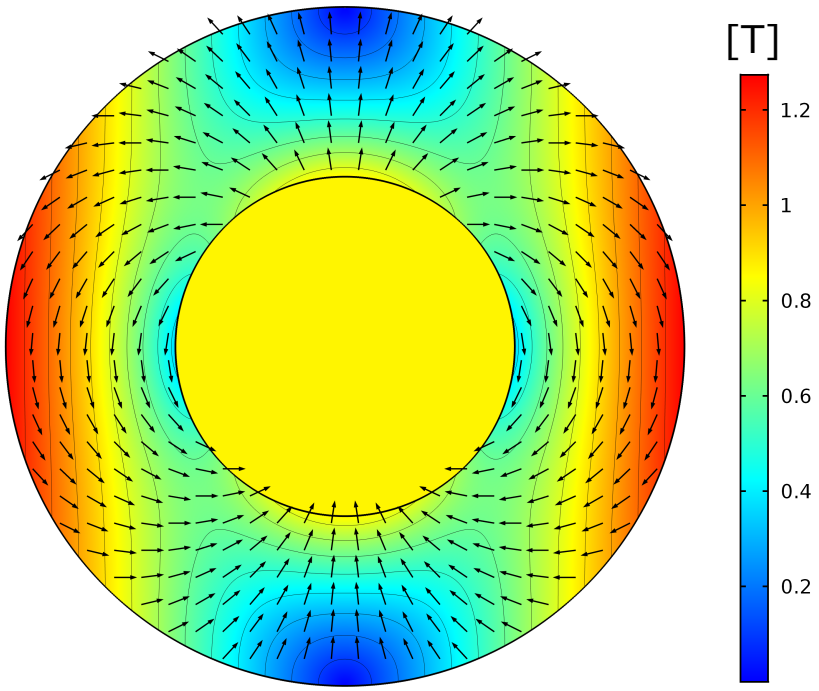

Figure 1.7: Flux density of Halbach cylinder with Ro/Ri = 2 and Brem=1.28T corresponding to a N42 grade permanent magnet. Black arrows show continuously varying distribution of remanence direction

Superconducting electromagnets

When a superconducting material is cooled below its critical temperature, the material exhibits near-perfect electron mobility. This allows greater current densities than traditional copper windings, which facilitates the generation of high magnetic fields with near-zero losses. The most commonly used superconducting material in active magnetic regenerative liquefiers is niobium titanium (NbTi) [44, 45, 46], as it is ductile, may be drawn into long wires and has a critical magnetic flux density exceeding 10 Tesla. NbTi is a low temperature superconductor (LTS) and is cooled below 4.2 K in a liquid helium bath or with a low-temperature Gifford-McMahon (GM) cryocooler. Fig. 1.8 below shows the NbTi superconducting solenoid and GM cryocooler used in Chapter 5.

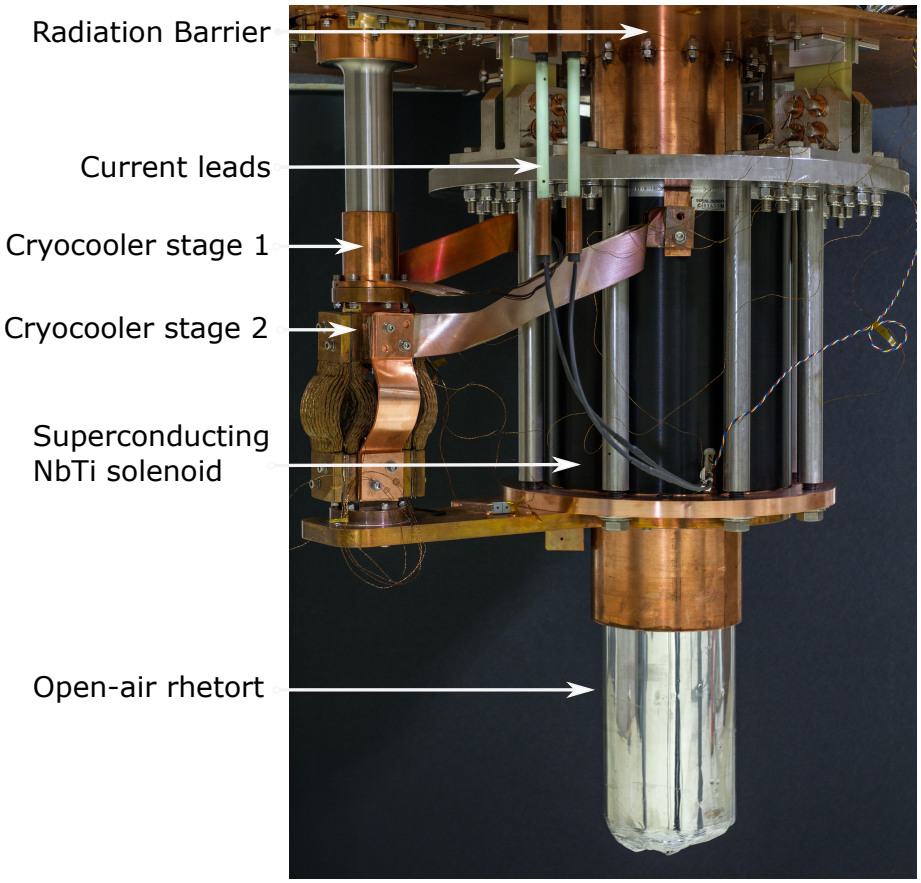

Figure 1.8: Pacific Northwest National Laboratory superconducting magnet assembly. NbTi solenoid conduction cooled below 3 K by cryocooler second stage. Regenerators enclosed in open-air rhetort. Photo courtesy of Evgueni Polikarpov.

As natural gas and hydrogen liquefiers require substantial cooling powers near

temperatures of 120 K and 20 K, respectively, many criticize the fact that a 4.2 K cryocooler is required to operate the superconducting magnet. High temperature superconductors (HTS) are emerging with promising performance, such rare-earth barium copper oxide tapes (REBCO) [47, 48], however engineering challenges are introduced that are accompanied with increased cost. Dr. Sangkwon Jeong's group has made a number of recent developments in high temperature superconducting magnets for active magnetic regenerative liquefiers [49, 50, 51].

As cryogenic AMR development is inherently expensive and time consuming, the field has not matured at the rate of room temperature magnetic refrigeration. The majority of cryogenic AMR devices use small amounts of magnetocaloric material, and a number of issues remain unsolved. AC losses in the windings and thermal structures have only recently been investigated [51], causing magnet heating that is exacerbated as systems scale towards commercial capacities [46].

1.2.3 Fluid flow control

To complete the AMR cycle, a fluid flow system is required to oscillate heat transfer fluid in the porous regenerator. The piston-based flow control system has demonstrated large temperature spans [52, 53], primarily due to the inherent flow balancing. The piston based system, however, is difficult to implement in an AMR device with more than two regenerators. An alternative flow control system uses a pump with valving to control the fluid blows. The most common configuration is the rotary valve with interchangeable valve plates [54, 55, 56, 57, 58, 59]. More recently, a series of cam-actuated poppet valves [60, 61] and solenoid valves [62] have been used. Several of these devices have demonstrated successful performance, however others have lower performance than prototypes with similar magnetic field strengths and refrigerant masses. This is likely caused by flow unbalance [63, 59, 61], inlet flow maldistribution [64, 65] and friction in the rotary valves [66]. Commercially oriented AMR devices require a fluid flow system with high performance, scalability and minimal lifetime maintenance.

1.3 Performance metrics

The performance of an AMR is commonly reported in literature with the temperature span vs. cooling capacity (T_{span} vs. $\dot{Q}_C$) curve, shown in Fig. 1.9. The AMR develops the maximum temperature span ($T_{span} = T_H - T_C$) with zero net cooling capacity. As load is applied, the temperature span decreases until the maximum cooling power is obtained with no temperature span.

The relationship between the temperature span and cooling power is to a good approximation linear when spatial variations in the magnetocaloric effect are minimal. Due to this linearity, devices are often characterized in terms of the no-load temperature span and zero-span cooling power [67]. Neither point, however, is commercially relevant and in reality an AMR will operate with a specified load and span. The exergetic cooling power ($\dot{E}x_Q$) describes the operating point with maximum refrigeration value and encapsulates the cooling power, heat rejection temperature (T_H) and temperature span [68].

$$\dot{E}x_Q = \dot{Q}_C\left(\frac{T_H - T_C}{T_C}\right) \tag{1.10}$$

The impact of AMR device configurations on the performance curve are shown conceptually in Fig. 1.9. The impact of applied field strength (and implicitly the magnetocaloric effect) is shown in Fig. 1.9 (a), where both the temperature span and cooling power are increased. The applied field strength, however, increases with permanent magnet mass which strongly increases capital cost. The magnetocaloric effect is primarily increased through material science development (e.g. magnetocaloric material discovery), however the average magnetocaloric effect for specific operating points can be increased with multilayering.

Fig. 1.9 (b) illustrates how increasing the magnetocaloric material (MCM) mass impacts the performance curve. While the cooling power is increased, the temperature span is relatively unaffected. Increasing the refrigerant mass increases the required high field volume, however, which increases capital costs from both the permanent magnet material and magnetocaloric refrigerant.

As an AMR device is inevitably imperfect, thermal interactions with the environment decrease the net cooling power from the AMR cooling power. These parasitic heat leaks can be modeled as a conductance between the hot and cold reservoirs ($\dot{Q}_{parasitic} = \kappa_{HC}(T_H - T_C)$), reducing performance with increasing T_{span}. Fig. 1.9 (c) illustrates the impact of parasitic heat leaks (and implicitly the regenerator effective-

ness) on the AMR performance curve.

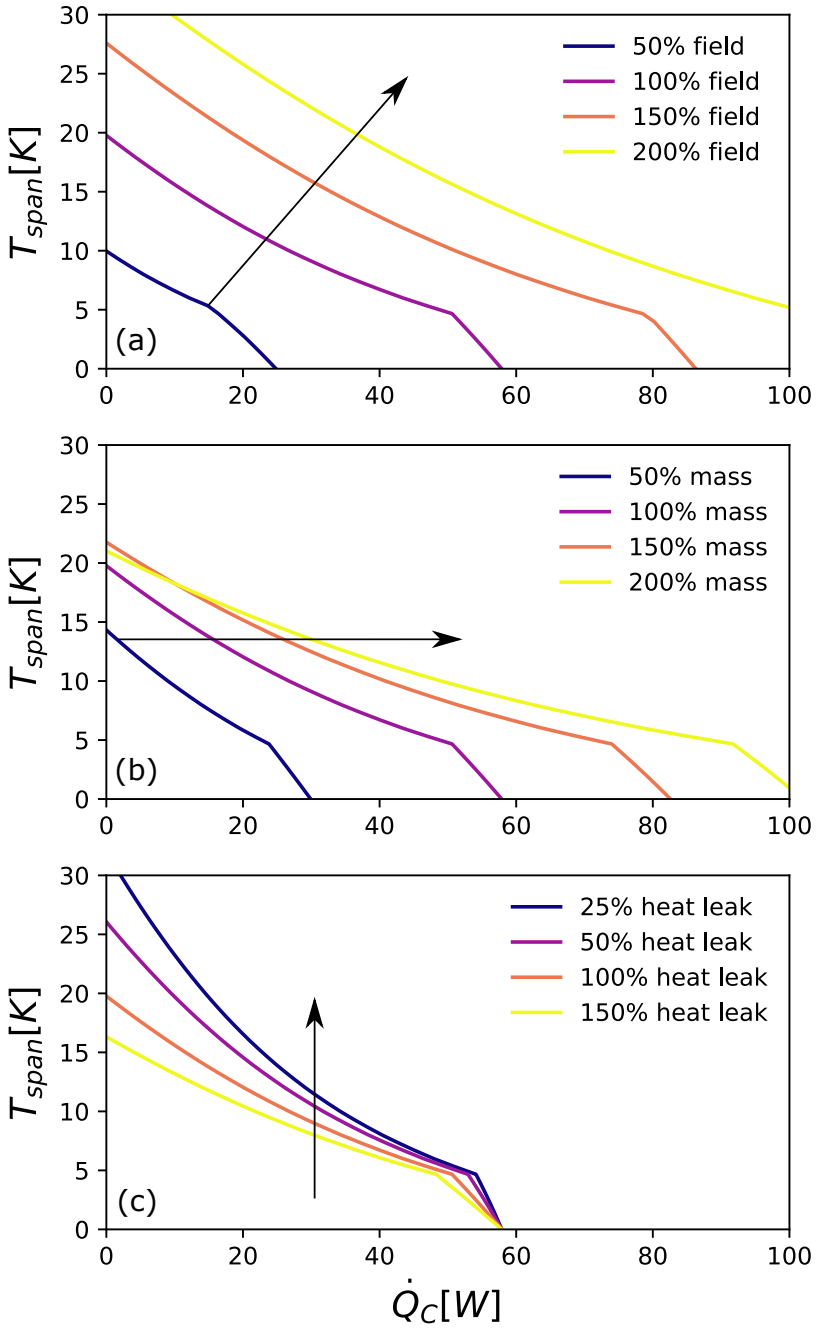

Figure 1.9: Simulating the impact of: (a) applied field strength (permanent magnet mass or magnetocaloric effect), (b) refrigerant mass (with constant utilization) and (c) reduced parasitic heat leaks (increased regenerator effectiveness)

Increasing the cooling capacity as in (b) is trivially obtained by building larger

machines. One of the challenges facing AMR device developers, however, is increasing the temperature span with acceptable cost. Building AMR devices with high temperature spans requires high performance magnetocaloric materials, effective regeneration and sound thermal design requiring insight from experimental development and modeling tools.

To be competitive with existing technologies, the efficiency must be considered with the performance $(T_{span}, \dot{Q}_C, \dot{E}x_Q)$. The coefficient of performance (COP) is a first-law metric and is the refrigeration equivalent of the thermal efficiency:

$$COP = \frac{\dot{Q}_C}{\dot{W}_{net}} \tag{1.11}$$

COP measurements are commonly reported for vapor-compression refrigeration devices and, as such, some literature reports COP numbers for direct comparison with existing technologies. In the context of a design objective, however, the COP increases without bound with decreasing temperature span; the maximum COP is realized at the zero-span $\dot{Q}_C$ which is not commercially relevant. A more meaningful metric is the second law efficiency, defined as the ratio of the ideal work requirement $(\dot{E}x_Q)$ to the actual work requirement $(\dot{W}_{net})$ [68].

$$\eta_{II} = \frac{\dot{Q}_C}{\dot{W}_{net}}\left(\frac{T_H - T_C}{T_C}\right) \tag{1.12}$$

Again considering a design objective, η_{II} is maximized with large magnetic fields (e.g. permanent magnet mass) and refrigerant masses. While the high efficiency reduces operating costs, the associated capital costs may be prohibitively large.

The conflicting objectives of temperature span, cooling power and second law efficiency can be addressed by considering a system-level thermoeconomic framework. Thermoeconomics allots costs to streams with thermodynamic value or exergy. The value streams yield a cost-rate balance where, for a refrigerator, capital and operating costs are used to provide a cooling service:

$$\dot{C}_{\mathrm{Q}} = \dot{Z} + \dot{C}_{\mathrm{op}} \tag{1.13}$$

in \$/h where streams with exergetic value are denoted by $\dot{C}$. The ammortized capital costs, $\dot{Z}$, typically consist of magnetocaloric material and either permanent magnet material (room-temperature applications) or superconducting material (for cryogenic applications), however the framework is highly flexible. Each cost rate is then decom-

posed into the product of exergy flow and the cost per unit exergy, e.g. $\dot{C}_{\mathrm{Q}} = \not{c}_{\mathrm{Q}} \dot{E}x_{\mathrm{Q}}$ ($\not{c}$ is used to distinguish costs from specific heat, c). Following the thermoeconomic approach used by Rowe (2011) [69, 67], the cost per exergetic cooling, $\not{c}_{\mathrm{Q}}$ in \$/kWh, of a magnetic refrigerator consisting of permanent magnet and magnetocaloric material can be expressed as:

$$\not{c}_{\mathrm{Q}} = \frac{CRF}{\dot{E}x_{\mathrm{Q}}}\left(\mathrm{Z}_{\mathrm{PMM}} + \mathrm{Z}_{\mathrm{MCM}}\right) + \not{c}_{\mathrm{e}}\left(\frac{1}{\eta_{II}}\right) \tag{1.14}$$

where $\mathrm{Z}_{\mathrm{PMM}}$ and $\mathrm{Z}_{\mathrm{MCM}}$ are the absolute capital costs of permanent magnet material and magnetocaloric material in \$, CRF is the capital recovery factor and $\not{c}_{\mathrm{e}}$ is the cost of electricity in \$/kWh. This balances the competing objectives of temperature span, cooling power, second law efficiency and capital cost into a single metric. Considering that magnetic refrigeration has matured beyond proof-of-concept devices, it is surprising that only a handful of works consider the combined capital and operating costs of an AMR [67, 70, 71].

1.4 Objectives

The objective of this dissertation is to improve the performance and lifetime cost of AMR devices. A combined experimental and numerical approach is employed to explore improvements at the component and the device scales, with a focus on the interaction between subsystems. To enable the development of this research, the following questions are investigated:

- How do fluid waveforms impact AMR performance, and why do similar AMR devices with different fluid flow systems vary in performance?
- What is the impact of regenerator composition on system performance? How do individual layers operate and interact, and can simplified modeling tools predict these complex behaviors?
- How do permanent magnet properties influence magnet design? What is the magnetic field waveform that minimizes AMR cost, and what is the optimal way to produce this field waveform?

1.5 Overview

The dissertation is outlined as follows, with a brief description of the main contributions. Each chapter is a peer-reviewed journal article that describes a performance improvement or cost reduction in AMR devices.

- Chapter 2 presents a cam-actuated valvetrain for controlling the waveform of regenerative fluid blows. This flow control device has numerous advantages over the friction-sealed rotary valve commonly found in literature, and the maximum exergetic cooling power is improved by tuning the fluid waveforms. (*International Journal of Refrigeration*, http://doi.org/10.1016/j.ijrefrig.2016.10.001)

- Chapter 3 describes a performance investigation of a two-layer AMR with second order magnetocaloric materials. An instrumented assembly identifies the performance of each layer as a function of the regenerator composition (i.e. Curie temperature spacing) for a number of operating parameters. (*Applied Thermal Engineering*, http://doi.org/10.1016/j.applthermaleng.2016.06.029)

- Chapter 4 proposes a new, highly efficient AMR modeling framework which is validated using the experiments in Chapter 3. Insights from the model are used to make device modifications and a no-load temperature span of 40 K is measured in close proximity to a simulated optimum; one of the highest in literature. (*Applied Thermal Engineering*, http://doi.org/10.1016/j.applthermaleng.2017.09.082)

- Chapter 5 identifies a passive structure to balance the force waveform of a multilayer AMR device with a conduction cooled superconducting solenoid for cryogen liquefaction. Using a genetic algorithm, nearly ideal balancing characteristics are obtained which increases both the efficiency and maximum attainable magnetic field. (*Journal of Magnetism and Magnetic Materials*, http://doi.org/10.1016/j.jmmm.2017.11.002)

- Chapter 6 presents a permanent magnet topology optimization to maximize the flux density of a Halbach cylinder subject to finite coercivity (i.e. avoiding permanent magnet failure). The numerical tool is used to assess the efficacy of reduced-rare-earth and rare-earth-free permanent magnet materials in literature. A number of formulations are investigated that explore the tradeoff be-

tween permanent magnet design sophistication and manufacturability. (*Journal of Applied Physics*, https://doi.org/10.1063/1.5026862)

- Chapter 7 presents a permanent magnet topology optimization to minimize the combined capital and operating costs of an AMR. The methodology simultaneously produces the optimal magnetic field waveform and the optimal means of producing this waveform in a framework for recycling rare-earth permanent magnet material. (*Journal of Magnetism and Magnetic Materials*, http://doi.org/10.1016/j.jmmm.2017.06.039)

Appendix A lists all publications, Appendix B presents the material properties used in this dissertation and Appendix C describes the numerical simulation of Halbach arrays using a finite difference scheme.

The work in this dissertation was performed by Reed Teyber; however, it should be noted that the 1-D numerical AMR model used in Chapter 3 was developed by Dr. Paulo Trevizoli [27]. This model was employed to analyze the two-material experiments, however the model is not a contribution in this dissertation.

Chapter 2

Experimental performance investigation of an Active Magnetic Regenerator subject to different fluid flow waveforms

International Journal of Refrigeration 74 (2017), 38-46.

Abstract

A flow control mechanism based on cam actuated valves is designed and implemented on an active magnetic regenerator test apparatus. The objective is to overcome the brief low field period of the nested concentric Halbach array by decreasing the fluid blow width; displacing fluid only when the magnetic field is close to the minimum and maximum values. Flow waveforms are simulated to evaluate varying blow durations with the same displaced volume. AMR experiments are performed where the largest exergetic cooling power of 1.62 W is obtained with $V_{\mathrm{D}} = 13.90$ cm^3 and a diversion ratio of $\delta = 0.41$, demonstrating an 11.2% increase over the sinusoidal waveform.

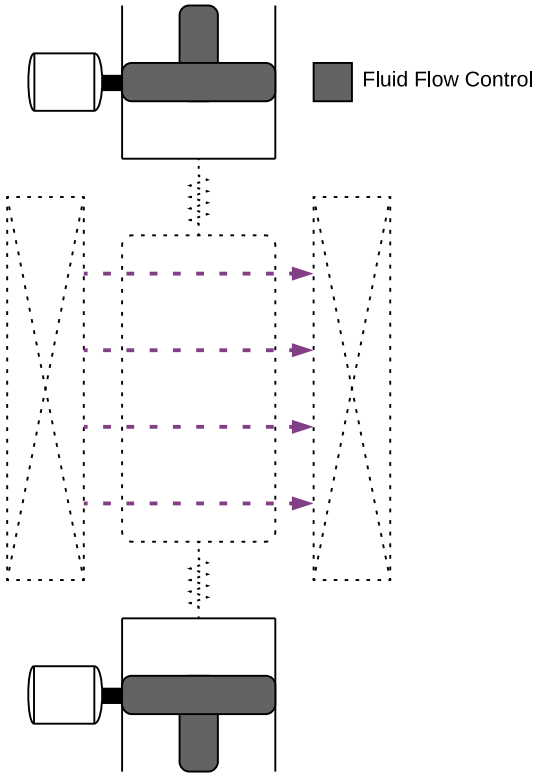

Figure 2.1: Graphical abstract of chapter 2, focusing on AMR fluid flow waveforms.

Nomenclature

Roman

A	area [m^2]
D_p	regenerator sphere diameter [m]
Ex_Q	exergetic cooling power [W]
f	frequency [Hz]
K	minor head loss [-]
L	length [m]
$\dot{m}$	mass flow rate [kgs^{-1}]
NTU	number of transfer units [-]
P	pressure [Pa; bar]
$\dot{Q}_c$	cooling capacity [W]
r	radius [m]
T	temperature [K]
t	time [s]
t^*	non-dimensional time [-]
U	velocity [ms^{-1}]
$\dot{V}$	volumetric flow rate [m^3s^{-1}]
V_D	displaced volume [cm^3]

Greek

ε	porosity [-]
δ	diversion ratio [-]
μ	viscosity [kg m^{-1} s^{-1}]
$\eta*$	weighted cooling capacity [-]
ω	angular velocity [rad s^{-1}]
ρ	density [kg m^{-3}]
τ	cycle period [s]
χ	valve stem displacement [m]

Subscripts and Superscripts

bed	subscript of regenerator bed
C	subscript of cold reservoir or cold side
D	subscript of Diversion flow
f	subscript of fluid
H	subscript of hot reservoir or hot side
HT	subscript of heat transfer
m	subscript of magnetic work
P	subscript of pump work
R	subscript of Regenerator flow
span	subscript of temperature span

2.1 Introduction

A large number of active magnetic regenerator (AMR) configurations can be created from the available combinations of magnetic field generators, fluid flow systems, regenerator geometries and magnetocaloric materials [13, 17]. The AMR prototypes developed at the University of Victoria [72, 52] use nested concentric Halbach cylinders as a magnetic circuit and a piston to sinusoidally drive fluid in the regenerator matrix. Although nested concentric Halbach arrays consisting of NdFeB magnet segments can generate magnetic flux densities exceeding 1.7 Tesla [73, 74, 75], when operating at constant angular velocity the magnetic field waveform has a brief low field period which reduces AMR performance.

Trevizoli *et al.* (2014) [76] showed numerically that changing the nested Halbach waveform to a sinusoidal or step change field waveform can increase the maximum cooling capacity by over 20% and 50%, respectively. Bjørk and Engelbrecht (2011) [77] found that increasing the ramp period of the magnetic field waveform by 10% decreased the temperature span and cooling capacity up to 20%. Plaznik *et al.* (2013) [78] investigated different thermodynamic cycles with an AMR by altering the magnetic field and fluid flow waveforms, measuring a 10% increase in temperature span by displacing fluid both in the high field and the ramp period. The displaced volume, however, was not fixed in the experiments and the magnetic ramp period was small relative to the high field period; dissimilar to the nested Halbach waveform.

In the present work, the performance of an AMR with nested Halbach cylinders subjected to different fluid flow waveforms is experimentally investigated. The idea is to change the fluid flow waveform to displace fluid when the magnetic field is near the maximum and minimum values. This increases the average magnetic field change during the blow period at the expense of increased thermal losses due to the no flow period. With this objective, a new flow control system is implemented on the PM II test device [52], in which cam-actuated valves selectively divert fluid from the regenerators to a secondary loop. The diverted flow profiles are simulated with a simple pressure drop model to obtain waveforms with varying blow widths (the cycle duration in which fluid is displaced) but equal displaced volumes (or utilization factor). The performance is then evaluated based on T_{span} $\dot{Q}_{\text{C}}$ and Ex_{Q} which are experimentally characterized at a fixed frequency of 0.8 Hz and rejection temperature of 298 K for several displaced fluid volumes.

2.2 Methodology

2.2.1 AMR test apparatus

The Permanent Magnet Magnetic Refrigerator (PM II) device is an AMR test apparatus developed at the University of Victoria [52]. The device contains two cylindrical regenerators housed in the bore of two nested concentric Halbach arrays which are de-phased by 180°. The mechanical drive system synchronously rotates the Halbach arrays and a double effect piston which sinusoidally drives fluid in the regenerator beds. In operation, warm fluid is pumped to the hot end where heat is released, and cold fluid is pumped to the cold end where heat is absorbed [16]. Outside the regenerator, a system of check valves creates unidirectional flow through the hot and cold heat exchangers. The hot heat exchanger is controlled by thermal bath, while a heater, controlled by an external power supply, provides a thermal load at the cold heat exchanger.

Each regenerator housing, made of Ultem polyetherimide, has dimensions of 22.4 mm ID, 24.2 mm OD and a total length of 65 mm yielding a mass of 130 g per regenerator (260 g total). The magnetocaloric matrix consists of packed Gadolinium spheres with an average particle diameter of 500 μm and a porosity of 0.36. The heat transfer fluid is a mixture of water and ethylene glycol (90/10 %vol).

2.2.2 Cam-actuated valving system

The piston-based flow control system has demonstrated large temperature spans, primarily due to the inherent flow balancing. The existing piston based system, however, has a fixed blow width which is difficult to investigate Halbach field ramping or implement in an AMR device with more than two regenerators. An alternative flow control system uses a pump with valving to control the fluid blow width. The most common is a rotary valve with interchangeable valve plates [54, 55, 56, 57, 58], and more recently a series of cam-actuated poppet valves has also been used [60]. Several of these devices have demonstrated successful performance, however some have demonstrated reduced performance compared to prototypes with similar magnetic field strengths and refrigerant mass, possibly due to flow unbalance [63], inlet flow maldistributions [64] and friction in the rotary valves [66].

In an effort to change the fluid flow profiles with the existing piston-based flow system in PM II, a secondary loop is implemented which diverts flow from the re-

generators to control the blow width as shown in Fig. 2.2. A total of four one-way, normally closed valves are used (Clippard MJV-2 Valve and MBA-1 Actuator); two of which modulate flow to the regenerator (R1-R2) while the other two modulate each direction of the diversion blow (D1-D2) [79].

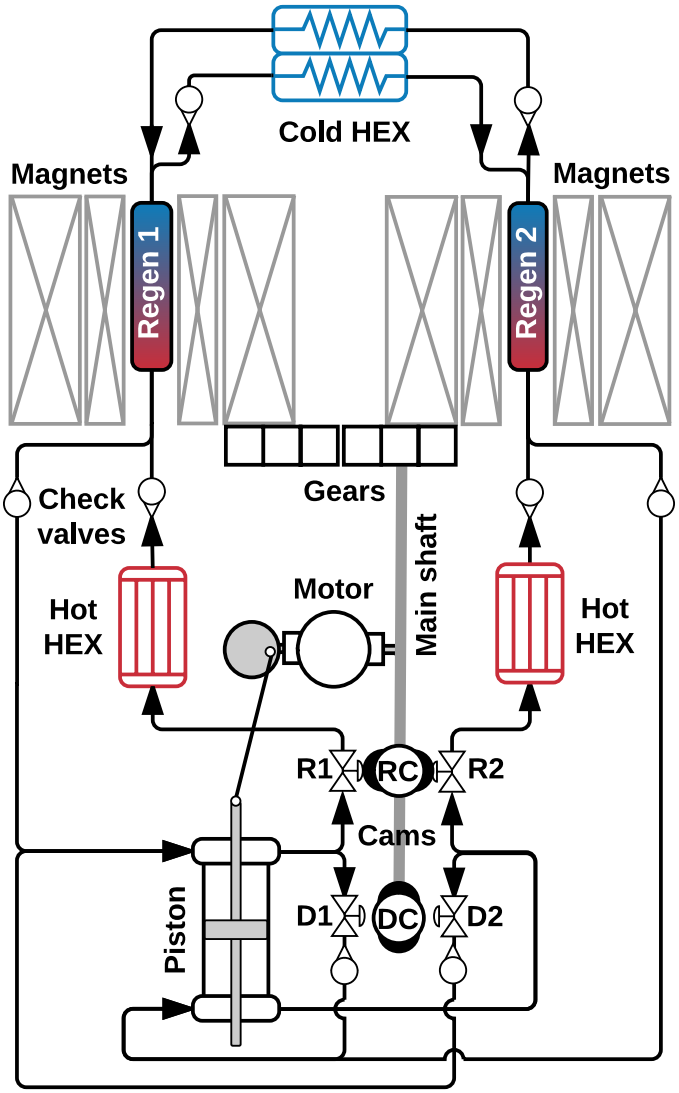

Figure 2.2: Modified PM II test apparatus schematic with the secondary fluid loop and cam actuated valves.

Flow is diverted from the regenerators when the diversion valve stems (D1-D2) are depressed by the diversion cams (DC), creating a static period of no fluid flow in the regenerators. The fluid blow begins when the regenerator valve stems (R1-R2) are depressed by the regenerator cams (RC) and the diversion valves close; shown

in Fig. 2.3 for a single blow (t^*=0-0.5). $t^* = t/\tau$ is the non-dimensional cycle time, defined as the ratio between the actual time t and the cycle period τ, ranging from 0 to 1. The valves are actuated by individual cams with a harmonic ramp profile.

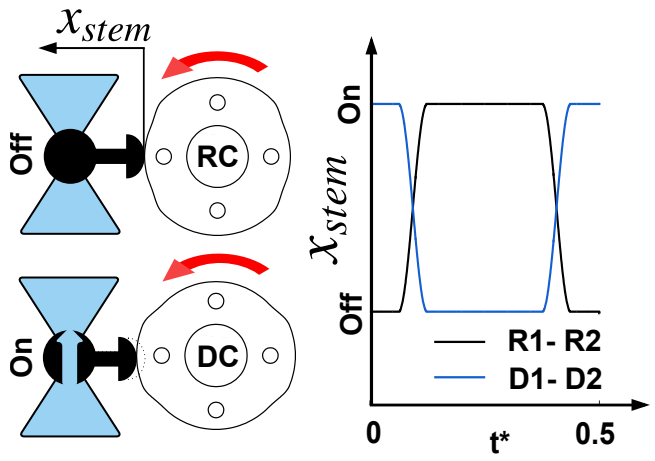

Figure 2.3: Schematic of valve operation and valve stem displacement.

A total of six fluid waveforms with varying blow widths are experimentally characterized, each requiring a new set of four regenerator (RC) and diversion (DC) cams. To facilitate changing fluid flow waveforms, the camshaft is designed with a focus on cam manufacturing and replacement. In the present work, cams are machined from 6.35 mm thick low friction Acetal plate as shown in the bottom right of Fig. 3 and mount on a central shaft for concentricity. Four threaded rods penetrate the cams into the camshaft flanges to transmit torque and axially clamp the assembly. To change the fluid blow width, the existing cams are removed from the shaft, shown in the top right of Fig. 2.4, and a new set of cams is installed. To change the peak fluid velocity, the piston stroke is adjusted in fixed increments of 5 mm.

The camshaft is directly driven by the piston-crank gear, which meshes with the geartrain driving the magnets. The direct coupling insures repeatable alignment of the cams with the fluid flow and magnetic field waveforms, however torque fluctuations in the magnet affect all driven components.

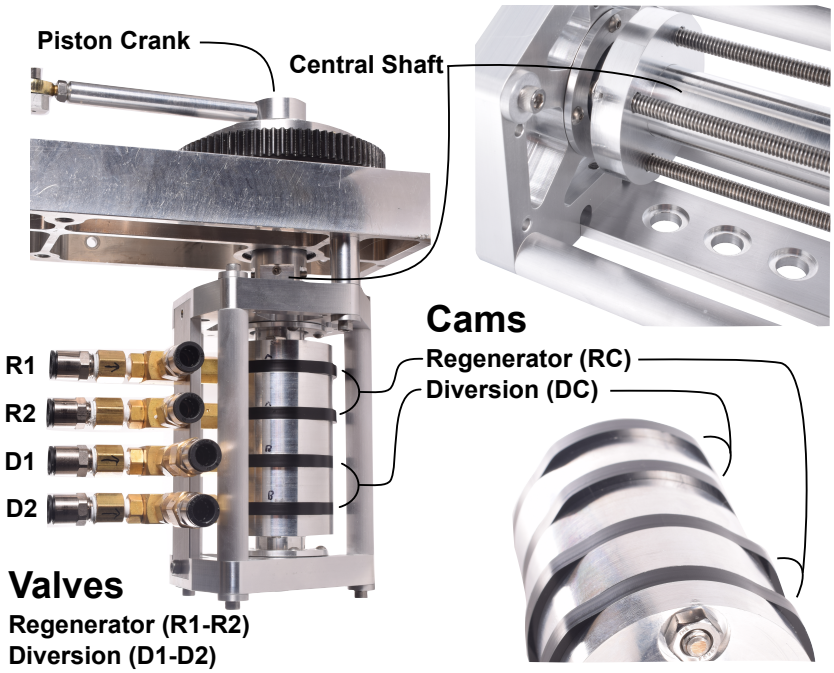

Figure 2.4: Camshaft prototype.

2.2.3 Simulation of fluid flow waveforms

As shown in Fig. 2.3, a valve transition period exists between discrete states where fluid flows entirely through the secondary loop or through the regenerator loop. The transition period occurs over an angular window of 22.5 degrees, where the valve stems are displaced from one position to another. The flow is simulated with a simple pressure drop model and results are used to design cam profiles which yield fluid waveforms of constant displaced volume.

The modified PM II schematic in Fig. 2.2 is modeled as two fluid loops in parallel: the diversion (secondary) loop (D) containing a single control valve, and the regenerator loop (R) treated as a control valve in series with a packed bed of spherical particles. Fluid flow through the porous media is modeled with the one-dimensional Ergun equation [80] and each valve is treated as a minor head loss which varies with the valve stem position [81]:

$$K_{\text{valve}} = \frac{\Delta P}{\frac{1}{2}\rho U^2} \tag{2.1}$$

where ΔP, ρ and U are the pressure drop, fluid density and fluid velocity, respectively. The minor head loss is experimentally characterized by measuring the pressure drop and the fluid velocity through the valve for ten stem depressions ranging from fully closed to fully open. The pressure drop across the valve is low relative to the packed bed until the valve abruptly closes. Assuming an incompressible fluid and temperature independent properties, the pressure drop for the regenerator and diversion loops are, respectively:

$$\Delta P_{\text{R}} = K_{\text{valve}}(x_{\text{R}})\frac{\rho}{2A_{\text{valve}}^2}\dot{V}_{\text{R}}^2 + L_{\text{bed}}\left[\frac{150\mu(1-\varepsilon)^2}{D_p^2\varepsilon^3 A_{\text{bed}}}\dot{V}_{\text{R}} + \frac{1.75\rho(1-\varepsilon)}{D_p\varepsilon^3 A_{\text{bed}}^2}\dot{V}_{\text{R}}^2\right] \tag{2.2}$$

$$\Delta P_{\text{D}} = K_{\text{valve}}(x_{\text{D}})\frac{\rho}{2A_{\text{valve}}^2}\dot{V}_{\text{D}}^2 \tag{2.3}$$

where $\dot{V}$ is the volumetric flow rate, μ, ε, L_{bed} and D_p are the fluid viscosity, bed porosity, bed length and particle diameter, respectively. A stands for the flow area of the piston, bed or valve. x_R and x_D are the valve stem displacement waveforms, as in Fig. 2.3. Assuming constant angular velocity (ω) and applying mass conservation:

$$\dot{V}_{\mathrm{R}} + \dot{V}_{\mathrm{D}} = r_{\mathrm{crank}} \omega A_{\mathrm{piston}} sin(\omega t) \tag{2.4}$$

Although the flow changes with time, inertial effects are assumed negligible, allowing implementation of pipe network relations. This presents a middle ground in numerical sophistication between the resistive network approach presented by Eriksen *et al.*(2016) [63], which assumes linear scaling between pressure drop and flow rate, and solving the Brinkman-Forchheimer equation for momentum transfer in porous media [82]. In a pipe network, the pressure drop across across parallel branches is balanced ($\Delta P_{\mathrm{R}} = \Delta P_{\mathrm{D}}$). The system of equations is solved at each time step, yielding the simulated flow rate in the valve transition period. The solution is repeated in a binary search to identify the cam profiles which yield decreasing blow widths of equal displaced fluid volume. The resulting fluid waveforms are characterized by the displaced volume through the regenerator (V_{D}) and the diversion ratio (δ), which is the ratio between the diverted fluid volume ($V_{\mathrm{D},\delta}$) and the total displaced volume ($V_{\mathrm{D,total}}$):

$$\delta = \frac{V_{\mathrm{D},\delta}}{V_{\mathrm{D,total}}} \tag{2.5}$$

where larger values of δ correspond to larger diverted fluid volumes and shorter blow widths.

The simulated waveforms are shown on the left of Fig. 2.5(a) for a fixed displaced volume of V_{D}= 13.90 cm^3. The dashed line corresponds to the simulated PM II magnetic field waveform. The diversion ratio increases with the piston stroke to displace the same volume of fluid through the regenerators, i.e., at the same utilization factor. At the same time, increasing δ increases the flow weighted average magnetic field change (ΔH) during the regenerator flow period, which is defined in Eq. (2.6) [83]. The values of ΔH for the non-diverted and diverted waveforms are also presented in Fig. 2.5(a) for the simulated cases, where it is clear that ΔH increases as δ increases.

$$\Delta H = \frac{1}{V_{\mathrm{D}}} \left(\int_{0.5}^{1} |H\dot{V}| dt^* - \int_{0}^{0.5} |H\dot{V}| dt^* \right) \tag{2.6}$$

Still in Fig. 2.5(a), the secondary loop is preferential in the transition period until the diversion valves are nearly closed, causing an abrupt transition between the simulated blow and no-blow states. This indicates the valve transition period has a small impact on the displaced volume.

The experimental pressure waveforms are shown in Fig. 2.5(b), where some dif-

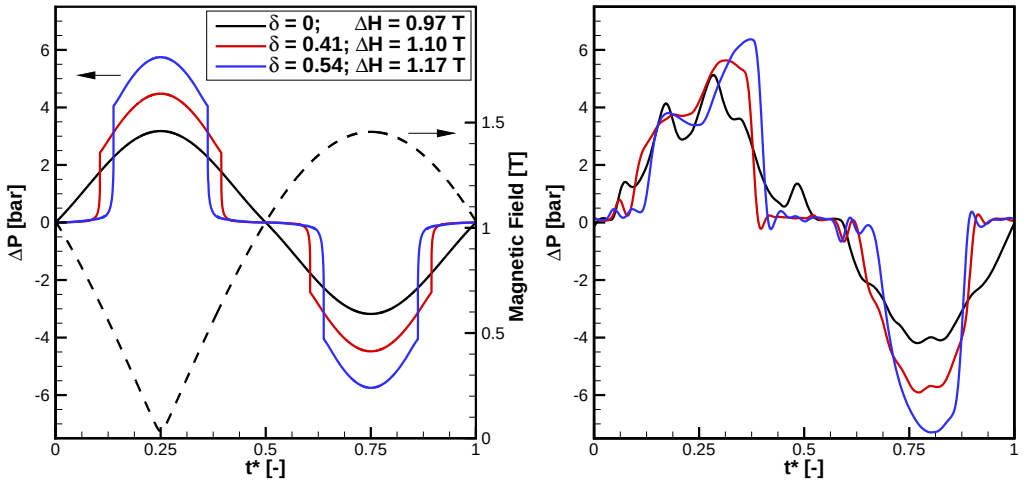

Figure 2.5: Fluid flow waveforms characterized by the pressure drop as a function of the dimensionless time: (a) Simulated; (b) Experimentally measured.

ferences between the simulated and measured pressure waveforms are observed. The measured waveforms show a more continuous variation in pressure than the simulations; likely caused by air entrapment or tubing deformation, which is difficult to model. Additionally, torque interactions between nested Halbach cylinders influence the gear train and piston crank, introducing a medium frequency torque oscillation from Halbach segment attraction and a stronger, low frequency torque from the tendency of cylinders to align [84, 27]. This stronger alignment causes the blow time in one direction (t*=0-0.5) to be greater than the blow time in the returning direction (t*=0.5-1).

2.2.4 Operating conditions

The experiments described here are performed with a fixed rejection temperature (T_{H}) of 298 K and operating frequency (f) of 0.8 Hz. Higher frequencies increase the rotational inertia, attenuating the torque fluctuations in the fluid waveform. The frequency and regenerator length are chosen to ensure a suitable number of waveforms are evaluated within the maximum design pressure of 10 Bar. The thermal load ($\dot{Q}_{\mathrm{C}}$) applied to the cold heat exchanger heater is varied from zero (no-load) up to 80 W, depending on the displaced fluid volume, in steps of 20 W. Table 2.1 summarizes the tested displaced volumes, cooling capacities and diversion ratios. The average ambient temperature in the present tests is 294 K.

Table 2.1: Summary of tested fluid waveforms and thermal loads.

Stroke (cm)	V_D (cm^3)	$\dot{Q}_C$	δ
0.5	3.48	0-20	0
1	6.95	0-40	0, 0.54, 0.74
1.5	10.42	0-60	0, 0.46, 0.59
2	13.9	0-80	0, 0.41, 0.54
2.5	17.44	0-80	0
3	20.85	0-80	0

The results are evaluated based on the thermal load, regenerator temperature span (T_{span}) and exergetic cooling power (Ex_Q). The presented temperature spans are the average of the two regenerator spans over 30 seconds after reaching periodic steady-state. This criterion is determined when the average span changes less than 0.04 K over 12 minutes, which is reached within 2 hours of operation for each data point. The exergetic cooling power is defined as:

$$Ex_Q = \dot{Q}_C \frac{T_{span}}{T_C} \tag{2.7}$$

The experimental procedure is repeated for several operating conditions with a reproducibility within 0.3 K. The experimental uncertainties, evaluated according to [85], for T_{span} and $\dot{Q}_C$ are estimated to be 0.8 K and 2.5%, respectively. The uncertainty of Ex_Q in the range of interest is between 0.12 and 0.17 W.

2.3 Results

T_{span} and Ex_Q as a function of $\dot{Q}_C$ are shown in Fig. 2.6(a) and (b), respectively, for a range of displaced volumes with non-diverted waveforms (δ=0). These curves are the benchmark to evaluate diverted fluid waveforms. A maximum no-load temperature span of 18.4 K is obtained with a displaced volume of V_D= 6.95 cm^3 and a span of 4.0 K is developed with a displaced volume of V_D= 17.44 cm^3 at the largest tested load of $\dot{Q}_C$= 80 W. Regarding the exergetic cooling power, Ex_Q increases with load up to a maximum value for each displaced volume. The maximum Ex_Q also changes with the displaced volume. The peak Ex_Q found is 1.45 W for $\dot{Q}_C$ = 60 W and V_D = 13.9 cm^3. The no-load temperature span, thermal load and exergetic cooling power are sensitive to changes in the displaced volume, therefore demonstrating the need to fix V_D (which means fixing the utilization factor) when investigating the diverted

fluid waveforms.

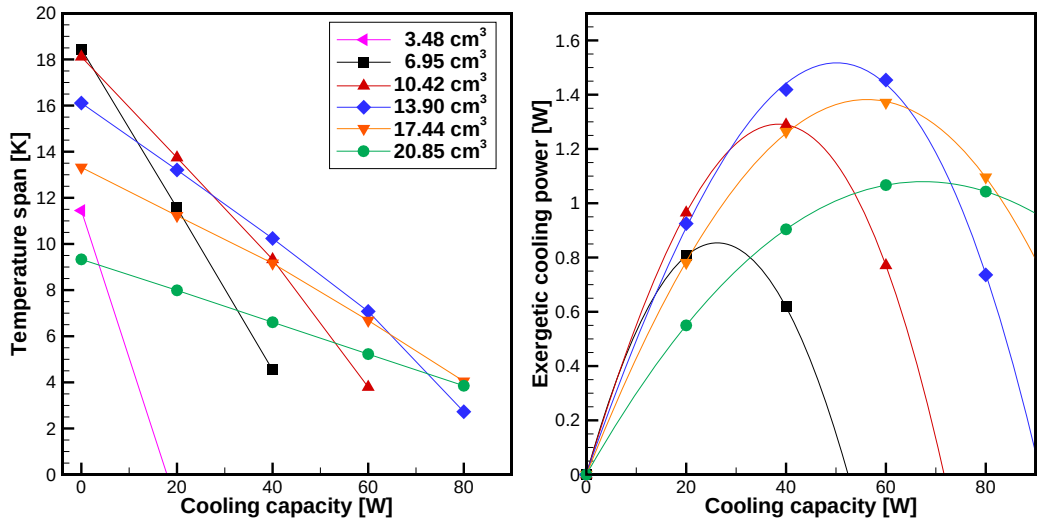

(a) (b)

Figure 2.6: AMR performance for non-diverted waveforms (δ=0) for different displaced volumes: (a) T_{span} as a function $\dot{Q}_{\text{C}}$; (b) Ex_{Q} as a function $\dot{Q}_{\text{C}}$.

T_{span} and Ex_{Q} as a function $\dot{Q}_{\text{C}}$ are shown for the diverted fluid waveforms in Fig. 2.7. Each window compares the performance of two diverted fluid volumes ($\delta > 0$) to the non-diverted waveform ($\delta = 0$), all at a fixed displaced volume. To better visualize the results, the x-axis range varies with the displaced volume. The smallest non-zero δ universally outperforms both $\delta = 0$ and the largest δ, and the performance improvements increase with load. The performance is reduced with the largest δ, in particular for the smaller displaced volume.

2.4 Discussion

The idea of using fluid waveforms with different no-blow periods is to increase the flow weighted average magnetic field change as in Fig. 2.5. Several performance limiting effects, however, are observed:

- (i) as δ increases, the superficial velocity (or average mass flow rate) increases to displace a fixed volume of fluid over a reduced blow duration. As a result, the NTU decreases with the increasing average flow rate. In addition, the axial dispersion and viscous dissipation increase with mass flow. These effects reduce the regenerator thermal effectiveness and, consequently, the AMR performance;

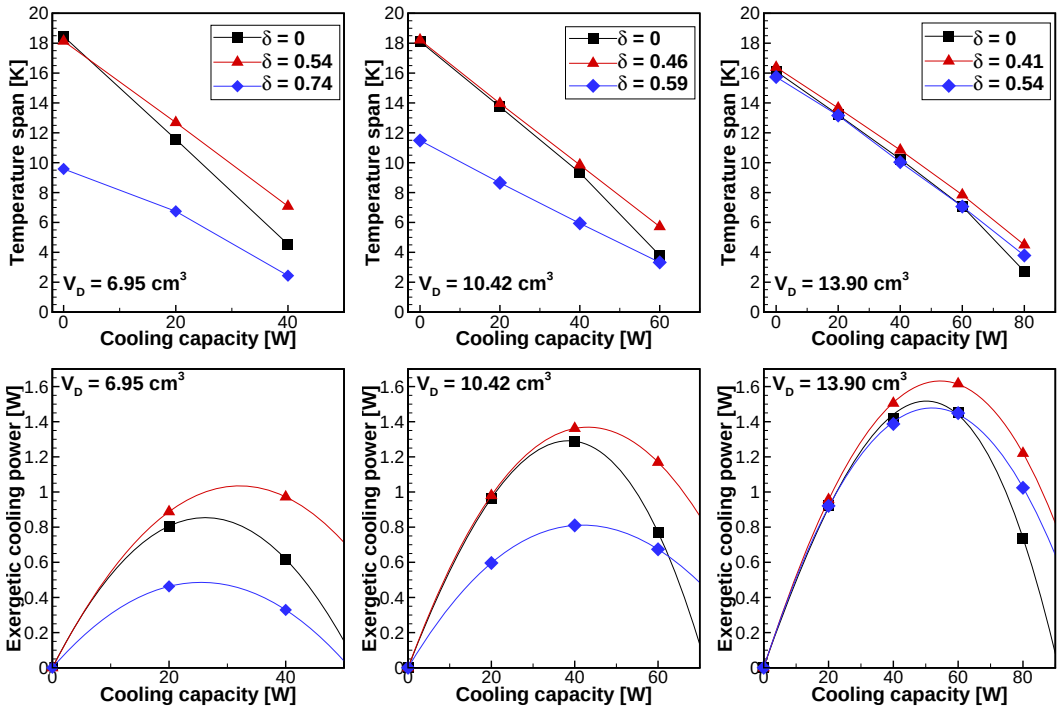

Figure 2.7: AMR performance for non-diverted and diverted waveforms ($\delta > 0$) for different displaced volumes. The top windows show the T_{span} as a function $\dot{Q}_{\text{C}}$ curves; and the bottom windows show the Ex_{Q} as a function $\dot{Q}_{\text{C}}$ curves.

- (ii) unbalanced flow effects.

Comparing the diverted and non-diverted waveforms in Fig. 2.7, the lower δ case outperforms the $\delta = 0$ curve, especially with high thermal loads for each displaced volume. With no applied load, no performance improvement is found even for the lower δ cases. This is mainly attributed to the increased effect of NTU losses (item (i)). NTU is defined as [86]:

$$NTU = \frac{hA_{\text{HT}}}{\dot{m}c_{\text{f}}} \tag{2.8}$$

where h is the convective heat transfer coefficient obtained from the Wakao and Kaguei (1982) [87] Nusselt correlation, A_{HT} is the interphase heat transfer area for a packed bed of spheres [82], $\dot{m}$ is the mass flow rate averaged over the fluid blow and c_{f} is the fluid heat capacity. As the volumetric flow rate (or $\dot{m}$) increases with the increasing δ, for a fixed V_{D}, the NTU exponentially decreases as presented in Fig. 2.8. This is more visible for V_{D} of 6.95 cm^3 where the NTU reduces from 19.3 at $\delta = 0$ to 9.6 at $\delta = 0.74$. A smaller NTU results in a smaller heat transfer effectiveness,

which is directly linked to the AMR temperature spans. Hence, the combined effects described in items (i) and (ii) are relevant for the largest δ curve, which is universally inferior to the benchmark $\delta = 0$ curve. It is observed from the presented results that an optimal diversion ratio exists which balances the gain in the flow-averaged magnetic field variation with the increased effect of NTU losses.

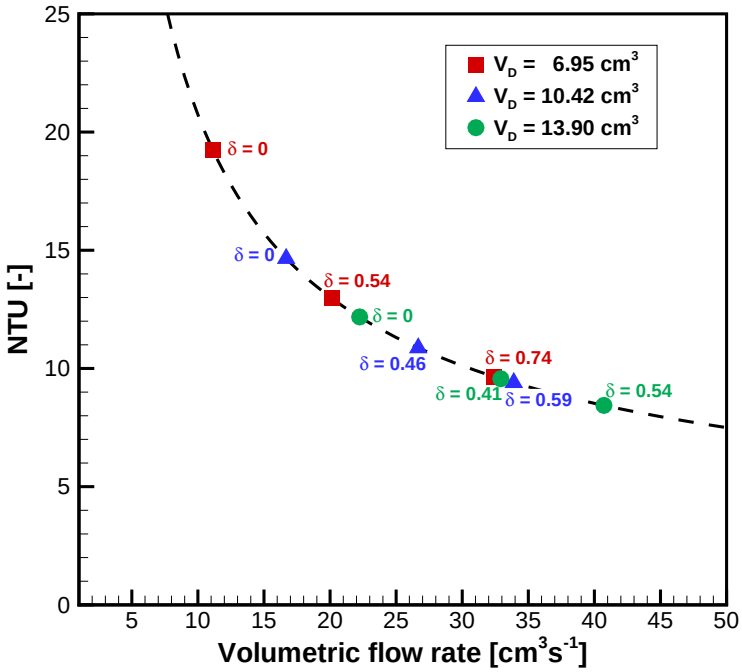

Figure 2.8: NTU as a function of the volumetric flow rate.

Regarding item (ii), the largest values of δ exhibit an unbalanced displaced fluid volume, which helps explain the reduced performance. Unbalanced flow is when the hot and cold streams through the regenerator have different displaced volumes, causing a net circulation of flow [63]. The unbalanced displaced volume occurs when a brief change in rotational velocity coincides with the valve transition period.

The impact of unbalanced flow is evaluated based on the regenerator temperature distribution; formed from each regenerators hot, middle and cold end temperature readings. More details on the internal thermocouple is available in Ref. [1]. Fig. 2.9 shows the cycle averaged temperature profile along the AMR bed for different values of δ with a fixed displaced volume of $V_{\mathrm{D}} = 13.90$ cm^3 and an applied load of $\dot{Q}_{\mathrm{C}} = 60$ W.

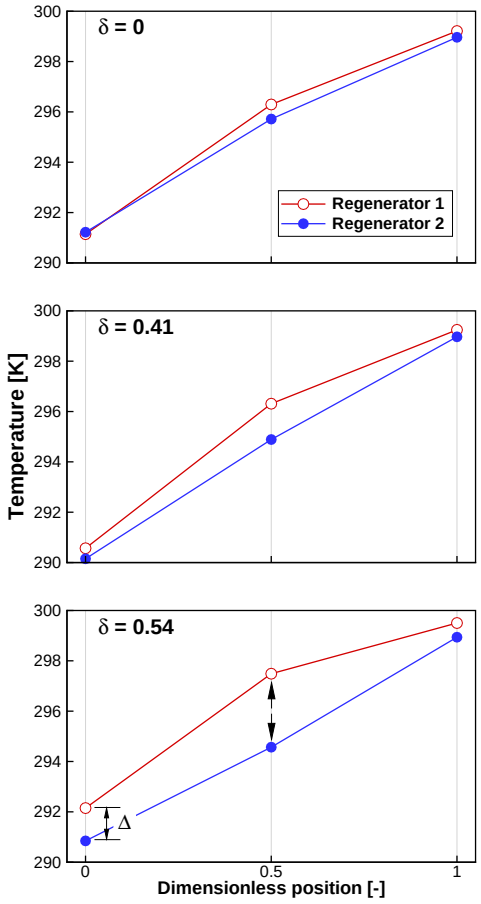

Figure 2.9: Regenerator temperature distribution with unbalanced displaced volume

Comparing the three cases in Fig. 2.9, as δ increases a displacement in temperatures between Regenerator 1 and 2 is observed. This displacement is greatest for $\delta = 0.54$, where Δ shows a deviation in the cold end temperature readings. This suggests a net influx of warm fluid from the hot reservoir into Regenerator 1. The internal temperature reading is even more sensitive to unbalanced flow conditions, which is in agreement with simulation results from Eriksen *et al.* (2016) [63].

Due to the loss mechanisms effecting the diverted fluid waveforms, the maximum temperature spans are not improved with a no-flow period. For all displaced volumes, however, the smallest δ waveform presents a significant improvement in exergetic cooling power over the non-diverted case. The largest Ex_{Q} of 1.62 W is obtained with $V_{\mathrm{D}} = 13.90$ cm^3 and $\delta = 0.41$, which represents an 11.2% increase over the non-diverted waveform. The improvement of Ex_{Q} is of the same order as the improvement from multilayering recently reported by the present authors [1].

Although the diverted waveforms increase the exergetic cooling power, the efficiency is penalized with the increased pressure drop. We propose the following figure of merit ($\eta*$), which relates the exergetic cooling capacity to the pump work ($\dot{W}_{\mathrm{p}}$).

$$\eta* = \frac{Ex_{\mathrm{Q}}}{\dot{W}_{\mathrm{p}}} \tag{2.9}$$

where $\dot{W}_{\mathrm{p}}$ is calculated as follows, assuming a sinusoidal $\dot{V}$ profile for each fluid waveform:

$$\dot{W}_{\mathrm{p}} = \frac{1}{\tau_{\mathrm{c}}} \int_0^{\tau_{\mathrm{c}}} \dot{V} \Delta P dt \tag{2.10}$$

Fig. 2.10 shows the behavior of Ex_{Q} and $\eta*$ as a function of δ. A fixed temperature span of 10 K is considered, in which the values of Ex_{Q} and $\dot{W}_{\mathrm{p}}$ are obtained by interpolation. Ex_{Q} is maximized with the smallest non-zero value of δ. In the case of 6.95 cm^3 , the largest δ presents a negative value of Ex_{Q} and is not shown. $\eta*$, on the other hand, always decreases with δ, showing that the increase in exergetic cooling capacity is small relative to the increase in pump work.

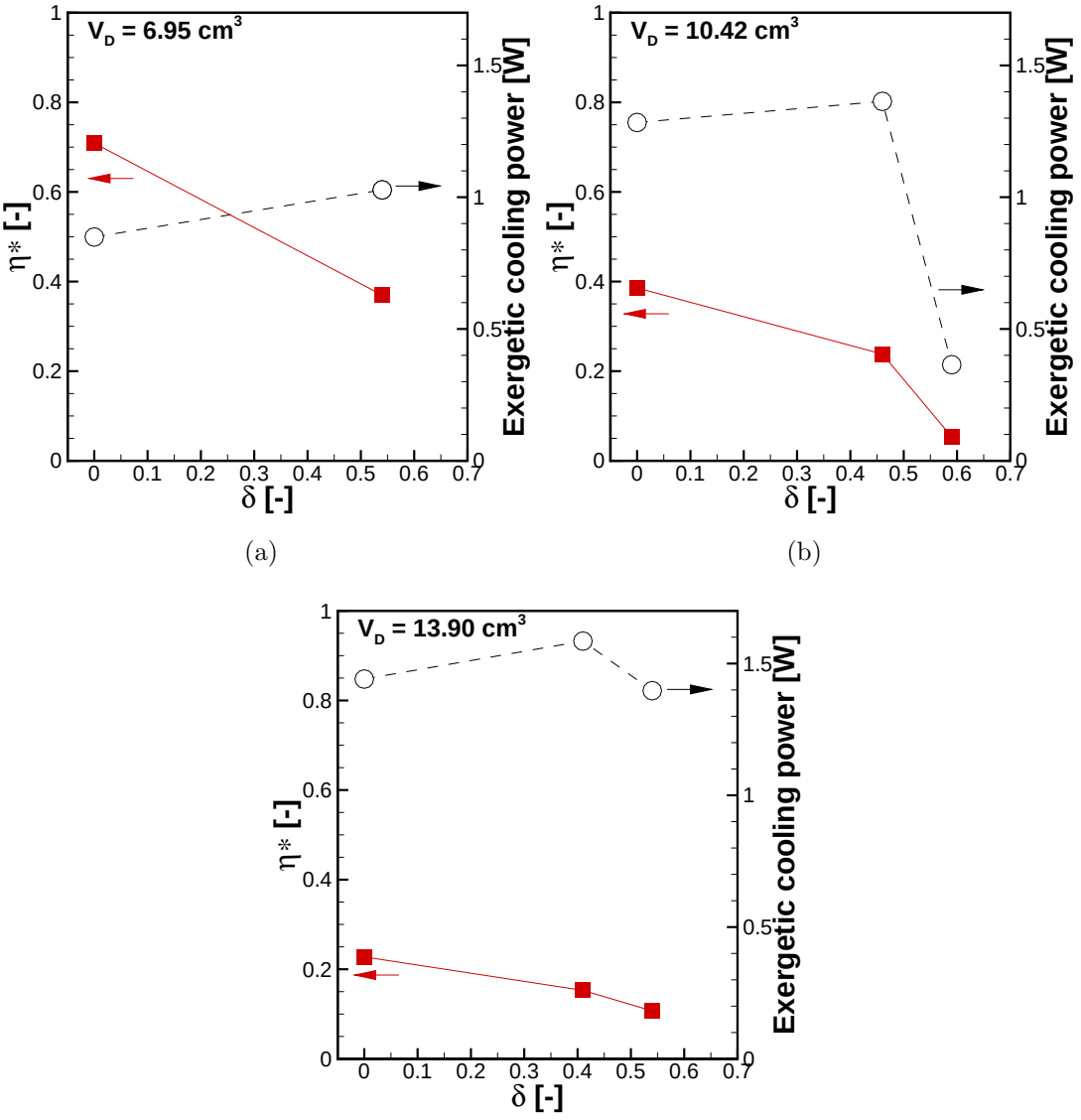

Figure 2.10: Exergetic cooling power (right y-axis) and $\eta*$ (left y-axis) as a function of δ for different displaced volumes at a fixed temperature span of 10 K: (a) 6.95 cm^3; (b) 10.42 cm^3; (c) 13.90 cm^3.

2.5 Conclusions

The PM II AMR test apparatus uses nested concentric Halbach cylinders which have a brief low field period. In the present work, the sinusoidal fluid velocity waveform is modified with a no-blow period to displace fluid when the change in magnetic field is highest. To accomplish this, a cam-actuated valvetrain is developed which diverts fluid from the regenerators to shape a user-defined fluid blow. The fluid waveforms are simulated to evaluate waveforms of varying blow widths with equal displaced volumes. Six diverted fluid waveforms are experimentally characterized and compared to sinusoidal fluid waveforms. The smallest diverted fluid volume develops the largest exergetic cooling power for each displaced volume, showing that the performance of an AMR with nested Halbach arrays can be improved with a small no-flow period when the magnetic field variation is greatest. Future works will focus on reducing unbalance effects to determine the optimum diversion ratios.

Acknowledgments

The support of the Natural Sciences and Engineering Research Council of Canada and BASF New Business is greatly appreciated.

Chapter 3

Performance evaluation of two-layer active magnetic regenerators with second-order magnetocaloric materials

Applied Thermal Engineering 106 (2016), 405-414.

Abstract

Magnetic heat pumps and cooling systems typically use a magnetocaloric material in an active magnetic regenerator (AMR) cycle for application near room temperature. One method of improving AMR performance is to layer regenerators with spatially varying Curie (or transition) temperatures. To study the impact of layering on AMR performance, four regenerator compositions comprised of two-layers are experimentally tested with interface temperature measurements. Each regenerator uses Gd as the layer with the highest Curie temperature; the second layer uses Gd and three compositions of $Gd_{1-x}Y_x$. The four regenerators are the same size and are tested using three different rejection temperatures and displaced volumes. Numerical simulations are in good agreement with the experimental results. The two-layer regenerators present the largest performance improvements for the no-load conditions and, in general, develop the peak exergetic cooling power for almost all operating conditions.

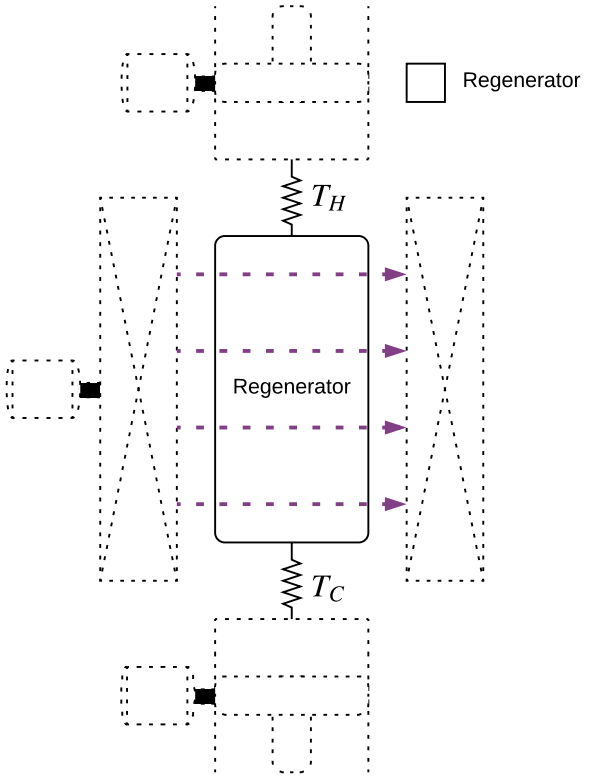

Figure 3.1: Graphical abstract of chapter 3, focusing on multilayered regenerator operation.

Nomenclature

Roman

c	specific heat capacity [J/kg-K]
$D_{\|\|}$	longitudinal thermal dispersion coefficient [-]
Ex_{q}	Exergetic cooling power [W]
h	convective heat transfer coefficient [W/m^2-K]
k	thermal conductivity [W/m-K]
P_{c}	Perimeter [m]
$\dot{q}_{\mathrm{csg}}$	Regenerator casing heat transfer [W/m^3]
$\dot{Q}_{\mathrm{c}}$	cooling capacity [W]
t	time [s]
T	temperature [K]
u	superficial (Darcy) velocity [m/s]
V_{D}	Displaced volume [cm^3]
z	axial coordinates [-]

Greek

β	surface area density [m^2/m^3]
ε	porosity [-]
ρ	density [kg/m^3]

Subscripts and Superscripts

amb	subscript of ambient
C	subscript of cold reservoir or cold side
eff	superscript of effective
f	subscript of fluid phase
H	subscript of hot reservoir or hot side
Int	subscript of layer interface
Reg	subscript of regenerator
s	subscript of solid phase
wall	subscript of the regenerator wall properties

3.1 Introduction

Magnetic heat pumps use a solid-state magnetocaloric material as the working media. Applications near room temperature typically use an active magnetic regenerator (AMR) cycle due to the limited magnetic entropy change over a narrow temperature range. Several AMR prototypes have been reported in recent years, however the pathway to commercialization requires reducing costs and size, while increasing efficiency and temperature spans [88, 13]. To reach these objectives, high performance AMRs should use low magnetic fields (smaller permanent magnet field generators) and inexpensive magnetocaloric materials [70, 17].

AMR performance can be improved by layering regenerators with spatially varying Curie (or transition) temperatures [16]. Richard *et al.* (2004) [89] compared a Gd single-layer regenerator to a Gd-$Gd_{0.74}Tb_{0.26}$ two-layer regenerator and found the latter produced larger temperature spans up to a critical cooling capacity. Zimm *et al.* (2006) [54] drew similar conclusions comparing a Gd single-layer regenerator to a Gd-$Gd_{0.94}Er_{0.06}$ two-layer regenerator. Rowe and Tura (2006) [90] presented the impact of operating parameters on the performance of a three-layer regenerator. The authors also carried out interface temperature measurements to investigate individual layer operation inside the multilayered regenerator. Engelbrecht *et al.* (2011) [91] compared a Gd regenerator to $La(Fe,Co,Si)_{13}$ single and two-layer regenerators. Tusek *et al.* (2014) [92] compared a Gd single-layer regenerator to a $La(Fe,Co,Si)_{13}$ regenerator with two, four and seven-layers. Although the best performance was found for Gd, the four-layer $La(Fe,Co,Si)_{13}$ regenerator outperformed the other compositions. Jacobs *et al.* (2014) [23] presented the performance of a six-layer $La(Fe,Co,Si)_{13}$ regenerator that demonstrated 2.5 kW of cooling power at a span of 11 C. Campbell *et al.* (2014) [93] describe experiments using layered regenerators consisting of three, six, and eight layers of $MnFeP_{1-x}As_x$. Multiple layer lengths are tested and results show significant increases in span with additional layers.

Numerical results of multilayered regenerators have been reported, and optimized parameters such as regenerator layer compositions and spatial distribution have been proposed but not experimentally tested to date [94, 95, 96]. Given the broad range of parameters affecting the performance of multilayer regenerators, a specific experimental study on the Curie temperature spacing in a two-layer regenerator can aid in the development of layered AMRs. In addition, measurements of the interface temperature (i.e., between the two layers) provide valuable information to evaluate

the performance of each layer and to validate AMR mathematical models.

In the presented work, four Gd-$Gd_{1-x}Y_x$ regenerators are evaluated with x = 0, 0.025, 0.05 and 0.075, resulting in a Gd (T_{Curie} = 17 C) single-layer and three Gd-$Gd_{1-x}Y_x$ two-layer beds (T_{Curie} = 13, 10 and 4 C). Experiments are carried out using a permanent magnet test apparatus (PM II) [52], in which the heat rejection temperature, pumped fluid volume and heat load are varied at a fixed operating frequency of 0.5 Hz. The temperature distribution and exergetic cooling power for each operating condition are reported as a function of the net cooling capacity. Finally, numerical simulations using the AMR model presented in Ref. [27] are performed and numerical predictions of interface temperature are compared to experimental values.

3.2 Experimental methods

The PM II device shown in Fig. 3.2(a) is a second generation AMR test apparatus developed at the University of Victoria [52]. The device contains two cylindrical regenerators housed in the bore of two nested concentric Halbach arrays which are de-phased by 180°. The magnetic field intensity increases from 0.06 T to a peak field strength of 1.45 T as the outer Halbach cylinder rotates around the stationary inner cylinder. The mechanical drive system synchronously rotates the Halbach arrays and a double effect pump which oscillates fluid in the regenerator beds. Outside the regenerator, a system of check valves creates unidirectional flow through the hot and cold heat exchangers. In operation, warm fluid is pumped to the hot end where heat is released, and cold fluid is pumped to the cold end where heat is absorbed.

The heat transfer fluid for the experiments described here is a mixture of water and ethylene glycol (70/30 %vol). A temperature-controlled circulator sets the temperature of the hot heat exchanger, while a heater, controlled by an external power supply, provides a thermal load at the cold heat exchanger. The average ambient temperature in the present tests is 20 C.

The regenerator housing, made of Ultem polyetherimide, is divided into hot and cold layers in which two different materials can be assembled as shown in Fig. 3.2(b). The housing has dimensions of 22.4 mm ID, 24.2 mm OD and each layer is 65.0 mm long (130 mm total length). The magnetocaloric matrix consists of packed spheres with a particle diameter of 300-600 μm (450 μm average) and a porosity of 0.36. The total mass of magnetocaloric material ranges from 120 to 130 g per layer (500 to 520 g total), since the $Gd_{1-x}Y_x$ alloys have a slightly lower density than Gd. Temperature

measurements are performed at the hot and cold ends of the bed to characterize the regenerator temperature span. In addition, an interface thermocouple is inserted between the layers.

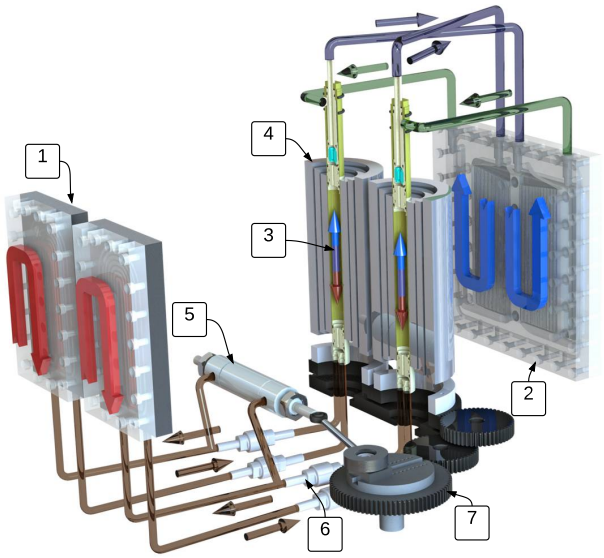

(a)

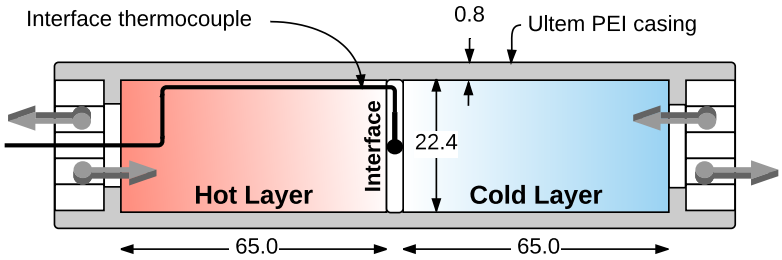

(b)

Figure 3.2: (a) PM II schematic showing (1) hot heat exchanger, (2) cold heat exchanger, (3) regenerator, (4) nested Halbach cylinders, (5) double effect pump, (6) check valves, (7) drive system; (b) Regenerator assembly for testing two-layer beds of packed spheres with interface temperature measurements. The thermocouple runs through the hot layer matrix.

As presented in Table 3.1, four different regenerator configurations are tested. In all the tests, the hot layer is composed of the same Gd matrix while the four $Gd_{1-x}Y_x$ alloys are alternated in the cold layer. $Gd_{1-x}Y_x$ has a similar magnetocaloric effect to Gd with shifted Curie temperatures [95]. Throughout the paper, the regenerators will be referred to by the naming convention given in the Table. ***R1*** indicates two Gd layers (single material regenerator), and ***R2-R4*** represent the Gd-$Gd_{1-x}Y_x$ regenerators where the spacing between Curie temperatures grows for each.

Table 3.1: Multi-layered regenerator compositions.

Parameter	Regenerator Compositions			
	R1	***R2***	***R3***	***R4***
Hot layer material	Gd	Gd	Gd	Gd
Hot layer T_{Curie} (C)	17	17	17	17
Cold layer material	Gd	$Gd_{0.975}Y_{0.025}$	$Gd_{0.95}Y_{0.05}$	$Gd_{0.925}Y_{0.075}$
Cold layer T_{Curie} (C)	17	13	10	4
T_{Curie} spacing (C)	0	4	7	13

The experiments are carried out using the operating conditions presented in Table 3.2. Operating frequency is fixed at 0.5 Hz while the displaced volume, hot side temperature and heat load are varied. The largest displaced volume (13.9 cm^3) is chosen to ensure that the absolute pressure remains below the maximum design pressure of 10 bar. The heat rejection temperatures are set between 15 and 25 C, which are above and below the Curie temperature of the hot (Gd) layer. The applied heat load is changed from 0 (no load) to 40 W, in steps of 10 or 20 W depending on the operating conditions. In some cases, the maximum load of 40 W is larger than the maximum cooling capacity so these tests are not performed.

Table 3.2: Experimental conditions for each regenerator.

Displaced Volume (cm^3)	Heat Load (W)	Hot side temperature (C)
6.95	0, 10, 20	15, 20, 25
10.42	0, 10, 20, 30	15, 20, 25
13.9	0, 20, 40	15, 20, 25

For all the displaced volumes, the experiments start with no applied load at a rejection temperature of 25 C. After reaching periodic steady-state, the data are recorded and the hot reservoir temperature is changed (e.g., to 20 C) for the same no-load condition. This procedure repeats for each applied load after the three hot heat exchanger temperatures are complete. Periodic steady-state is assumed when

the average temperature span changes less than 0.09 C over 12 minutes. This criterion is reached within three hours and introduces a maximum error of 0.65 C with the smallest displaced volume of 6.95 cm^3 and the largest hot side temperature of 25 C.

3.3 Mathematical formulation

The numerical simulations are performed using the one-dimensional numerical model in Ref. [27]. The mathematical model is composed of the one-dimensional Brinkman-Forchheimer equation for momentum transfer in porous media coupled with energy balance equations for the solid (Eq. 3.1) and fluid (Eq. 3.2) phases.

The solid phase energy equation is [82]:

$$\rho_{\mathrm{s}} c_{\mathrm{s}} (1-\varepsilon) \frac{\partial T_{\mathrm{s}}}{\partial t} = h\beta (T_{\mathrm{f}} - T_{\mathrm{s}}) + (1-\varepsilon) k_{\mathrm{s}}^{\mathrm{eff}} \frac{\partial^2 T_{\mathrm{s}}}{\partial z^2} \tag{3.1}$$

where the term on the left accounts for thermal inertia in the solid, and the terms on the right are due to interstitial heat convection and axial heat conduction, respectively. T_{f} is the fluid temperature and T_{s} is the solid temperature, ρ_{s} is the density of the solid, c_{s} is the specific heat capacity of the solid and $k_{\mathrm{s}}^{\mathrm{eff}}$ is the effective thermal conductivity of the solid phase.

The fluid phase energy equation is given by [82]:

$$\rho_{\mathrm{f}} c_{\mathrm{f}} \left(\varepsilon \frac{\partial T_{\mathrm{f}}}{\partial t} + u \frac{\partial T_{\mathrm{f}}}{\partial z} \right) = h\beta (T_{\mathrm{s}} - T_{\mathrm{f}}) + \varepsilon \left[\kappa_{\mathrm{f}}^{\mathrm{eff}} + \rho_{\mathrm{f}} c_{\mathrm{f}} D_{||} \right] \frac{\partial^2 T_{\mathrm{f}}}{\partial z^2} + \left| u \frac{\partial P}{\partial z} \right| + \dot{q}_{csg} \tag{3.2}$$

where the term on the left is due to inertial effects and the terms on the right are, respectively, the interphase heat transfer calculated via a convective heat transfer coefficient (h), longitudinal advection term, axial conduction term and viscous dissipation term. ρ_{f} is the fluid density, c_{f} is the specific heat capacity of the fluid, $k_{\mathrm{f}}^{\mathrm{eff}}$ is the effective thermal conductivity of the fluid phase and $D_{||}$ is the longitudinal thermal dispersion.

In addition, $\dot{q}_{csg}$ is the casing heat transfer loss term:

$$\dot{q}_{csg} = -h_{\mathrm{wall}} \frac{P_{\mathrm{c,Reg}}}{A_{\mathrm{c,Reg}}} (T_{\mathrm{f}} - T_{\mathrm{wall}}) \tag{3.3}$$

where h_{wall} is the internal wall heat transfer coefficient [97, 87], $P_{\mathrm{c,Reg}}$ is the regener-

ator internal perimeter, $A_{c,Reg}$ is the regenerator cross sectional area and T_{wall} is the internal wall temperature. T_{wall} is calculated by solving the two-dimensional transient conduction equation for the regenerator wall and the air gap between the regenerator housing and the magnet. The regenerator housing wall thickness is 0.8 mm and the air gap thickness is 0.1 mm. The Ultem polyetherimide housing has a thermal conductivity, density and specific heat capacity of 0.22 W/m-K, 1270 kg/m^3 and 2000 J/kg-K, respectively. The magnetic circuit is assumed to be in thermal equilibrium with the external environment at room temperature. Eq. 3.1, Eq. 3.2 and Eq. 3.3 are coupled and solved in a iterative loop. More details about the mathematical formulation, boundary conditions and solver procedure can be found in Ref. [27].

The discrete implementation of the adiabatic temperature change is used and demagnetizing losses are included [98]. The rectified sinusoidal waveform, characteristic of nested Halbach cylinders, is used for the time varying magnetic field [52, 76] and a sinusoidal fluid flow waveform is simulated. Experimental magnetocaloric and thermophysical properties of Gd (density, thermal conductivity and specific heat) are used for all of the $Gd_{1-x}Y_x$ layers by shifting the transition temperature. This is a first approximation to evaluate the performance of $Gd_{1-x}Y_x$ alloys in a multilayer regenerator [95], and as will be discussed later, is reasonable for low Yttrium contents and when the experimental magnetocaloric and thermophysical properties are unavailable.

3.4 Results

3.4.1 Experimental results

The temperature span as a function of cooling capacity for each regenerator composition (***R1***-***R4***, see Table 3.1) is shown in Fig. 3.3. Each window presents a combination of displaced volume (V_D) and hot reservoir temperature (T_H), and each curve indicates a different regenerator composition. The total temperature span arises from contributions by each layer - the blue bars indicate the cold layer span and the red bars indicate the hot layer span. The calculated uncertainty is 2% for the applied thermal load (cooling capacity), evaluated from the resistance and voltage uncertainty in a Fluke multimeter, and 1.5 C for the temperature span, which includes the two thermocouple errors of 0.5 C and the steady state error. The uncertainties are evaluated according to Ref. [85].

Preliminary inspection of Fig. 3.3 reveals how the hot and cold layers can develop different temperature spans. Depending on the operating conditions, the cold layer can have a larger temperature span than the hot layer (and vice-versa). For example, for T_H = 15 C and V_D = 6.95 cm^3 ***R4*** gives the largest no-load temperature span ($\approx$ 12 C). In this case, the cold layer span is close to 8.5 C versus 4.5 C for the hot layer. In some cases, the total and hot layer temperature spans are positive while the cold layer span is negative - see case ***R4*** for T_H = 25 C, V_D = 6.95 cm^3 and 10 W cooling capacity. A negative cold layer span means that the temperature measured at the interface between the layers is lower than the temperature at the cold end. In this situation, the temperature distribution in the regenerator is nonlinear between T_H and T_C. Finally, in some cases the total temperature span is negative (i.e., $T_C > T_H$) even with positive layer spans, see cases ***R3***-***R4*** for T_H = 20 C and V_D = 6.95 cm^3, for 20 W cooling capacity.

For a fixed hot side temperature (e.g., 15 C) and fixed temperature span, the cooling capacity increases with V_D. The maximum temperature span also increases with V_D, and a maximum is found at 13.9 cm^3. For a fixed displaced volume (e.g., 13.9 cm^3) and fixed cooling capacity, the temperature span increases with T_H for the tested conditions. This can be explained by better activation of the hot-layer given the Curie temperature and the range of T_H values considered, as can be observed following the red bars in Fig. 3.3. The cold layer span tends to decrease as T_H increases, especially for load tests and for the $Gd_{1-x}Y_x$ cold layer cases (***R2*** - ***R4***).

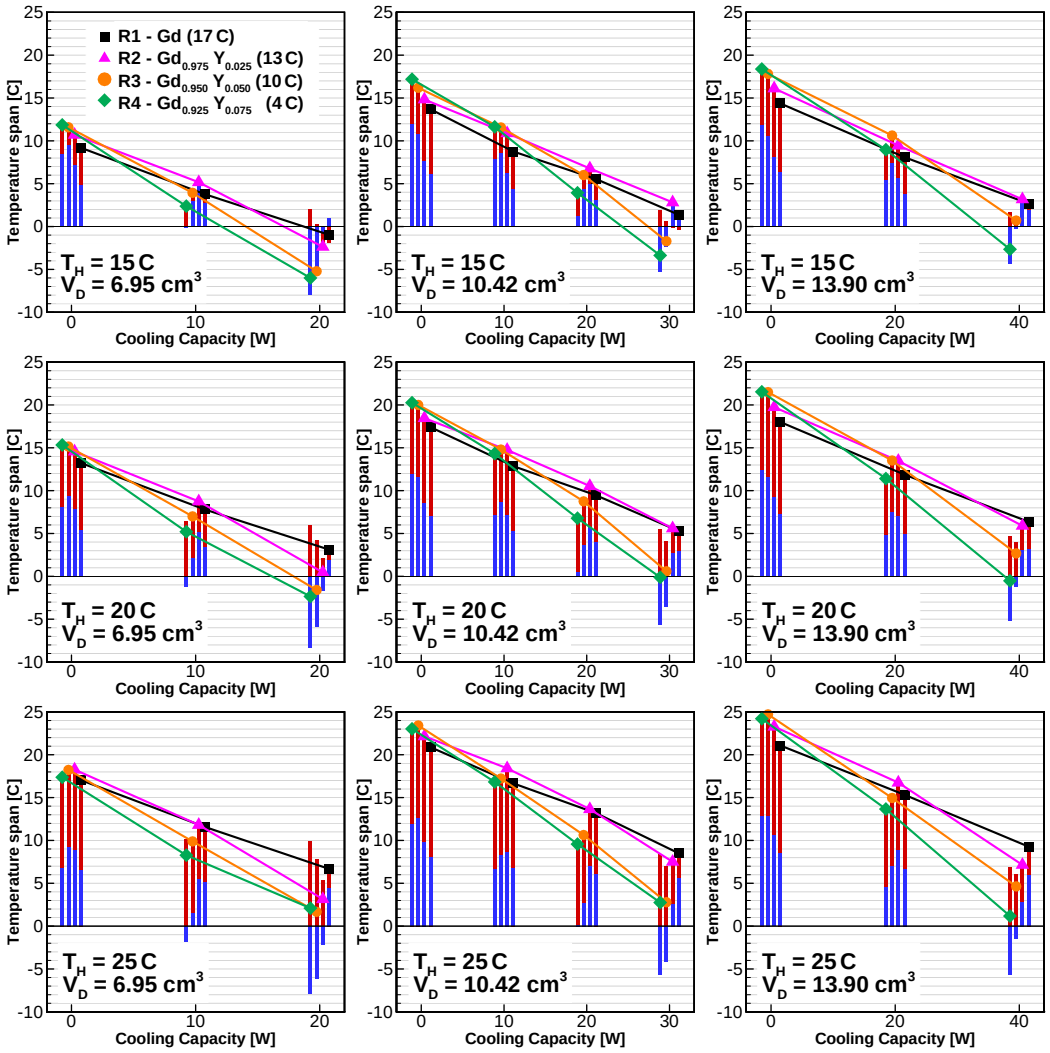

Figure 3.3: Temperature span vs. cooling capacity curves for different operating conditions and different regenerator configurations: (i) ***R1*** - Gd single-layer; (ii) ***R2*** - Gd-$Gd_{0.975}Y_{0.025}$ two-layer; (iii) ***R3*** - Gd-$Gd_{0.95}Y_{0.05}$ two-layer; (iv) ***R4*** - Gd-$Gd_{0.925}Y_{0.075}$ two-layer.

Fig. 3.4 shows the experimental average temperatures as a function of the cooling capacity for all operating conditions. The different symbols identify regenerator compositions (***R1*** - ***R4***). Blue and red symbols represent cold and hot side measured temperatures, respectively, while black symbols are the temperatures measured at the interface. In addition, the colored horizontal lines show the transition temperatures for each material, as described in the legend of Fig. 3.4.

From the results in Fig. 3.4, it is clear that the highest spans are developed when the local transition temperature is between the hot and cold temperatures of a layer.

All four regenerators (***R1*** to ***R4***) show that at a given cooling capacity, the hot layer span is minimized when producing the maximum overall temperature span. For example, in Fig. 3.4, see T_{H} = 25 C, V_{D}= 10.42 cm^3 and 0 W cooling capacity. In this case, the largest temperature span is obtained for ***R3*** which has the smallest hot layer temperature span of ***R1*** to ***R4***. In almost all of the maximum temperature span cases, the hot and cold layer spans are similar creating a nearly linear average temperature gradient. Comparing the results for ***R3*** and ***R4*** from Fig. 3.3 and Fig. 3.4, in general, regenerator ***R3*** outperforms ***R4*** even for the maximum temperature span (0 W). This result can be explained by ***R3*** operating closer to its transition temperature than ***R4***.

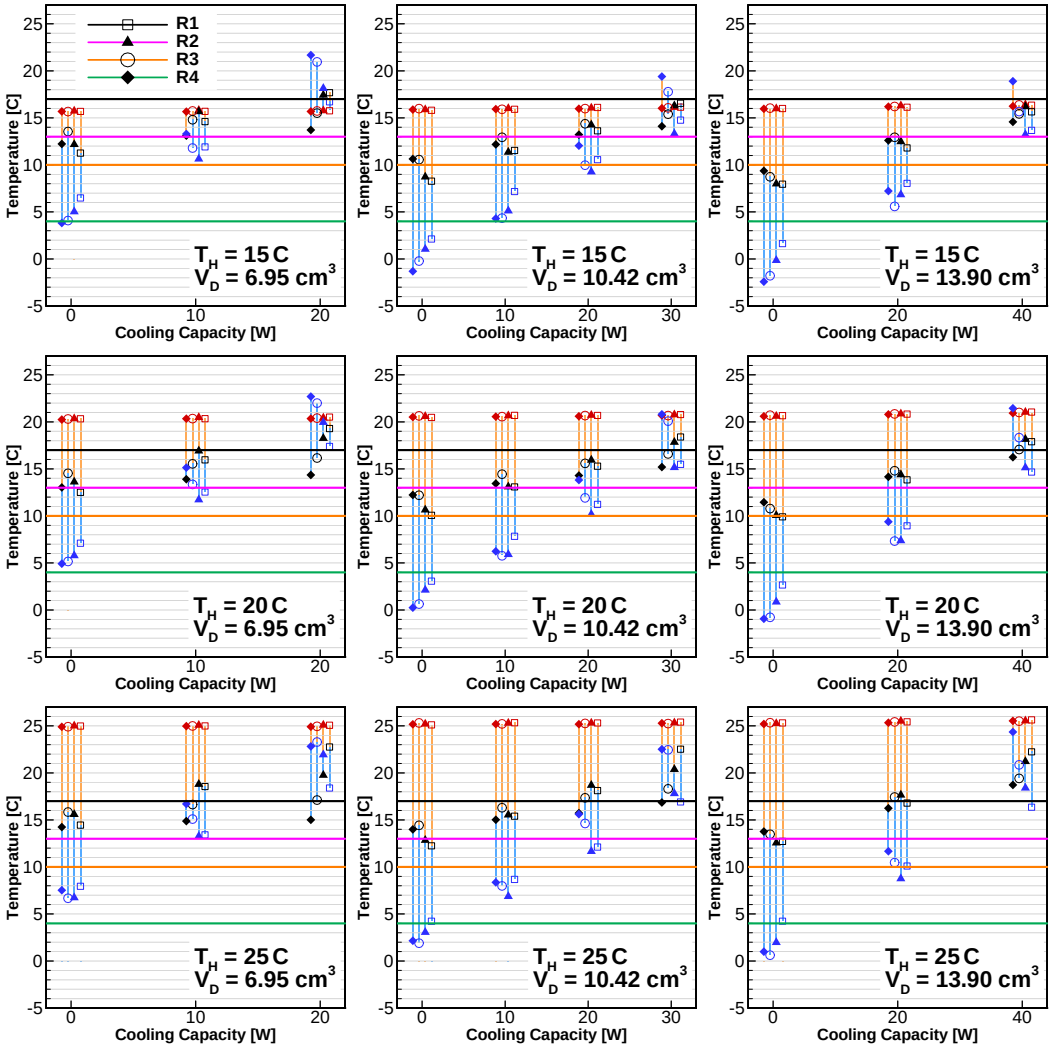

Figure 3.4: Temperature vs. cooling capacity curves for different operating conditions and different regenerator configurations: (i) ***R1*** - Gd single-layer; (ii) ***R2*** - Gd-$Gd_{0.975}Y_{0.025}$ two-layer; (iii) ***R3*** - Gd-$Gd_{0.95}Y_{0.05}$ two-layer; (iv) ***R4*** - Gd-$Gd_{0.925}Y_{0.075}$ two-layer. Blue and red symbols refer to cold and hot side measured temperatures, respectively, and the black symbols are the temperature measured at the interface.

An alternative representation of performance is possible based on the exergetic equivalent cooling power (Ex_{Q}), defined as:

$$Ex_{\mathrm{q}} = \dot{Q}_{\mathrm{C}}\left(\frac{T_{\mathrm{H}}}{T_{\mathrm{C}}} - 1\right) = \dot{Q}_{\mathrm{C}}\frac{T_{\mathrm{span}}}{T_{\mathrm{C}}} \tag{3.4}$$

Fig. 3.5 shows the exergetic cooling power as a function of the cooling capacity. It is important to note that the range of the x-axis varies when comparing results for different displaced volumes. In general, the maximum exergetic power increases with displaced volume and hot side temperature. Comparing the different cases (***R1*** to ***R4***), the $Gd_{1\text{-}x}Y_x$ regenerators perform best at the intermediate cooling capacities for almost all cases. For instance, ***R3*** presents a peak of 0.8 W for $T_{\mathrm{H}} = 15$ C, $V_{\mathrm{D}} = 13.9$ cm^3 and $\dot{Q}_{\mathrm{C}} = 20$ W, while for $T_{\mathrm{H}} = 25$ C, $V_{\mathrm{D}} = 13.9$ cm^3 and $\dot{Q}_{\mathrm{C}} = 20$ W the peak is found for ***R2***. The single material regenerator (***R1***), however, presents the highest exergetic cooling power of 1.3 W, for $T_{\mathrm{H}} = 25$ C, $V_{\mathrm{D}} = 13.9$ cm^3 and $\dot{Q}_{\mathrm{C}} = 40$ W.

3.4.2 Numerical results

Fig. 3.6 compares the numerical (solid lines) and experimental (symbols) results for the temperature span as a function of the hot reservoir temperature. The different symbols and line colors stand for the different cooling capacities defined in the figure legend. Each row of figures represents a particular regenerator (***R***) and each column represents a displaced volume. It is important to note that the numerical results include the heat leaks through the regenerator casing (as explained in Section 3.3), but other external heat leaks, such as in the cold side tubing and the cold heat exchanger thermal mass, are not included in the simulations. Gd experimental properties are assumed for the $Gd_{1\text{-}x}Y_x$ regenerators (***R2***- ***R4***) where the temperature dependence of properties are assumed to scale by the Curie temperature of each composition (Table 3.1).

In general, the simulations align with the experimental results with a systematic over-prediction of performance. For example with case ***R1*** and V_{D}= 6.95 cm^3, the numerical results for temperature span are about 10 W higher than experimental results, i.e., the numerical 10 W curve coincides with the experimental 0 W curve, while the numerical 20 W curve coincides with the experimental 10 W curve. This offset is observed for all of the results. Furthermore, the numerical and experimental differences are more pronounced at the lower displaced volumes. This behavior can

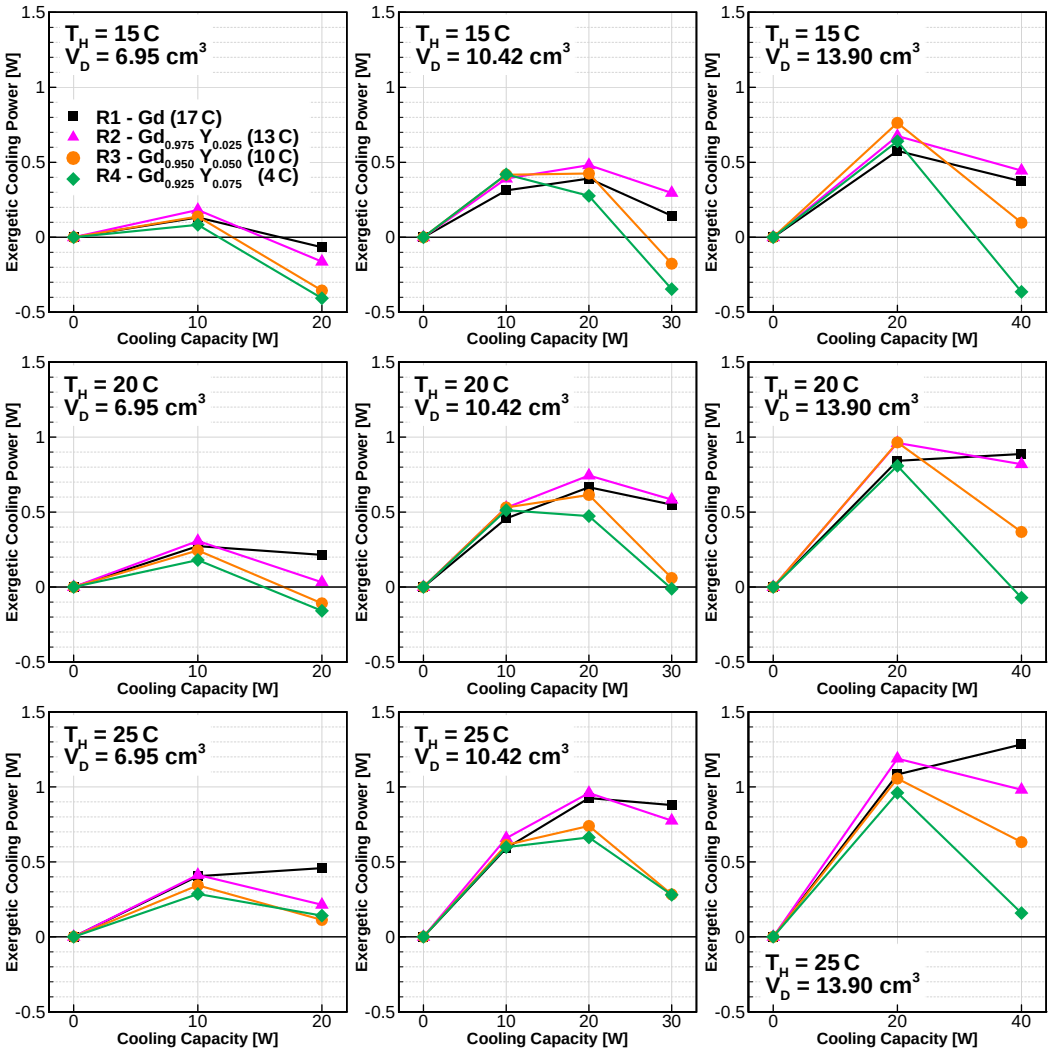

Figure 3.5: Exergetic cooling power vs. cooling capacity curves for different operating conditions and different regenerator configurations: (i) ***R1*** Gd single-layer; (ii) ***R2*** Gd-$Gd_{0.975}Y_{0.025}$ two-layer; (iii) ***R3*** Gd-$Gd_{0.95}Y_{0.05}$ two-layer; (iv) ***R4*** Gd-$Gd_{0.925}Y_{0.075}$ two-layer.

be explained by heat leaks to the cold side heat exchanger which will tend to be more significant at smaller mass flow rates [27, 83]. Finally, as the amount of Yttrium increases (cases ***R3*** and ***R4***), the differences between numerical and experimental results are more visible. This suggests that the properties of $Gd_{1-x}Y_x$ are not well represented by shifted Gd properties as the Yttrium content increases.

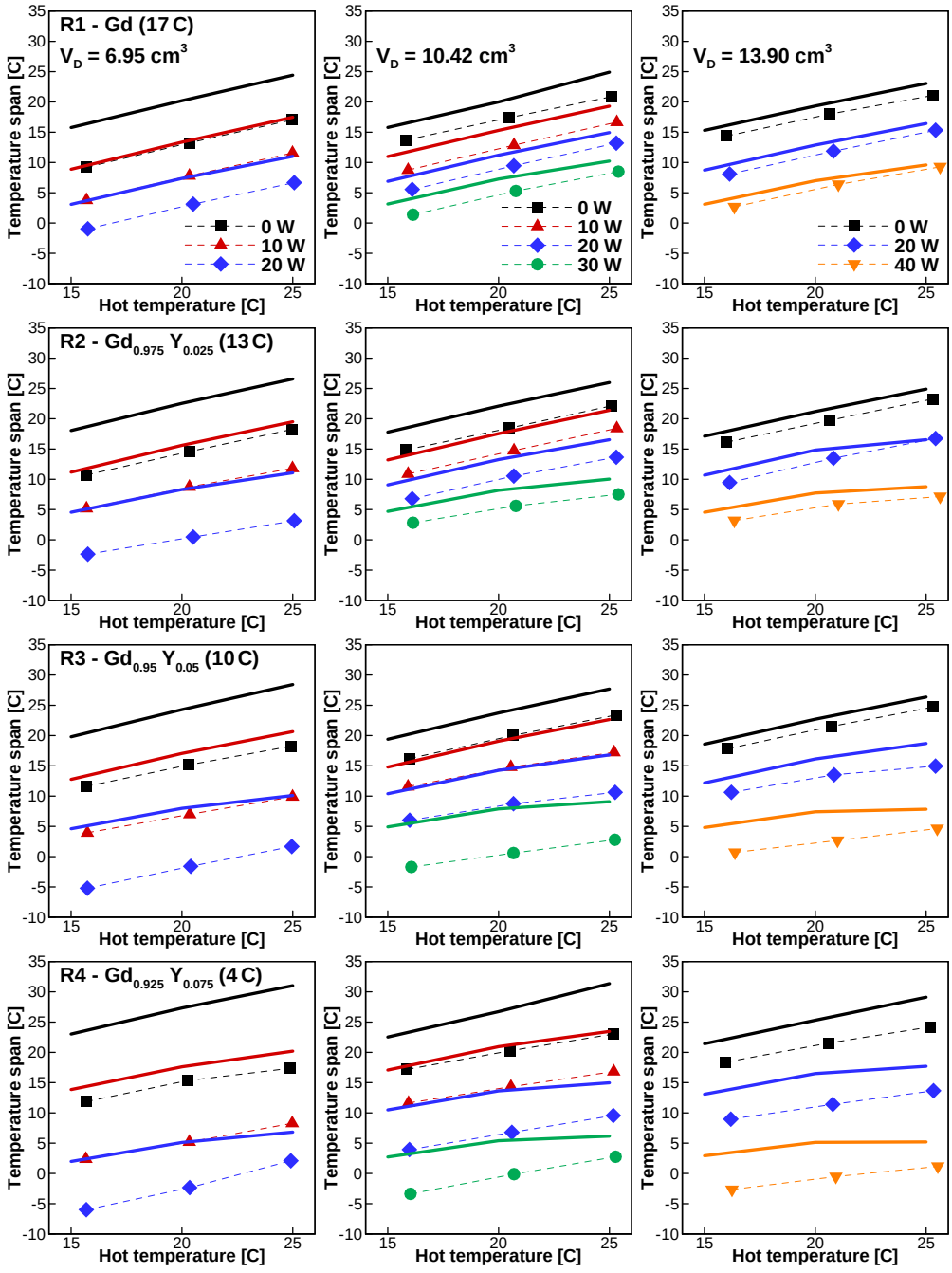

Figure 3.6: Comparison of numerical and experimental results for the temperature span as a function of the hot reservoir temperature for different regenerator compositions and operating conditions.

Fig. 3.7 compares the numerical and experimental results for the cold and hot layer spans as a function of the hot reservoir temperature for a fixed pumped volume of 10.42 cm^3 and different cooling capacities. The first column is the total span, the middle column is the warm layer span, and the final column is the cold layer span. While not shown, similar trends appear for the other pumped volumes. The numerical and experimental hot layer spans are in very good agreement especially for cases ***R1*** and ***R2***. The cold layer spans show more significant differences, which can be attributed to uncertainty in properties and increased heat leaks due to the cold layer operating significantly below ambient temperature. In terms of the different regenerator compositions (***R1*** to ***R4***):

- The hot layer span increases as T_H increases for all the applied loads and regenerator compositions.
- The trend for the cold layer span, with respect to T_H, changes depending on the applied load and the regenerator composition. For example, the cold layer span at 0 W for regenerator ***R4*** increases with T_H, while for 20 W the cold layer span decreases as T_H increases. This depends on if the cold layer temperature moves towards (***R1***) or away (***R4***) from the layer Curie temperature with a change in T_H or applied load.
- Increasing the Curie temperature spacing increases the sensitivity of the cold layer span to cooling capacity, while the load sensitivity of the hot layer span decreases.

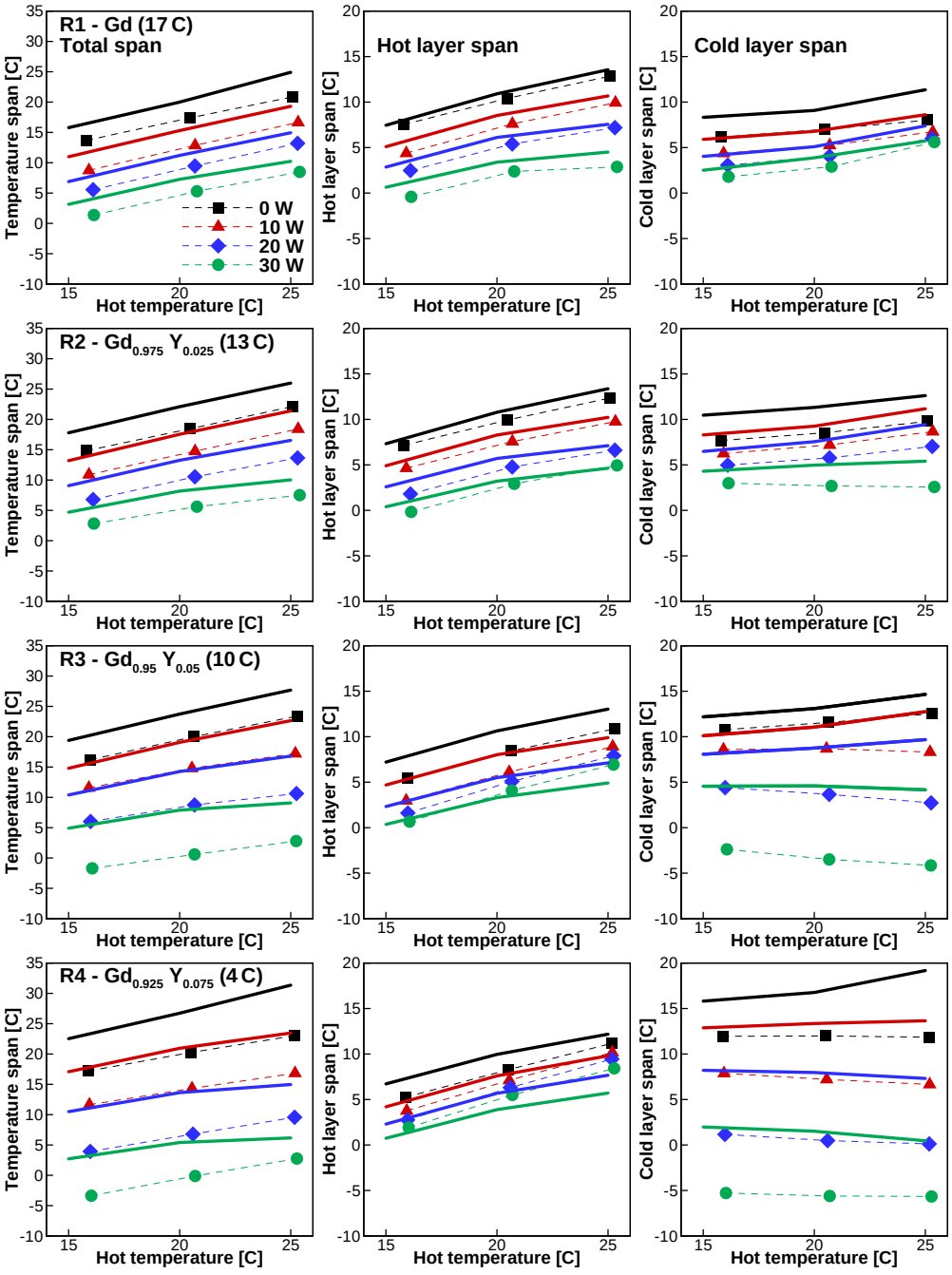

Figure 3.7: Numerical and experimental results comparison for the layer temperature span as a function of the hot reservoir temperature for different regenerator composition and V_D= 10.42 cm^3.

Fig. 3.8(a) presents the average temperature gradient along the regenerator, for the dimensionless positions 0 (cold side), 0.5 (interface) and 1 (hot side). Two different scenarios are evaluated with a displaced volume of 6.95 cm^3: (i) the red square symbols and red solid line stands for ***R1*** and T_H = 15 C; (ii) the blue round symbols and blue solid line stands for ***R4*** and T_H = 25 C. In the first scenario, T_H is less than ambient temperature (20 C) while in the second scenario T_H is greater than ambient. For scenarios (i) and (ii) the experimental data is for a cooling capacity of 20 W, whereas for the purpose of comparing heat leak effects, the numerical data are for the maximum cooling capacity of 22.5 W for (i) and 24.2 W for (ii). As such, the following observations are made:

- For scenario (i), although the hot layer span is negative ($T_H < T_{int}$) and the cold layer span is positive ($T_{int} > T_C$), the regenerator span is negative ($T_H < T_C$) as seen in Fig. 3.6;
- For scenario (ii) the hot layer span is positive ($T_H > T_{int}$) while the cold layer span is negative ($T_{int} < T_C$), however, the regenerator span is positive ($T_H > T_C$);

For both scenarios, the average temperature gradient along the regenerator is non-linear, in which the interface temperature tends to be drawn to T_{amb}. This behavior is observed in the experimental and numerical results and can be directly associated with the heat leaks/gains through the regenerator housing. Fig. 3.8(b) presents scenario (i) again, but compares the simulations with (red solid line) and without (dashed black line) heat leaks through the regenerator housing. For the no loss results, a nearly linear average temperature profile along the regenerator is found, but as the heat leaks are included, the interface temperature tends to T_{amb} which is in agreement with the experimental measurements.

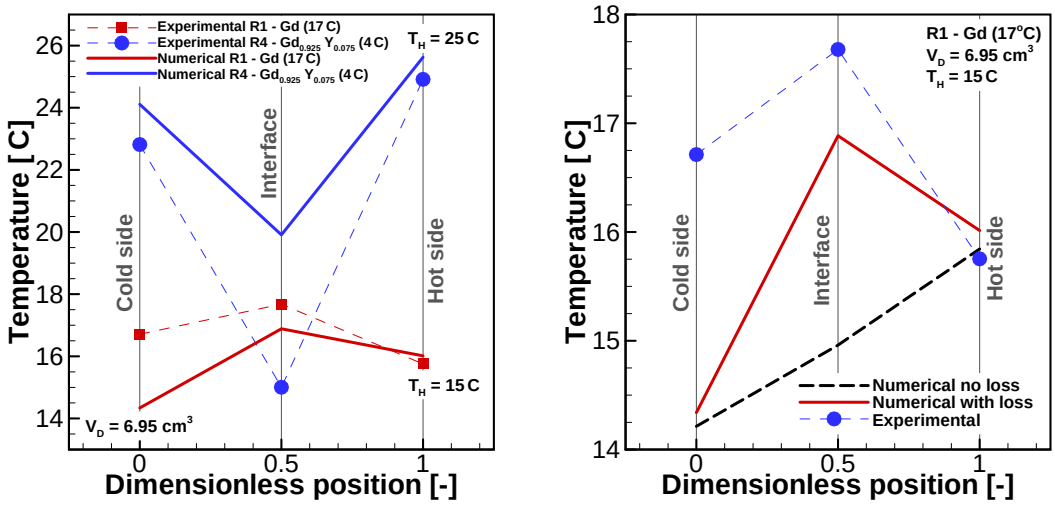

(a) (b)

Figure 3.8: Comparison of numerical and experimental results for the average temperature gradient along the regenerator, for the dimensionless positions 0 (cold side), 0.5 (interface) and 1 (hot side). Two different cases are considered. (a): (i) the red square symbol and red solid line stands for R1 regenerator and $T_{\mathrm{H}} = 15$ C and (ii) the blue round symbol and blue solid line for ***R4*** case with $T_{\mathrm{H}} = 25$ C. For scenarios (i) and (ii) the experimental data is evaluated for a cooling capacity of 20 W, while the numerical data stands for the maximum cooling capacity (22.5 W for (i) and 24.2 W for (ii)). (b) comparing the simulations performed with (red solid line) and without (dashed black line) the heat leaks through the regenerator housing for ***R1*** and $T_{\mathrm{H}} = 15$ C.

3.5 Discussion

All $Gd_{1-x}Y_x$ regenerators (***R2*** to ***R4***) develop higher maximum temperature spans than the single-layer Gd regenerator (***R1***). This improvement arises for multilayer regenerators when appropriate Curie temperature spacing is used. In ***R1***, the MCE decreases when operating at temperatures away from the Gd Curie point. Hence, replacing the Gd cold layer (***R1***) with $Gd_{1-x}Y_x$ (***R2*** to ***R4***), it is possible to increase the MCE when the cold layer temperature range is in the vicinity of the transition temperature of the $Gd_{1-x}Y_x$ cold layer material. Conversely, as the cooling capacity increases and the temperature span decreases, the regenerator operating range moves towards the Gd transition temperature. As a result, ***R1***, in general, developed the highest temperature span at the largest cooling capacity, as in Fig. 3.3 and Fig. 3.4.

The largest performance improvements for multilayer regenerators are obtained for the no-load conditions and, in general, the peak exergetic cooling power is found for the layered regenerators. Compared to the Gd single material regenerator (***R1***), the multilayer exergetic performance improvements are small. This is mainly due to three factors. First, the exergetic cooling power is calculated using the applied load, where the actual heat transfer through the regenerator is the gross power which includes parasitic heat leaks. By using the applied load to calculate exergy, the regenerator is penalized for system problems [83]. This somewhat masks the benefits of the layered cases at the larger spans where there is in fact a load, but it is due to the parasitic heat leaks. Improving thermal isolation will more clearly show the benefits of the layered regenerators where they provide higher spans. Second, the MCE slowly decreases for second-order materials as temperature deviates from the Curie point. One could expect a much higher improvement when first-order materials are layered. Finally, discontinuous thermophysical properties between the layers introduces irreversibilities.

3.6 Conclusions

To study the impact of multilayering on AMR performance, four regenerator compositions are compared: one single-layer Gd (T_{Curie} = 17 C) (***R1***) and three two-layer regenerators Gd-$Gd_{1-x}Y_x$ (T_{Curie} = 13, 10 and 4 C) (***R2***- ***R4***). In all the cases, the hot layer material is fixed (Gd) while the cold layer is changed to different Gd or $Gd_{1-x}Y_x$ alloys. The experimental tests are carried out in the PM II apparatus with interface temperature measurements for different rejection temperatures (15 to 25 C), displaced volumes and heat loads (0 to 40 W) at a fixed operating frequency of 0.5 Hz. A maximum no-load temperature span of 24.7C is found with Gd-$Gd_{0.95}Y_{0.05}$ (***R3***), while a maximum exergetic cooling power of 1.28 W is obtained for the Gd single layer (***R1***) at T_{H} = 25 C and V_{D}= 13.9 cm^3. Numerical results are in good agreement with the experimental results. The two-layer regenerators present the largest performance improvements for the no-load conditions and, for almost all operating conditions, ***R2*** and ***R3*** develop the peak exergetic cooling power.

Acknowledgments

The support of the Natural Sciences and Engineering Research Council of Canada and BASF New Business is greatly appreciated.

Chapter 4

Semi-analytic AMR element model

Applied Thermal Engineering 128 (2018), 1022-1029.

Abstract

The active magnetic regenerator (AMR) cycle has the potential to reduce energy consumption and mitigate environmental pollutants. While layering regenerators with spatially varying Curie (or transition) temperatures has been shown to significantly increase AMR performance, layering strategies have yet to be developed. A central issue is the need for a modeling tool capable of efficiently screening the problems parameter space. A semi-analytic AMR element model is developed and validated with experiments over a broad range of operating conditions and regenerator compositions using second-order magnetocaloric materials. An optimization is performed and a temperature span of 40 K is measured in close proximity to the simulated optimum.

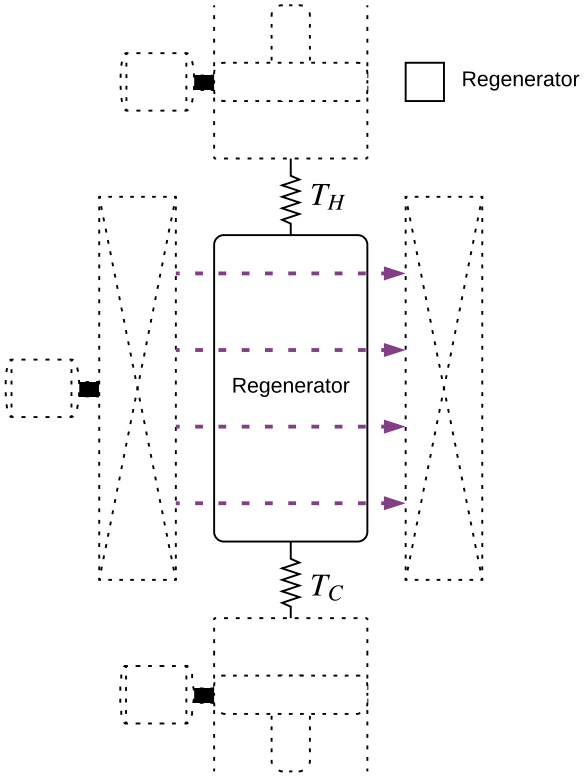

Figure 4.1: Graphical abstract of chapter 4, focusing on the simulation and optimization of multilayered regenerators.

Nomenclature

Roman

B	magnetic flux density [T]
c	specific heat [J kg^{-1} K^{-1}]
$\dot{E}x_{\mathrm{Q}}$	exergetic cooling power [W]
f	operating frequency [Hz]
m	mass [kg]
$\mathrm{n_{reg}}$	number of regenerators[-]
N_{D}	demagnetization factor[-]
$\dot{Q}_{\mathrm{c}}$	cooling capacity [W]
R	thermal mass ratio [-]
s	entropy [J kg^{-1} K^{-1}]
T	temperature [K]
V	Volume [m^3]

Greek

ϵ	regenerator porosity [-]
κ	effective thermal conductivity [-] or thermal conductance [W/K]
Φ	utilization [-]
ρ	density [kg m^{-3}]
σ	specific magnetization [A m^2 kg^{-1}]
μ_0	permeability of free space [H m^{-1}]
ζ	reduced magnetocaloric effect [-]

Subscripts and Superscripts

ad	adiabatic
AMR	Active Magnetic Regenerator
app	applied
OC	ambient-to-cold
C	cold reservoir or cold side
Curie	Curie or transition temperature
D	displaced
f	fluid
H	hot reservoir or high field
HC	hot-to-cold
I	interface
int	internal
L	low field
M	magnetic
p	constant pressure, pump or parasitic
s	solid
span	temperature span

4.1 Introduction

Magnetic heat pumps using solid-state magnetocaloric materials (MCM) have the potential to reduce energy consumption and mitigate environmental pollutants [13]. Applications near room temperature typically use an active magnetic regenerator (AMR) cycle to overcome the limited magnetic entropy change of magnetocaloric materials [16]. While AMR systems still face technical challenges [17, 22], performance can be improved by layering regenerators with spatially varying Curie (or transition) temperatures [12].

Jacobs *et al.*(2014) [23] presented the performance of a six-layer La(Fe,Co,Si)$_{13}$ regenerator demonstrating 2.5 kW of cooling power at a temperature span of 11 K. Govindappa *et al.*(2017) [99] investigated MnFeP$_{1-x}$As$_x$ multilayer regenerators and measured a no-load temperature span of 32 K. While experimental [89, 54, 90, 55, 91, 100, 92, 101] and numerical [102, 95, 103, 104, 105, 106, 107] multilayering studies have shown promising performance improvements, optimum layering strategies for specific performance goals have not been developed. Simplified modeling tools can play a role by efficiently identifying promising regions in an extensive parameter space. Solutions to the reduced problem can then be further refined using more sophisticated modeling tools and AMR devices.

The present work continues the analysis of multilayered AMRs using second-order magnetocaloric materials previously described using experimental and numerical methods [1, 79]. A flexible and computationally efficient modeling tool is developed and validated with four regenerator compositions tested over a wide range of operating parameters. The validated model is coupled with a hybrid optimization algorithm to analyze design modifications. An optimized design vector maximizing the no-load temperature span is then implemented and tested in a subsequent experimental investigation.

4.2 Model description

The following sections present the energy balance equations for the semi-analytic AMR element model and the constitutive relations describing magnetocaloric material properties. The model is implemented in Python using the open-source SciPy package [108].

4.2.1 Semi-analytic AMR model

State-of-the-art AMR models numerically solve the coupled energy equations for the solid and fluid phases [18, 109, 110, 111, 112]. Using this methodology, Tusek *et al.* (2011) [113] optimized the displaced volume, frequency and sphere diameter of a gadolinium AMR. Park *et al.* (2015) [103] optimized a multilayer regenerator composition for a specific cryogenic device, and Bjørk *et al.* (2016) [71] found the geometry, Halbach cylinder and operating conditions of a gadolinium regenerator that minimized cost for a defined operating scheme. Using a new methodology, Aprea *et al.* (2017) [114] trained an artificial neural network with experimental data to control frequency and displaced volume. While these works identified performance improvements, the convergence time of numerical AMR models using readily available computational hardware limits the parameter space that can be explored. Furthermore, the necessity of training data limits the scope of machine learning algorithms. Non-linearities and the complexity of coupled phenomena can also complicate the interpretation of simulated results.

Rowe (2012) [115, 116] proposed the use of analytical expressions to describe the magnetic work and cooling power in an AMR. These expressions were obtained under the assumption of local thermal equilibrium between the solid and fluid phases in the regenerator matrix, which results in a single differential energy equation for the porous media [82]. An effective conductivity incorporating finite convection accounts for non-equilibrium between solid and fluid. In addition, an effective specific heat and reduced adiabatic temperature change are used. The derived magnetic work and cooling power expressions yield a fast solution and have been validated with a number of experimental devices. Using the formulation presented by Burdyny *et al* (2014) [117], the cooling power of a material undergoing an AMR cycle is:

$$\dot{Q}_{\mathrm{C,AMR}} = m_{\mathrm{s}} c_{\mathrm{s}} f \zeta T_{\mathrm{C}} \left(\frac{\Phi}{R}\right) \left[1 - \left(\frac{\Phi}{2R} + \left(\frac{\Phi\zeta}{R\kappa}\right)^{-1}\right)\left(\frac{T_{\mathrm{H}}}{T_{\mathrm{C}}} - 1\right)\right] \tag{4.1}$$

where m_{s} is the mass of magnetocaloric material, c_{s} is the effective solid specific heat, f is the operating frequency, T_{H} and T_{C} are the hot and cold temperatures on the boundaries of the regenerator and ζ is defined as the *effective* reduced adiabatic temperature change ($\Delta T_{ad}/T$). Utilization (Φ) is a measure of the displaced fluid volume in a regenerative blow and is defined as the ratio of the fluid to solid thermal mass:

$$\Phi = \frac{m_{\mathrm{d}} c_{\mathrm{p}}}{m_{\mathrm{s}} c_{\mathrm{s}}} \tag{4.2}$$

where m_{d} is the mass of displaced fluid and c_{p} is the average fluid specific heat. The term *semi-analytic* stems from a modification proposed by Burdyny *et al* (2014) to include the thermal mass ratio (R):

$$R = 1 + \frac{m_{\mathrm{f}} c_{\mathrm{p}}}{m_{\mathrm{s}} c_{\mathrm{s}}} \tag{4.3}$$

where m_{f} is the entrained fluid mass in the pores. κ is the effective thermal conductivity which contains a contribution from thermal diffusion and a degradation factor to account for finite convective heat transfer. Further implementation details can be found in Ref. [117].

The net work input, $\dot{W}_{\mathrm{net}}$, is the sum of the magnetic and pump work, where the latter is based on the average pressure drop. In the case of particle beds, pressure drop is numerically estimated using Ergun's relation (1952) [80]. The semi-analytic expression for magnetic work is given by:

$$\dot{W}_{\mathrm{M}} = \mathrm{m}_{\mathrm{s}} c_{\mathrm{s}} f \left(\frac{\overline{\Delta T}}{T} \right) \left[\frac{R-1}{R} \overline{\Delta T}_{\mathrm{ad}} + \frac{\Phi}{R} (T_{\mathrm{H}} - T_{\mathrm{C}}) \right] \tag{4.4}$$

4.2.2 Property implementation

In the semi-analytic AMR expressions, the solid phase specific heat and the adiabatic temperature change are determined using material properties for discrete low and high magnetic field strengths ($\bar{B}_H, \bar{B}_L$) defined by the average magnetic field over each blow period. Demagnetization effects produce a lower internal field, B_{int}, relative to the applied field:

$$B_{\mathrm{int}}(x) = \bar{B}_{\mathrm{app}} - \mu_0 \rho_{\mathrm{s}} N_{\mathrm{D}} \sigma(T(x), \bar{B}_{\mathrm{app}}) \tag{4.5}$$

where μ_0 is the permeability of free space, ρ_{s} is the refrigerant density, N_{D} is the average demagnetization factor and σ is the specific magnetization of the refrigerant. The demagnetization expression for a bed of packed spherical particles ($N_{\mathrm{D,geo}}$=1/3) with a cylindrical regenerator geometry subjected to a transverse field is [118, 119]:

$$N_{\mathrm{D}} = 1/3 + (1-\epsilon)(N_{\mathrm{D,csg}} - 1/3) \tag{4.6}$$

where ϵ is the regenerator porosity.

In this work, magnetocaloric material properties such as specific heat, specific magnetization and adiabatic temperature change are determined via mean field theory (MFT) [118, 120]. Gadolinium-yttrium alloys are modeled as fictitious second-order materials with Gd properties shifted to the respective Curie temperature. This was shown to be a reasonable assumption in Refs. [95, 1].

Fig. 4.2 illustrates the determination of material properties for an individual layer. Boundary temperatures are specified and the assumed linear temperature distribution shown in the upper left window (a), is used to determine the average internal fields of the layer, shown in the upper right window (b). The magnetocaloric properties are then evaluated between the average internal fields, where the lower left window in Fig. 4.2 (c) shows the spatially varying reduced MCE ($\Delta T_{ad}/T$). The adiabatic temperature change is approximated using:

$$\Delta T_{ad}(T, \overline{B}_{L,int} \rightarrow \overline{B}_{H,int}) = \Delta T_{ad}(T, 0 \rightarrow \overline{B}_{H,int}) - \Delta T_{ad}(T, 0 \rightarrow \overline{B}_{L,int}) \tag{4.7}$$

The reduced adiabatic temperature change, ζ, is defined as the minimum value over a layer, as indicated by the point in Fig. 4.2 (c).

$$\zeta = \min\Big[\frac{\Delta T_{ad}}{T}\Big]_{layer} \tag{4.8}$$

The specific heat evaluated at the low and high internal field strengths is shown in the bottom right window of Fig. 4.2 (d). In the derivation of the semi-analytic equations, it is assumed that $\Delta T/T = \Delta s/c_{\mathrm{s,H}}$. As such, c_{s} is evaluated as the average high field specific heat over a layer (red dashed line in Fig. 4.2 (d))

$$c_s = \mathrm{mean}\big[c_s(T, \overline{B}_{H,int})\big]_{layer} \tag{4.9}$$

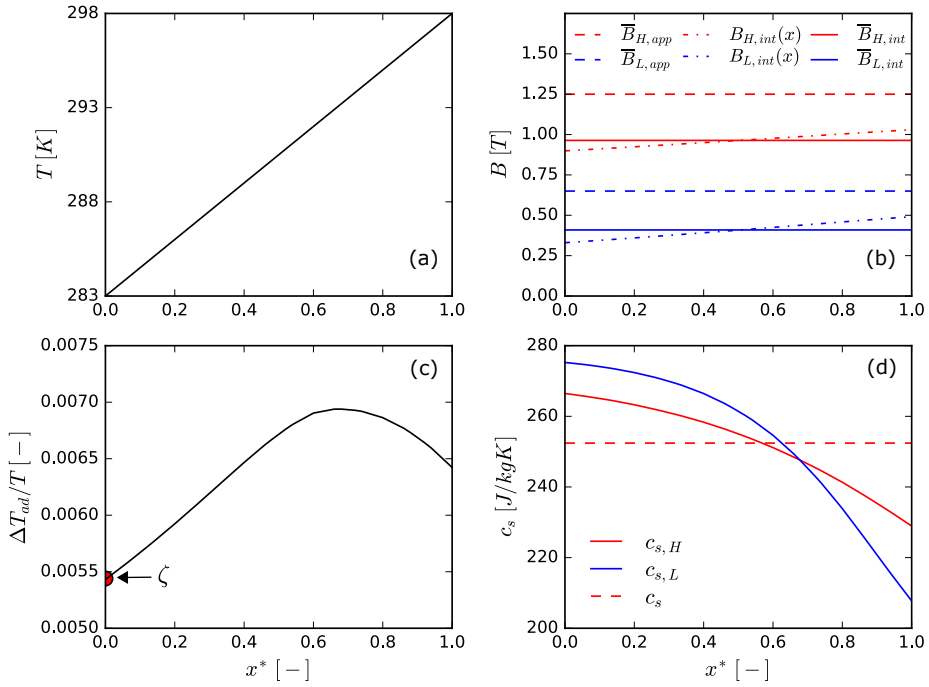

Figure 4.2: Evaluation of semi-analytic properties as a function of the non-dimensional regenerator length (x^*): (a) assumed linear temperature profile; (b) applied and internal (high and low) magnetic fields; (c) reduced MCE ($\Delta T_{\mathrm{ad}}/T$); (d) specific heat capacity as a function of high and low internal field.

4.2.3 Multilayer AMR element model

The multilayer AMR element model is proposed by dividing a single regenerator into a number of AMR elements, where each element can assume the properties of a different magnetocaloric material [121]. The approach is conceptually analogous to 1-D finite-element methods in solid mechanics, where the partial differential equations describing a loaded member are replaced by a network of discretized elements. Rather than finding the nodal displacements satisfying a force balance, the nodal temperatures are solved satisfying an energy balance using the semi-analytic AMR expressions. The schematic of a two-layer AMR element model is shown in Fig. 4.3.

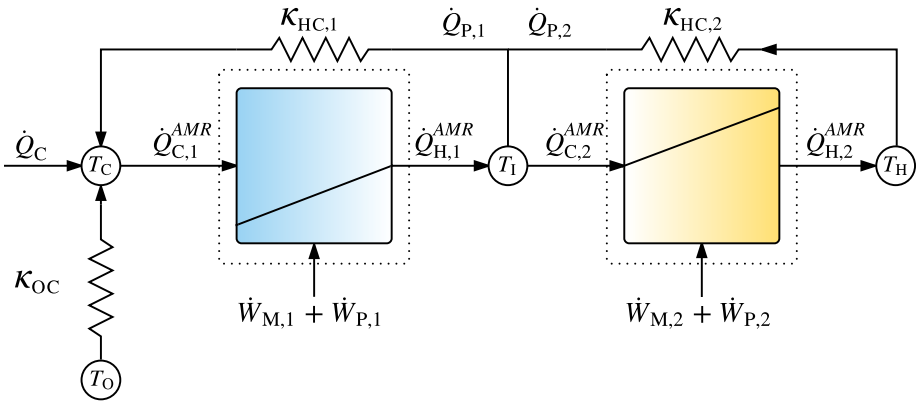

Figure 4.3: Two layer AMR element model. Dotted lines show control volume for layer energy balance.

The heat rejection from each AMR element, $\dot{Q}^{AMR}_{H,i}$, is solved from a layer energy balance:

$$\dot{Q}^{AMR}_{H} = \dot{Q}^{AMR}_{C} + \dot{W}_{M} + \dot{W}_{P} \tag{4.10}$$

Heat leaks external to the regenerator include the effects of imperfect insulation between the cold side and environment, κ_{OC}, and between the hot and cold side of the device, κ_{HC}. κ_{HC} manifests primarily as a heat leak through the permanent magnet structure which thermally interacts along the regenerator length [1]. This effect is captured via an energy exchange at the interface node, yielding the following energy balance:

$$\dot{Q}^{AMR}_{H,1} + \dot{Q}_{P,2} = \dot{Q}^{AMR}_{C,2} + \dot{Q}_{P,1} \tag{4.11}$$

where the signs assume that $T_H > T_I > T_C$.

Assuming the same κ_{HC} for each layer, the interface node energy balance can be expressed as:

$$\dot{Q}_{\mathrm{C},2}^{AMR} - \dot{Q}_{\mathrm{H},1}^{AMR} + \kappa_{\mathrm{HC}}(2T_{\mathrm{I}} - T_{\mathrm{C}} - T_{\mathrm{H}}) = 0 \tag{4.12}$$

where $\dot{Q}_{\mathrm{C},2}^{AMR}$ and $\dot{Q}_{\mathrm{H},1}^{AMR}$ are functions of T_{I}. An iterative root-finding scheme determines the interface temperature satisfying the energy balance in Eq. 4.12.

The net cooling power is obtained from an energy balance at the cold node and multiplied by the number of regenerators in the system as follows. Note that the useful refrigeration effect is reduced by both κ_{HC} and κ_{OC}.

$$\dot{Q}_{\mathrm{C}} = \mathrm{n}_{\mathrm{reg}}\left[\dot{Q}_{\mathrm{C},1}^{AMR} - \kappa_{\mathrm{OC}}(T_{\mathrm{O}} - T_{\mathrm{C}}) - \kappa_{\mathrm{HC}}(T_{\mathrm{I}} - T_{\mathrm{C}})\right] \tag{4.13}$$

4.3 Experimental methods

The multilayer AMR element model is validated using the PM II AMR test apparatus [52] with two-layer performance data [1]. The device contains two cylindrical regenerators housed in the bore of two nested concentric Halbach arrays with a peak field strength of 1.45 T. Validation requires nodal temperature measurements that are obtained with an interface temperature sensor for each composition. In all tests, the hot layer is composed of a fixed gadolinium (Gd) matrix while the cold layer material is varied using Gd and $Gd_{1-x}Y_x$ alloys. ***R1*** is the single material regenerator, e.g. Gd in the cold layer, while ***R2*** to ***R4*** correspond to $Gd_{1-x}Y_x$ alloys. The $Gd_{1-x}Y_x$ Curie temperatures are: $T_{\text{Curie}} = 286$ K for ***R2***; $T_{\text{Curie}} = 283$ K for ***R3***; and $T_{\text{Curie}} = 277$ K for ***R4***.

The magnetocaloric matrix consists of packed spheres with a particle diameter of 300-600 μm (450 μm average) and a porosity of 0.36. The mass of magnetocaloric material ranges from 120 to 130 g per layer (500 to 520 g for the entire device), as the $Gd_{1-x}Y_x$ alloys have a slightly lower density than Gd. Experiments are conducted at a fixed frequency of 0.5 Hz while the rejection temperature (T_H), displaced fluid volume (V_D) and applied load (Q_C) are varied for each regenerator composition as shown in Table 4.1 [1]. The reported measurement uncertainties of the temperature span and cooling power are 1.5 K and 2 %, respectively. Further details on the operating conditions, experimental apparatus and interface temperature measurements can be found in Ref. [1].

Table 4.1: Experimental conditions for each regenerator composition [1].

Displaced Volume [cm^3]	Heat Load [W])	Hot side temperature [K]
6.95	0, 10, 20	288, 293, 298
10.42	0, 10, 20, 30	288, 293, 298
13.9	0, 20, 40	288, 293, 298

4.4 Results

Fig. 4.4 shows temperature span versus cooling capacity curves for the Gd single-material regenerator (***R1***). A comparison between the experimental (symbols) and two-layer AMR element model (solid line) is presented. Red squares indicate the hot layer, blue triangles indicate the cold layer and black circles indicate the total temperature span. Each window corresponds to a combination of rejection temperature and displaced fluid volume.

Fig. 4.5 shows temperature span versus cooling capacity curves for different regenerator compositions (***R2*** to ***R4***). In this figure, operating frequency (0.5 Hz) and displaced fluid volume (13.9 cm^3) are fixed. Each window corresponds to a combination of Curie temperature spacing and rejection temperature. The symbols and lines follow the same description as Fig. 4.4.

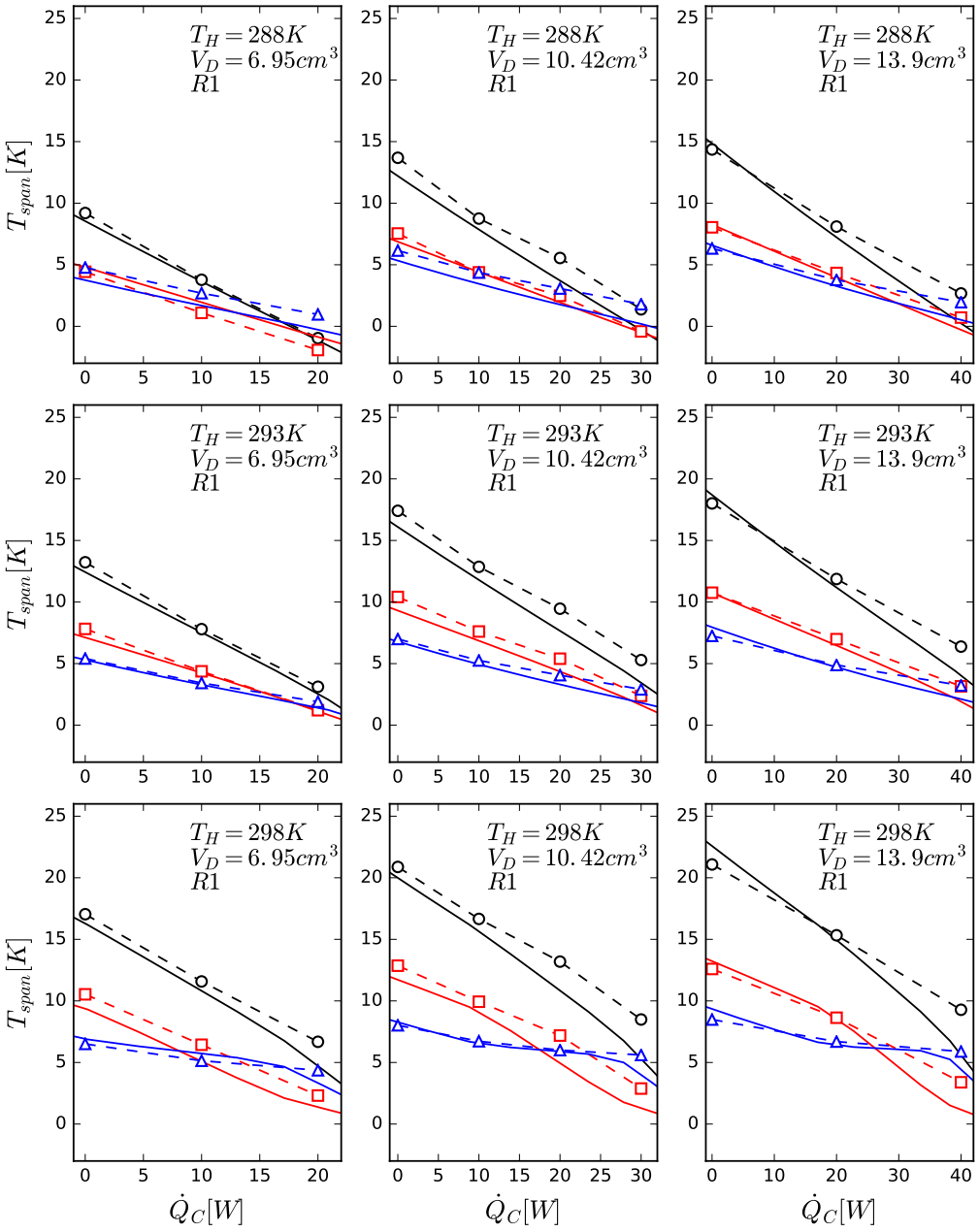

Figure 4.4: Experimental and two-layer AMR element model results for Gd single-layer regenerator (***R1***). The results are presented as the temperature span versus cooling capacity at a fixed frequency of 0.5 Hz with increasing rejection temperature (top to bottom) and displaced fluid volume (left to right).

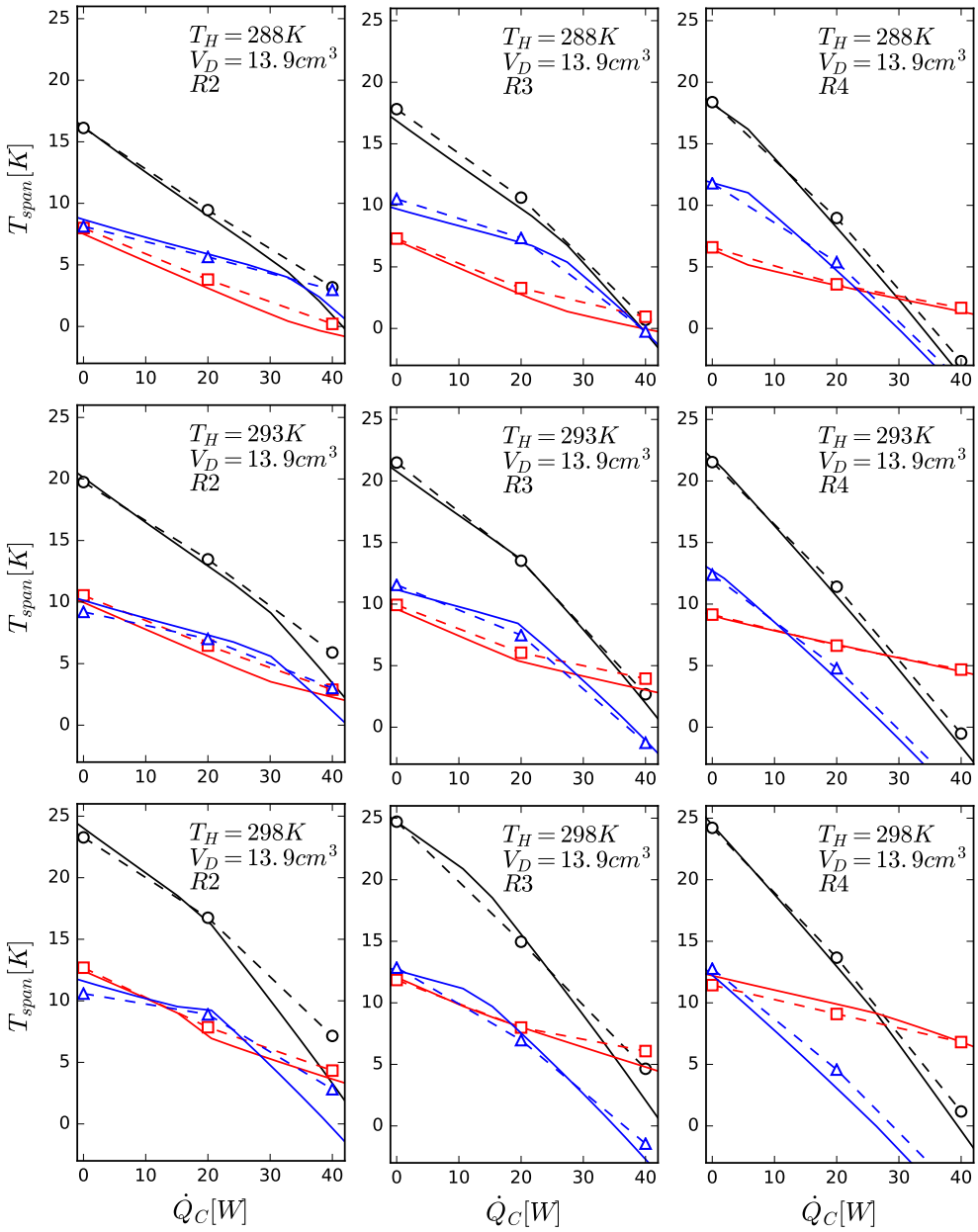

Figure 4.5: Experimental and two-layer AMR element model results for Gd-GdY two-layer regenerators (***R2*** to ***R4***). The results are presented as the temperature span versus cooling capacity at a fixed frequency (0.5 Hz) and displaced volume (13.9 cm^3) with increasing rejection temperature (top to bottom) and Curie temperature spacing (left to right).

4.5 Discussion

Fig. 4.4 and Fig. 4.5 demonstrate the capabilities of the two-layer semi-analytic AMR element model regarding the contribution of each layer to the total temperature span for a range of cooling capacities, operating conditions (displaced volume and rejection temperature) and regenerator compositions. Furthermore, the two-layer AMR element model converges in milliseconds on a desktop computer. The rapid solution time and good predictive capabilities make the model a robust tool for screening operating conditions and regenerator compositions.

A parametric study of the parasitic heat leak reveals that increased spans on the order of 5-10 K are possible with a 50% decrease in κ_{OC}. κ_{OC} in the PM II device is experimentally reduced by removing the cold-side heat exchanger and redesigning the magnet support structure using a thermally insulative material. κ_{HC} is reduced using a regenerator housing with a smaller diameter (22.4 mm to 21.4 mm) minimizing the transverse heat leak from the permanent magnet structure [83, 112]. As a penalty, however, the matrix mass is reduced from Ref. [1] by 25 grams per regenerator resulting in a total device mass of 0.45 kg.

Fig. 4.6 shows the experimental (symbols) and simulated (solid lines) temperature distribution before (from Ref. [1]) and after the experimental modifications. ***R4*** is used with a frequency of 0.5 Hz, a rejection temperature of 298 K and a displaced volume of 13.9 cm^3. While the original heat leak conductances are based on experiments [83], the modified values in Table 4.2 are obtained by fitting simulations to nodal temperature measurements. Following the initial simulations, the temperature span with zero applied load is improved by 7.2 K when the parasitic heat leak is reduced as specified in Table 4.2.

Table 4.2: Modified AMR parameters, where m_{reg} is the mass of a single regenerator and κ_{HC} is the heat leak for each layer.

	$\mathrm{m_{reg}}$ [kg]	κ_{OC} [W/K]	κ_{HC} [W/K]
Original	0.25	0.5	0.4
Modified	0.225	0.25	0.3

With the modified device validated, the system is further optimized to maximize the temperature span with zero applied load and a constraint on the total pressure drop. The optimization problem is formulated as:

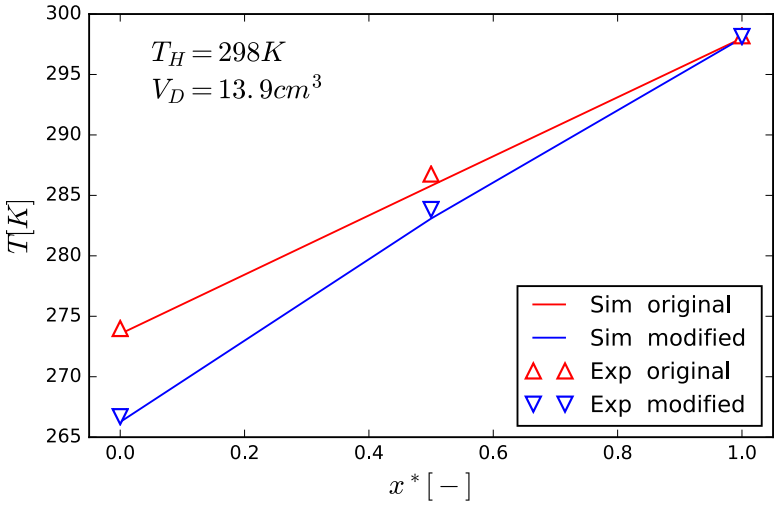

Figure 4.6: Averaged temperature profile along the dimensionless length for ***R4*** before and after the device modifications. The symbols indicates experimental measurements while the solid line represents simulations with the two-layer AMR element model using the heat leaks conductances given in Table 4.2.

$$\begin{aligned} &\text{Maximize } T_{span}(T_{\mathrm{H}}, \Delta V_D, f, m_{\mathrm{reg}}, \Delta T_{\mathrm{Curie}})\big|_{\dot{Q}_C=0} \\ &\text{s.t. } \Delta P(T_{span}, T_{\mathrm{H}}, \Delta V_D, f, m_{\mathrm{reg}}, \Delta T_{\mathrm{Curie}}) \leq 7 \text{ Bar} \end{aligned} \tag{4.14}$$

with bounds on the design variable of:

$$\begin{bmatrix} 288 \\ 3.45 \\ 0.25 \\ 0.05 \\ 0 \end{bmatrix} \leq \begin{bmatrix} T_{\mathrm{H}}[K] \\ V_D[cm^3] \\ f[hz] \\ m_{\mathrm{reg}}[kg] \\ \Delta T_{\mathrm{Curie}}[K] \end{bmatrix} \leq \begin{bmatrix} 318 \\ 27.8 \\ 1.5 \\ 0.225 \\ 16 \end{bmatrix} \tag{4.15}$$

The bounds on V_{D} , f and m_{reg} are based on limitations of the PM II device, while the Curie temperature spacing governing the cold layer ordering temperature is constrained to the available compositions (***R1*** to ***R4***). With a fixed bed diameter, the matrix length scales with regenerator mass. The pressure drop constraint investigates if shorter beds with high fluid capacity outperform longer matrices with reduced f-V_{D} combinations.

Due to the nonlinearity of the problem, a two-phase hybrid optimization approach is implemented. First, the Python SciPY differential evolution metaheuristic is employed which stochastically breeds favorable configurations [108]. Differential evolution, a subset of the genetic algorithm, is well suited for finding global optimizers

at the expense of computationally intensive convergence. A coarse convergence criterion (20 iterations with a population of 25) returns the most favorable candidate which is used as a starting solution for a gradient-based, constrained sequential least squares quadratic programming method (SLSQP). The hybrid optimization returns repeatable optimizers within minutes.

The optimized design vector is shown in Table 4.3. The frequency and regenerator length should be maximized with the displaced volume satisfying the pressure drop constraint. As the parasitic heat leak is reduced, the Curie temperature spacing should be increased. ***R4*** is the simulated optimizer for the modified experimental device, while the maximum temperature span was previously measured with ***R3*** [1]. Removing the upper bound of 16 K, an optimal composition of $\Delta T_{\text{Curie}} = 18.3$ K is simulated yielding a 0.5 K improvement in total span. As most AMR research facilities have a limited set of magnetocaloric materials available, the differential evolution step of the presented two-phase algorithm can be configured to optimize discrete sets of available materials in contrast to the continuous ΔT_{Curie} investigated here.

Table 4.3: Optimized design variables.

T_{span} [K]	T_{H} [K]	$V_D[cm^3]$	f [Hz]	m_{reg} [kg]	ΔT_{Curie} [K]
37.3	303	7.13	1.5	0.225	16

As discussed above, the objective of the AMR element model is to efficiently screen a large parameter space to find candidate solutions for more sophisticated methods. Thus, as a final step, the optimized parameters in Table 4.3 are used as a starting point for an experimental investigation focused on maximizing the no-load temperature span. Fig. 4.7(a) presents a sweep of T_{H} in the vicinity of the optimal vector summarized in Table 4.3. Open symbols (red squares: hot layer; blue triangles: cold layer; black circles: total temperature span) are experimental measurements of ***R4*** with $f = 1.5$ Hz and $V_{\text{D}} = 6.95$ cm^3, the closest fixed increment to the optimized V_{D} . The solid diamond is the optimal temperature span from the data in Table 4.3.

Fig. 4.7(b) presents a sweep of frequency in the vicinity of the simulated maximizer. Again, open symbols are experimental measurements of ***R4*** with $V_{\text{D}} = 6.95$ cm^3 and $T_{\text{H}} = 306$ K. While the model predicts a maximum T_{span} at $T_{\text{H}} = 303$ K and the upper frequency bound of 1.5 Hz, a maximum T_{span} of 40 K is experimentally measured at 0.9 Hz and $T_{\text{H}} = 306$ K.

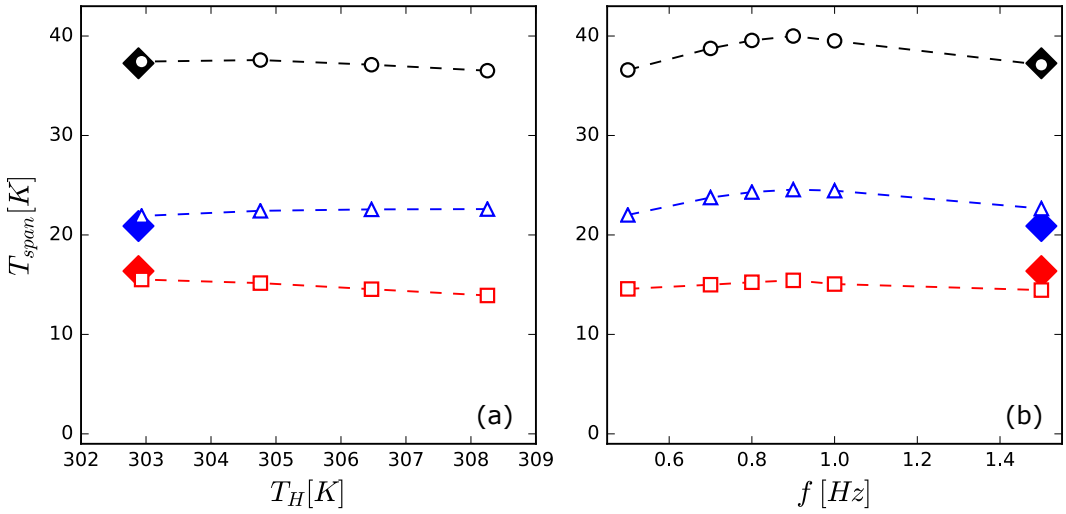

Figure 4.7: Optimized operating point (diamonds) and experimental measurements (dashed lines) as a function of (a) hot side temperature and (b) frequency.

4.6 Conclusions

A numerically efficient model based on a semi-analytic AMR element is developed and used to predict multilayer Active Magnetic Regenerator performance. The two-layer AMR element model demonstrates good predictive capabilities using experimental data from [1] and new experiments reported in the present work. The validation is performed over a broad range of operating parameters and regenerator compositions. An optimization routine is developed and is proven to be a valuable tool for identifying candidate solutions for experimental devices.

A maximum temperature span of 40 K is experimentally measured in close proximity to the simulated optimum. This is one of the largest no-load temperature spans from a permanent magnet based device reported in literature, and is accomplished using a well documented AMR device. Future works will extend the AMR element approach to larger numbers of layers for both second and first-order magnetocaloric materials.

Acknowledgments

The support of the Natural Sciences and Engineering Research Council of Canada and BASF New Business is greatly appreciated.

Chapter 5

Passive force balancing of an Active Magnetic Regenerative Liquefier

Journal of Magnetism and Magnetic Materials 451 (2018), 79-86

Abstract

Active magnetic regenerators (AMR) have the potential for high efficiency cryogen liquefaction. One active magnetic regenerative liquefier (AMRL) configuration consists of dual magnetocaloric regenerators that reciprocate in a persistent-mode superconducting solenoid. Issues with this configuration are the spatial and temporal magnetization gradients that induce large magnetic forces and winding currents. To solve the coupled problem, we present a force minimization approach using passive magnetic material to balance a dual-regenerator AMR. A magnetostatic model is developed and simulated force waveforms are compared with experimental measurements. A genetic algorithm identifies force-minimizing passive structures with virtually ideal balancing characteristics. Implementation details are investigated which affirm the potential of the proposed methodology.

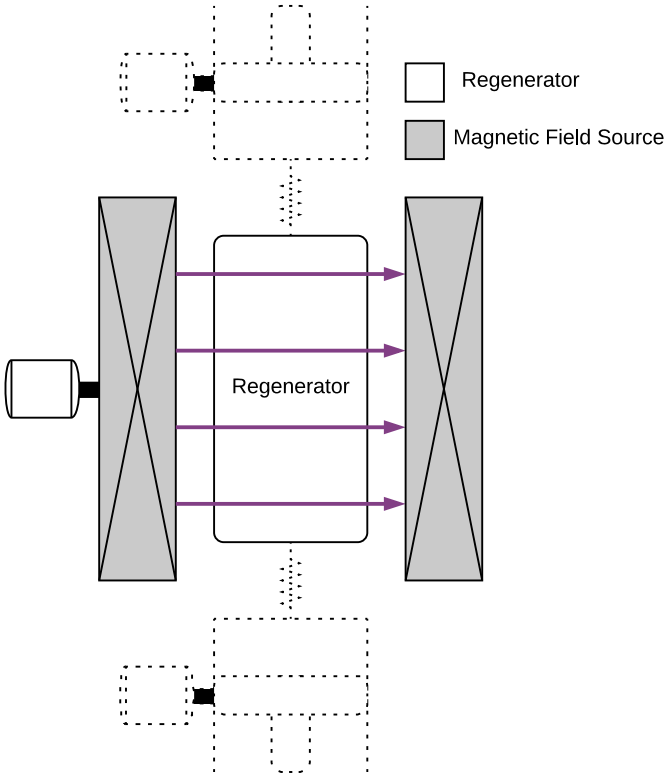

Figure 5.1: Graphical abstract of chapter 5, focusing on the force interactions between the magnetic field source and regenerator.

Nomenclature

Roman

A	area [m^2]
B	magnetic flux density [T]
F	force [N]
H	magnetic field strength [A m^{-1}]
I	solenoid winding current [A]
j	current density [A m^{-2}]
M	magnetization [A m^{-1}]
$\dot{Q}_{eddy}$	Eddy current generation [W]
r	radius [m]
t	time [s]
$\overleftrightarrow{T}$	Maxwell electromagnetic stress tensor [N m^{-2}]
T	temperature [K]
V	volume [m^3]
z	spatial coordinate along solenoidal axis

Greek

δ_{ij}	Kronecker delta [-]
Γ	geometric factor [-]
μ_0	Permeability of free space [H/m]
ρ	density [kg m^{-3}]
ρ_e	electrical resistivity [Ωm]
σ	specific magnetization [A m^2 kg^{-1}]

Subscripts and Superscripts

C	cold reservoir or cold side
coil	superconducting magnet winding
Curie	magnetic ordering temperature
H	hot reservoir or hot side
m	middle passive structure
magnet	position of AMR relative to magnet
o	outer passive structure

5.1 Introduction

Although hydrogen (H_2) has a gravimetric energy density several times greater than common fossil fuels such as gasoline or diesel, the low volumetric energy density of gaseous hydrogen has motivated research efforts on liquid hydrogen ([122]) and liquefaction technologies [123]. The low process efficiency of state-of-the-art liquefiers coupled with the added expense of long-distance transport in cryogenic tankers significantly raise the cost of liquid hydrogen at distributed refueling stations.

The active magnetic regenerator (AMR) uses a magnetocaloric material (MCM) as the matrix media in a thermal regenerator [16], and shows promise for high efficiency distributed cryogen liquefaction [124]. In an AMR, each differential regenerator section undergoes an independent Brayton refrigeration cycle consisting of: (1) adiabatic magnetization, (2) isofield heat rejection, (3) adiabatic demagnetization and (4) isofield heat absorption. In operation, warm fluid is pumped to the hot end at T_{H} where heat is released and cold fluid is pumped to the cold end at T_{C} where heat is absorbed.

Room temperature AMR devices using permanent magnets have demonstrated commercially relevant cooling powers [23], efficiencies [24] and temperature spans [125]; however, costs must be reduced for market penetration [71, 22]. While room temperature AMR devices are an active area of research, active magnetic regenerative liquefiers (AMRL's) are less mature and only a small number of cryogenic devices using superconducting magnets (SC) have been reported. Zimm *et al.*(1996) [126] measured a 35 K temperature span while rejecting heat to liquid nitrogen (LN2). Rowe and Tura (2006) [90] measured a 50 K temperature span from room temperature using a three material regenerator, and the device was later modified for cryogenic testing [127]. The layered experiments were investigated in subsequent analytic and numerical works [115, 116, 26]. Kim *et al.* (2013) [45] presented a no-load cold temperature of 24 K while rejecting heat to LN2 using 83 grams of magnetocaloric material. The AMRL was recently retrofitted with a GdBCO high temperature superconducting solenoid [50]. The device was numerically investigated and an optimized layering composition was proposed [103]. While the temperature spans reported by Kim *et al.* [45] approached the domain of a hydrogen liquefier, larger devices are required to provide commercially relevant capacities.

Barclay *et al.*(2016) [128] and Holladay *et al.* (2017) [46] described a large-scale AMRL with an ultimate goal of hydrogen liquefaction from room temperature. While

a temperature span of 100 K was reported with 2.1 kg of a single magnetocaloric material, the varying permeability in the solenoid core induced an electromotive force across the copper superconducting stabilizer. This ultimately heated the superconducting winding towards the critical temperature, limiting the applied field strength to 3.3 T. The magnet heating was found to increase with regenerator mass, applied field strength and operating frequency.

Improved cooling capacities require increased regenerator mass which, to avoid a magnet quench, decreases the magnetic field strength and consequentially the cooling capacity; a challenge with reciprocating AMRL configurations. The magnetic field from the coupled regenerator-solenoid system must be explored to reduce spatial and temporal magnetization gradients. Barclay *et al.*(1986) [129] simulated force waveforms for reciprocating and rotary configurations. Rowe and Barclay (2002) [130] used the centerline field of a static, air-bored solenoid simulation to evaluate magnetization and magnetic forces. An optimization routine found a flywheel configuration minimizing the cycle RMS torque accounting for magnetic, pumping and inertial loads. While forces were balanced at the drive input, a flywheel does not resolve the magnetization gradients and coupled magnet heating problem.

Peksoy and Rowe (2005) [131] later performed magnetostatic field simulations to investigate the variation of magnetization in a single and two-material AMR. Rowe and Tura (2008) [132] continued this work by investigating ferromagnetic shims to concentrate magnetic field lines in the regenerator, demonstrating that the influence of magnetic material on the magnetic field distribution can be both the detrimental and beneficial. Recently, Mira *et al.* (2017) [133] solved the magnetostatics problem to investigate demagnetization in gadolinium (Gd) regenerators.

Arnold *et al.* (2011) [44] reported experimental measurements of the mechanical, eddy and magnetic work in a reciprocating AMR device. Although large forces were present, it was found that the thermodynamic cycle work was on the order of the experimental uncertainty. This emphasized that while *regenerator* efficiencies can be high, *device* efficiencies may be heavily penalized without force balancing.

While Peksoy and Rowe (2005) [131] and Mira *et al.* (2017) [133] solved the magnetostatics problem, several works have investigated magnetic forces with a simplified treatment of the magnetic field distribution (i.e. $\vec{B} = \mu_0 \vec{H}$). Kamiya *et al.*(2006) [134] analyzed the force waveform of a reciprocating AMR with two gadolinium doped dysprosium aluminum garnet regenerators using a similar methodology as Rowe and Barclay (2002) [130]. The authors reported a 60 % force reduction using magnetic

material between regenerators. Allab *et al.*(2006) [135] simulated the magnetic force on a Gd sample as a function of the local magnetic field strength, and presented force waveforms for a magnetized and demagnetized regenerator. Balli *et al.*(2011) [136] and Gama *et al.*(2016) [137] compared experiments and simulations of the force on magnetic material using a similar formulation.

In the present work, a 2-D, axisymmetric magnetostatic model is developed to study the interaction of a multilayered AMR and superconducting magnetic field generator. Magnetic forces are analyzed and compared with experiments on the AMR device described by Barclay *et al.* (2016) [128] and Holladay *et al.* (2017) [46]. A passive, soft ferromagnetic structure is proposed to balance both spatial and temporal magnetization gradients in an effort to simultaneously address the force balancing and magnet heating problems impeding AMRL development. An optimization is formulated to find passive geometries minimizing the force waveform of a dual regenerator assembly. The optimized force waveform is discussed and implementation details such as solution sensitivity and field distribution are investigated.

5.2 Methodology

5.2.1 AMR configuration

Passive force balancing is investigated on the AMR configuration shown in Fig. 5.2 [128, 46]. A persistent-mode, conduction-cooled NbTi Cryomagnetics 70-650-010CF superconducting solenoid is used to generate the magnetic field for two regenerators mounted axially opposite to each other onto a common cold heat exchanger (CHEX). The solenoid consists of two composite windings with the properties listed in Table 5.1.

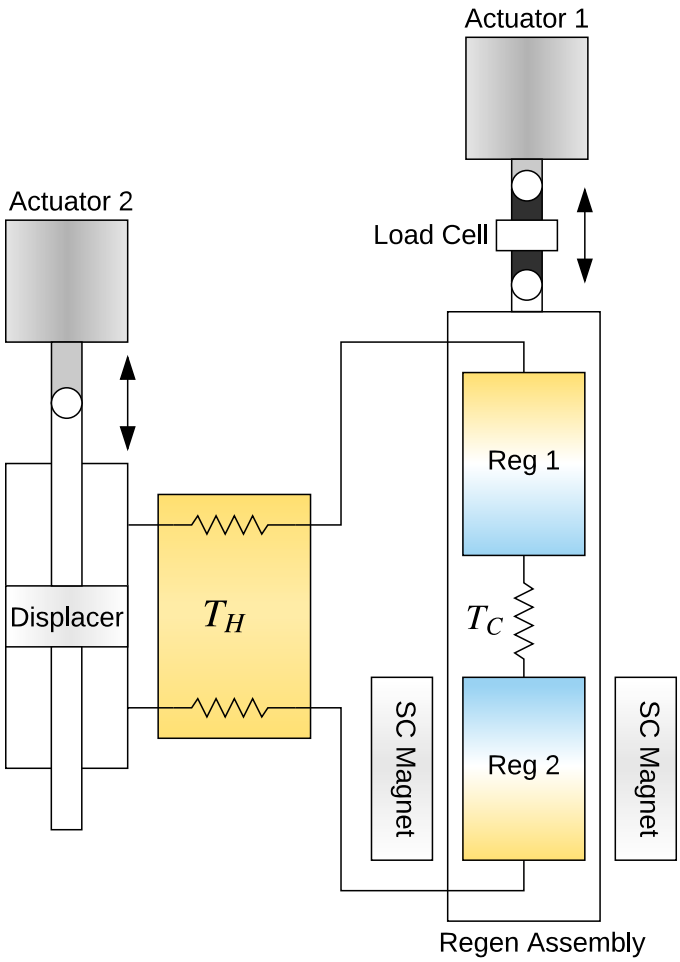

Figure 5.2: Schematic of experimental AMR device. Actuator 1 drives regenerator assembly inside stationary superconducting (SC) magnet while load cell measures net force. Actuator 2 displaces pressurized helium through a temperature controlled circulator at T_{H}.

Table 5.1: Superconducting magnet dimensions.

Winding	Inner diameter [mm]	Outer diameter [mm]	Length [mm]	Turns [-]
1	172.7	180.6	203.2	1708
2	180.6	232.9	203.2	17791

Each regenerator contains eight layers of magnetocaloric material which are summarized in Table 5.2 and shown in Fig. 5.4. The layers consist of rare-earth gadolinium and gadolinium alloys with yttrium, terbium, erbium, dysprosium and holmium with compositions selected for a respective Curie temperature spacing of 20 K per layer. Spherical particles of each refrigerant are prepared by AMES using a rotating disk apparatus [46] and packed into monolithic regenerators with an approximate porosity of 0.36 and mean particle size of 225 μm.

Table 5.2: Rare-earth alloys synthesized by AMES laboratory for eight-layer regenerator.

Layer	Composition	T_{Curie}[K]	Mass [g]	Diameter [mm]	Length [mm]
L1	$Gd_{0.16}Ho_{0.84}$	153	57	31.8	14.2
L2	$Gd_{0.27}Ho_{0.73}$	173	100	38.1	17.3
L3	$Gd_{0.15}Dy_{0.85}$	193	139	44.5	17.7
L4	$Gd_{0.32}Dy_{0.68}$	213	172	50.8	16.8
L5	$Gd_{0.67}Er_{0.33}$	232	202	57.1	15.6
L6	$Gd_{0.3}Tb_{0.7}$	253	235	63.5	14.7
L7	$Gd_{0.91}Y_{0.09}$	274	258	69.9	13.3
L8	Gd	293	268	76.2	11.6

A linear actuator drives the regenerator assembly with constant velocity, as shown in Fig. 5.2, and a second actuator drives a double-acting piston displacing 2,520 cm^3 of pressurized Helium. The two actuators are driven out of phase with equal displacement times of 2 seconds, yielding a trapezoidal waveform with a cycle frequency of 0.125 Hz. A Futek LCM350 load cell measures the net assembly force with a calculated uncertainty of 160 N. In practice, however, the sensor is able to measure the static assembly weight within 10 N. The measured force waveforms are corrected for the assembly weight of 0.33 kN. E-type thermocouples measure the temperature across each layer with an approximate uncertainty of 0.5 K. Measurements are recorded with a National Instruments CompactDAQ.

5.2.2 Magnetostatics model

The superconducting winding is modeled in COMSOL Multiphysics using the AC/DC magnetic fields interface in a 2-D axisymmetric domain. As the AMRL cycle period generally exceeds 1 second, Maxwell's equations reduce to:

$$\nabla \times \vec{H} = \vec{j} \tag{5.1}$$

$$\nabla \cdot \vec{B} = 0 \tag{5.2}$$

where $\vec{B}$ is the magnetic flux density in T, $\vec{H}$ is the magnetic field strength in A/m and $\vec{j}$ is the current density in the winding cross section in A/m^2. These are solved numerically with the constitutive relation $\vec{B} = \mu_0(\vec{H}+\vec{M})$, where M is the magnetization in A/m. Boundary conditions are imposed to satisfy magnetic flux conservation ($\vec{n} \cdot \vec{B} = 0$).

The simulations described here consider gadolinium-like materials with molecular mean field theory (MFT) [118, 120] generated magnetization data shifted to the respective Curie temperature. The specific magnetization, defined as the ratio of magnetization (M) to density (ρ), is shown as a function of temperature and field (μ_0H) in Fig. 5.3. The magnetization is then corrected for porosity and processed into relative permeability curves. Fixed heat rejection and absorption temperatures of T_{H} = 280 K and T_{C} = 120 K are considered, relevant for the first stage of a hydrogen liquefier or natural gas liquefaction. As passive force balancing cannot reduce the thermodynamic cycle work stemming from regenerative temperature perturbations, a linear, field-independent axial temperature profile is assumed in each regenerator.

Magnetic forces are evaluated in COMSOL Multiphysics by numerically integrating the Maxwell electromagnetic stress tensor:

$$\vec{F} = \oint_S \overleftrightarrow{T} \cdot \vec{n}\, \mathrm{d}s \tag{5.3}$$

where S is a surface in free space enclosing the considered body and $\vec{n}$ is a unit vector normal to the integration surface. The Maxwell stress tensor, $\overleftrightarrow{T}$, is defined for any coordinate system as:

$$\overleftrightarrow{T}_{ij} = \frac{B_i B_j}{\mu_0} - \delta_{ij} \frac{||\vec{B}||_2^2}{2\mu_0} \tag{5.4}$$

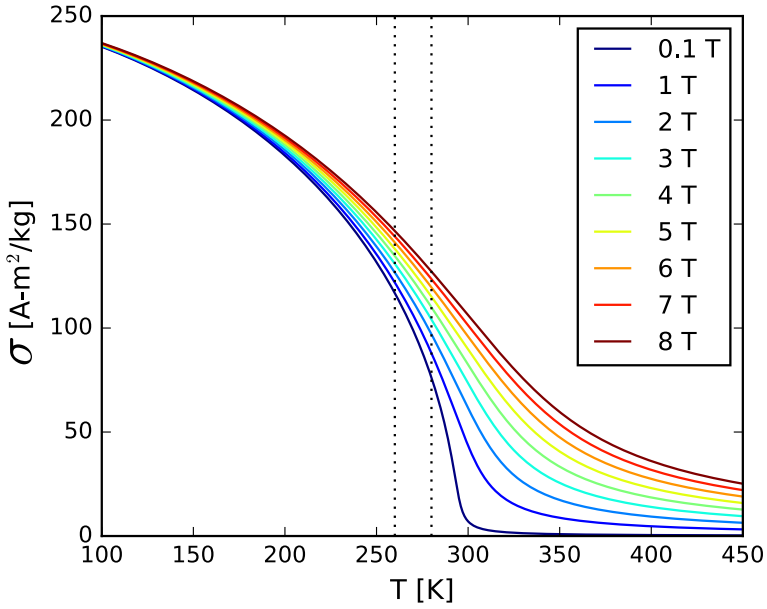

Figure 5.3: Specific magnetization of gadolinium (σ), generated with MFT, illustrating a second-order, para-ferromagnetic phase change at T_{Curie}=293 K. Magnetization increases with field and decreases with temperature. σ is shown for fields (μ_0H) ranging from 0.1 to 8 T. Vertical dashed lines indicate layer operating range.

where δ_{ij} is the Kronecker delta and $||\vec{B}||_2^2$ is the squared norm of the magnetic flux density. Bjørk *et al.* (2010) [32] and Meessen *et al.* (2013) [138] used this formulation to evaluate forces in permanent magnet assemblies using analytic field expressions derived from Fourier series solutions of the governing partial differential equations.

If the flux density and magnetization are uniform over a material volume, and the applied field and magnetization vectors reduce to components along the solenoidal axis (z), the force can be described as:

$$F_z = \mu_0 M_z \frac{\partial H_z}{\partial z} \tag{5.5}$$

which is referred to the Kelvin force [139, 118]. Although the more-robust Maxwell stress tensor formulation is used in the present work, the Kelvin force familiarizes the physical mechanisms describing magnetic forces in magnetized bodies. Eq. 5.5 describes a force increase with field gradient and magnetization, which occur with increased coil current and decreased magnetocaloric material temperature, respectively.

5.2.3 Optimization formulation

Passive, soft ferromagnetic structures are proposed in the regenerator assembly to minimize variations in magnetization. These passive structures fill the void regions on either side of the regenerators in Fig. 5.2, and an optimization routine determines the structure geometry ($r_{m1}, r_{m2}, r_{o1}, r_{o2}$) that balances magnetic forces. Fig. 5.4 shows the parameterized outer radii, and only the top half of the assembly is shown. The middle passive structure ($r_{\mathrm{m1}}, r_{\mathrm{m2}}$) has a fixed length of 127 mm with a 10 mm gap on either side for the layer 1 (L1) housing and flow distributor. The outer structure ($r_{\mathrm{o1}}, r_{\mathrm{o2}}$) has a fixed length of 85 mm, constrained by the superconducting magnet's bore, and is spaced 10 mm from layer 8 (L8). A fixed inner radius of 10 mm is considered in both structures. The passive structure is composed of 1010 steel with experimental B-H data provided by COMSOL Multiphysics.

The force waveform, $\mathrm{F}(\mathrm{z}_{magnet})$, is composed of static force simulations as the regenerator assembly translates downwards with increasing values of z_{magnet}. An optimization problem is formulated to find the structure geometry defined by ($r_{\mathrm{m1}}, r_{\mathrm{m2}}$,$r_{\mathrm{o1}}, r_{\mathrm{o2}}$) that minimizes the l^2 norm of the force waveform:

$$\mathrm{Min}||F(\mathrm{z}_{magnet}, r_{m1}, r_{m2}, r_{o1}, r_{o2})|| = \sqrt{\sum_{\mathrm{z}_{magnet}=0}^{z_{max}} F(\mathrm{z}_{magnet}, r_{m1}, r_{m2}, r_{o1}, r_{o2})^2} \quad (5.6)$$

Due to the problems' non-convexity, the optimization is performed in MATLAB using a genetic algorithm. An initial population of 25 randomly generated configurations are evaluated, and the 4 design candidates with the highest fitness (lowest l^2 norm) are cloned into the next generation. Remaining design candidates are procreated with a crossover fraction of 0.9 in a process mimicking biological evolution, amalgamating the design traits of two favorable parents. The probability of a design procreating into the next generation increases with fitness, and designs with high forces are eliminated. Further implementation details are outlined in the MATLAB documentation. With appropriate bounds on the design vector, the optimization converges within 12 hours using an AMD FX-8350 CPU.

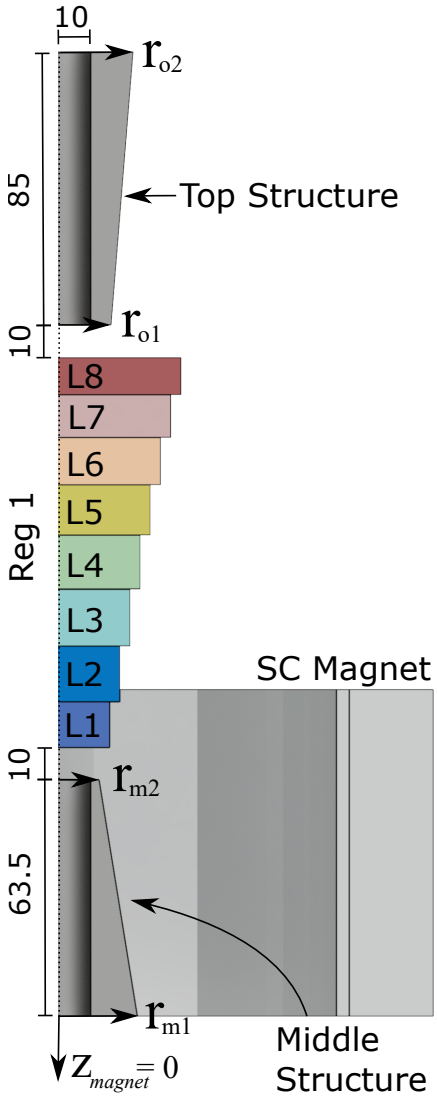

Figure 5.4: AMR configuration (Reg 1 with 8 layers), composite superconducting magnet and parameterized passive structures. Fixed dimensions have units of mm. Figure shows axisymmetric domain, and due to symmetry only the top half of the assembly is shown.

5.3 Results

5.3.1 Validation

Two experiments are performed to validate the force waveform; one with regenerators in the paramagnetic (PM) phase at μ_0H = 3T (I_{coil}=33.4 A) and a second in the ferromagnetic (FM) phase at μ_0H = 4T (I_{coil}=44.2 A). μ_0H refers to the magnetic flux density in the absence of magnetic material. For the ferromagnetic test, the assembly is cooled with saturated nitrogen vapor at atmospheric pressure (LN2 boil-off). Fig. 5.5 shows the average temperatures of each layer over one cycle for the top (red) and bottom (blue) regenerators in the paramagnetic (dashed) and ferromagnetic (solid) phases. The Curie temperature of each layer is shown for reference.

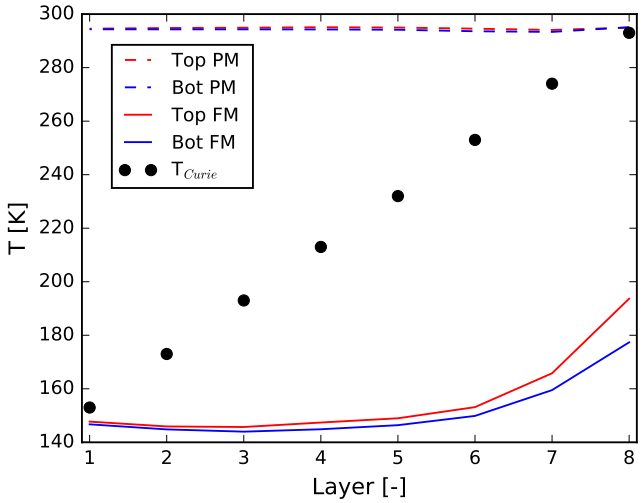

Figure 5.5: Measured temperatures for validation in paramagnetic (PM) and ferromagnetic (FM) phases.

Fig. 5.6 shows the measured and simulated force waveform using the experimentally measured temperatures of each magnetic material as shown in Fig. 5.5. The force waveform for the paramagnetic (PM) and ferromagnetic (FM) phases are shown in Fig. 5.6 (A) and (B), respectively. The solid black line shows the simulated waveform, while the red and blue dashed lines show experimental measurements with the linear actuator moving in the positive ($\rightarrow$) and negative($\leftarrow$) directions. After the regenerator is displaced in either direction, a double-acting piston drives heat transfer fluid through the material matrix as shown in Fig. 5.2. The perturbed solid temperature invokes a magnetization change in each layer of magnetic refrigerant, causing the off-

set between red and blue curves. This manifests as the required thermodynamic cycle work and serves as a limit to what can be attenuated with passive force balancing.

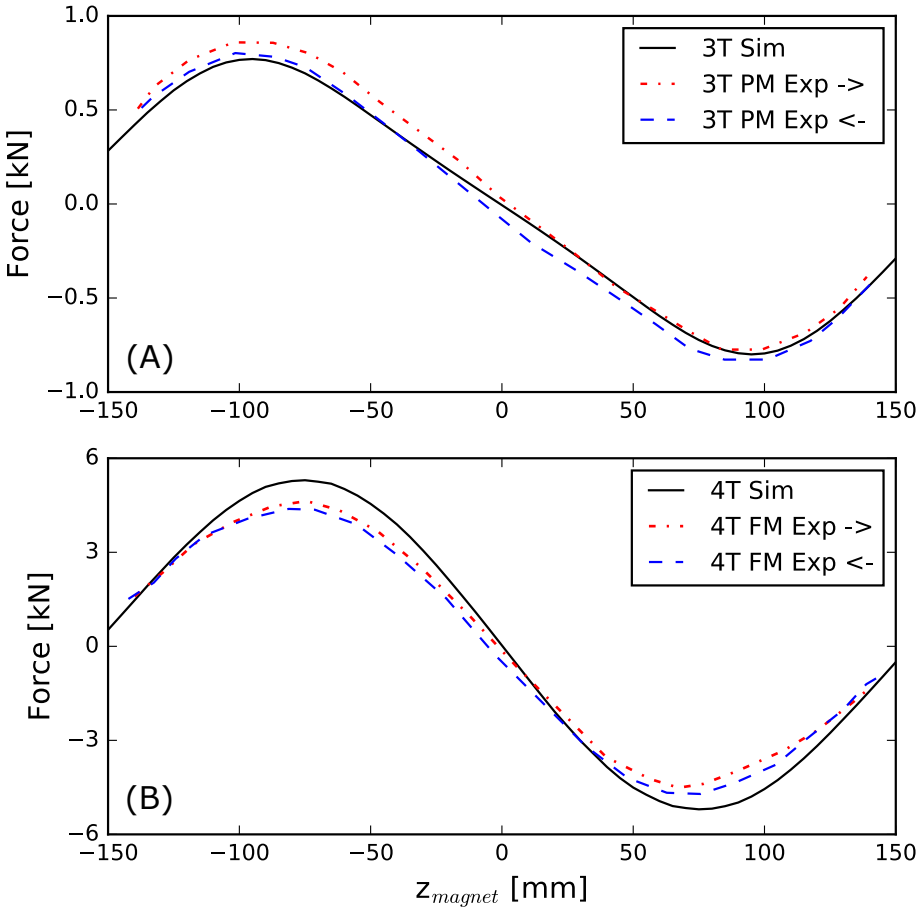

Figure 5.6: Validation of simulated waveforms (solid black) with measurements for paramagnetic (A) and ferromagnetic (B) conditions. Red and blue curves correspond to positive and negative linear actuator velocities, where the difference yields the thermodynamic cycle work.

The model results are in good agreement with the magnitude of the measured force waveforms, and the peak force location is predicted for both experiments. While the simulated paramagnetic forces are nearly identical to measurements, the ferromagnetic simulations are 12.5 % higher than measured. The discrepancy is likely caused by a combination of simulated magnetization data and the magnetic alloy treatment. The MFT data in Fig. 5.3 shows higher ferromagnetic magnetization at low field strengths than experimental measurements [140]. Additionally, shifting gadolinium magnetization data to the ordering temperatures of layers 1-8 causes properties to

be referenced 140 K from the Curie temperature, where the impact of varying alloy parameters (e.g. electron spin and orbital angular momentum) on magnetization is most pronounced [118]. This error is expected to decrease in operation with a linear temperature span from T_{H}= 280 K to T_{C}= 120 K, where materials operate in the vicinity of the magnetic ordering temperature.

5.3.2 Force minimization

The optimization converged on a design vector of $(r_{m1}, r_{m2}, r_{o1}, r_{o2})$ = (25.45, 12.66, 16.41, 23.25) mm, shown in Fig. 5.4, for a winding current of 66.0 A (μ_0H=6 T) and temperature reservoirs of 280 K and 120 K. Fig. 5.7 shows the magnetic force waveform of the top regenerator (solid red), bottom regenerator (solid blue), top passive structure (dashed red), middle passive structure (dashed black) and bottom passive structure (dashed blue). Forces on the middle passive structure are out of phase with forces on the top and bottom regenerators. As such, the middle passive structure is responsible for the majority of force cancellation while outer structures (red and blue dashed lines) fine-tune the net waveform shape. Although the large magnetic forces exerted on individual components requires detailed housing design, the superposition or net assembly force (solid black) is effectively reduced to zero throughout the AMR cycle.

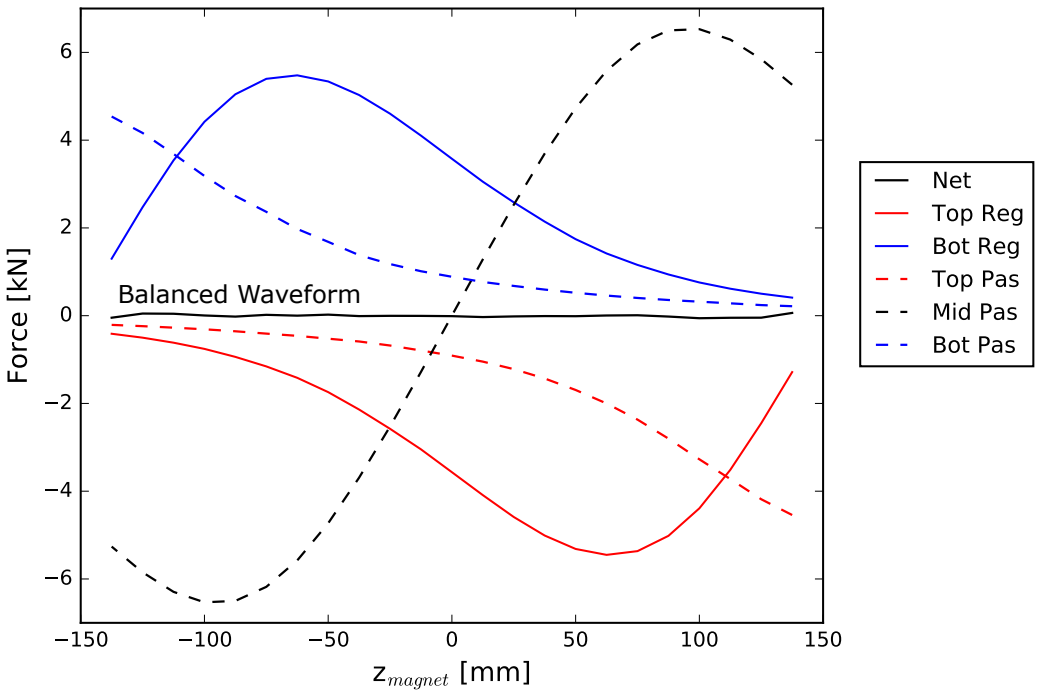

Figure 5.7: Force contribution from each component at μ_0H=6 T in optimized geometry. *Reg* denotes regenerator and *Pas* denotes passive magnetic material. Superposition of forces demonstrates near-ideal cancellation (Balanced Waveform) at this operating condition.

5.4 Discussion

5.4.1 Solution sensitivity

The passive structures are optimized for T_{H}= 280 K, T_{C}= 120 K and μ_0H = 6 T; however, the impact of operating conditions on the force waveform with passive structures must be investigated. Fig. 5.8 shows contours of the maximum net force over the waveform as a function of μ_0H and cold side temperature for the optimized assembly, while Fig. 5.9 shows contours of the maximum net force with two regenerators. The contours illustrate the force variation during the transient cooling process at any field strength.

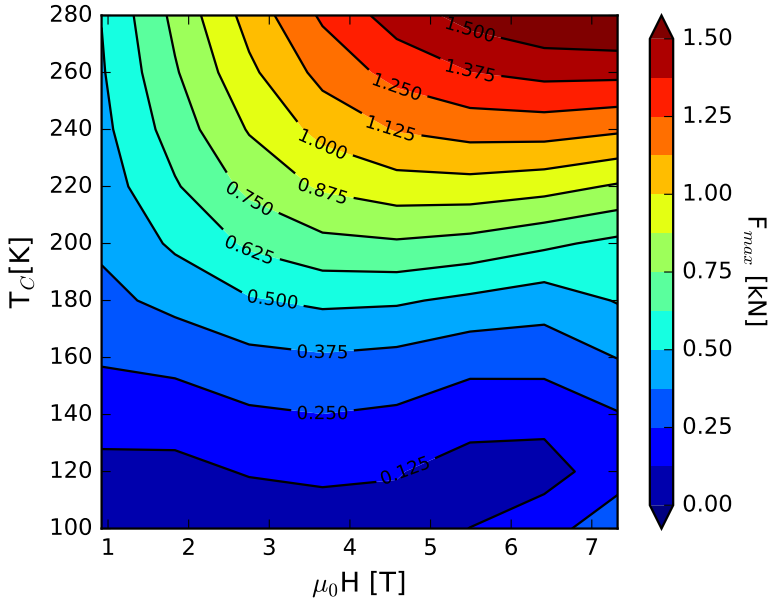

Figure 5.8: Contours of the simulated maximum net force as a function of the cold side temperature and flux density. Passive structures are optimized for T_{C}= 120 K and μ_0H = 6 T. Hot side temperature fixed at 280 K.

Without passive balancing material, the maximum net force increases weakly with decreasing temperature and strongly with increasing field strength as shown in Fig. 5.9. Fig. 5.8 shows the insensitivity of net force to field strength at the design temperature of 120 K; the same passive structure balances forces at an applied field of 3 T (33.2 A) and 6 T (66 A). Furthermore, the peak net force is significantly reduced for nearly all operating conditions with passive balancing material.

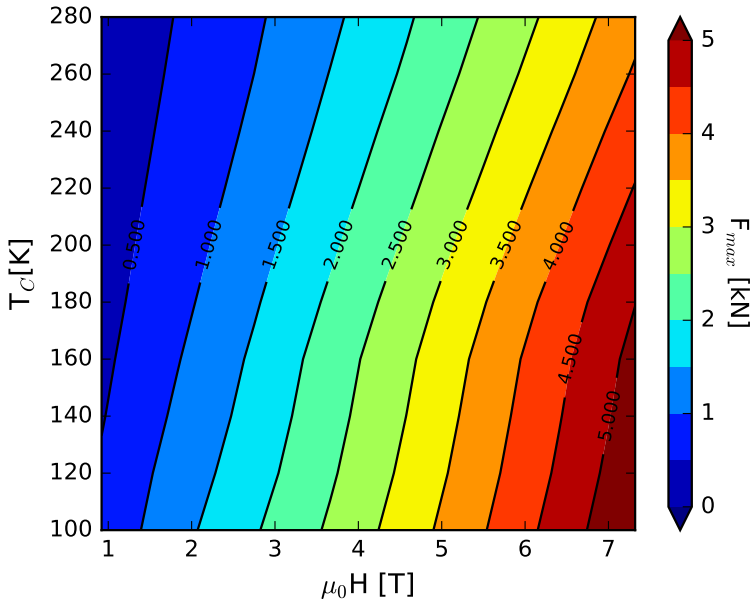

Figure 5.9: Contours of the simulated maximum net force as a function of the cold side temperature and flux density for dual regenerator system (no passive balancing).

5.4.2 Field homogeneity

It is important to minimize the field strength during the demagnetized blow, as the adiabatic temperature change scales with $B^{2/3}$ for gadolinium alloys [12]. Fig. 5.10 shows the centerline field distribution for $\mu_0 H = 6$ T with an air bore (black), with magnetocaloric material (red) and with the optimized assembly (blue). The regenerator locations are indicated by vertical dashed lines.

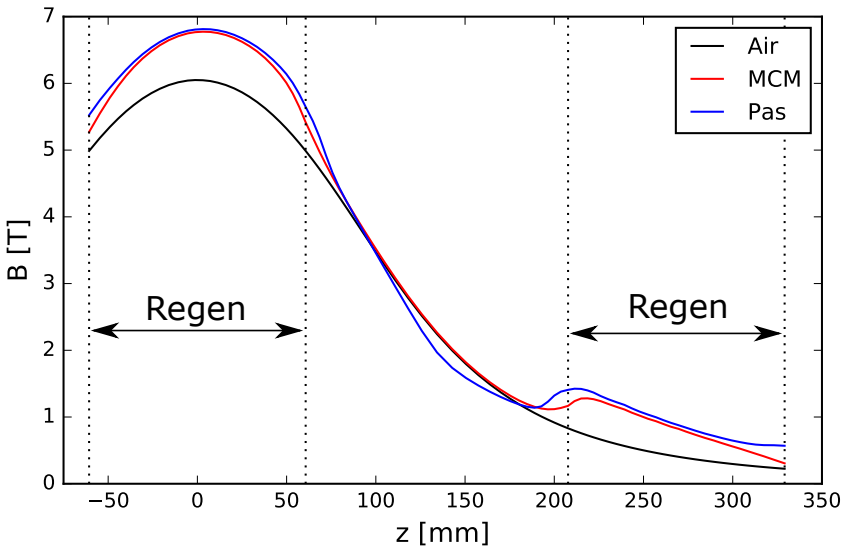

Figure 5.10: Centerline magnetic flux density for air, regenerators (MCM) and the optimized assembly (Pas) showing a minimal increase in low field strength with passive balancing material.

The magnetocaloric material compresses field lines in the solenoid bore, increasing the high field strength. This phenomena was observed and exploited by Rowe and Tura (2008) [132], however Fig. 5.10 demonstrates how the same mechanisms can also be detrimental by increasing the flux density during the low-field fluid blow. Fortunately, the increased low field strength is minimal with the addition of passive balancing material.

5.4.3 Eddy currents

A consequence of the electrically conducting force balancing structure is the generation of eddy currents. The power dissipation from induced currents in an electrically resistive medium act as a parasitic load into the cold side of the AMR. Kittel (1990)

[141] derived analytic expressions for eddy current power dissipation in primitive geometries

$$\dot{Q}_{\mathrm{Eddy}} = \frac{\Gamma A V}{32 \rho_{\mathrm{e}}} (\mathrm{dB/dt})^2 \tag{5.7}$$

where Γ is a geometric form factor, A is the area enclosed by the largest possible current loop, V is the volume of material and ρ_{e} is the electrical resistivity. As AMR performance increases with field strength and operating frequency, $\Gamma AV/\rho_{\mathrm{e}}$ must be minimized. While ΓAV can be reduced with thin laminations of the 1010 alloy considered here, advanced soft magnetic materials with high electrical resistivity deserve further investigation.

5.5 Conclusions

A passive, soft ferromagnetic structure is proposed to balance both spatial and temporal magnetization gradients in an effort to simultaneously address the force balancing and magnet heating problems found in large-scale, reciprocating AMRL devices. A magnetostatic model is developed and validated with experimental force measurements. A genetic algorithm is implemented to identify force-minimizing passive balancing structures with a cold side temperature and field strength of 120 K and μ_0H = 6 T, respectively.

The methodology produces a unique structure which decreases the net assembly force by a factor of 100. The optimized structure is shown to be effective over a wide range of operating conditions and has minimal impact on the effective magnetic field change. Future works will focus on the experimental treatment of magnetization properties, experimental testing of optimized passive structures and the minimization of low field strength.

Acknowledgments

It is a pleasure to acknowledge the financial and programmatic support of the Fuel Cell Technology Office of the Energy Efficiency and Renewable Energy Office of the Department of Energy. The pro-active support of DOE program managers Dr. Erika Gupta (Nee Sutherland) and Dr. Neha Rustagi is deeply appreciated. Additionally, Dr. Andrew Rowe would like to acknowledge the support of the Natural Sciences and Engineering Research Council of Canada.

Chapter 6

Topology optimization of reduced rare-earth permanent magnet arrays with finite coercivity

Journal of Applied Physics 123 (2018) 193903.

Abstract

The supply chain risk of rare-earth permanent magnets has yielded research efforts to improve both materials and magnetic circuits. While a number of magnet optimization techniques exist, topology optimization literature has not incorporated the permanent magnet failure process stemming from finite coercivity. To address this, a mixed-integer topology optimization is formulated to maximize the flux density of a segmented Halbach cylinder while avoiding permanent demagnetization. The numerical framework is used to assess the efficacy of low-cost (rare-earth-free ferrite C9), medium-cost (rare-earth-free MnBi) and higher-cost (Dy-free NdFeB) permanent magnet materials. Novel magnet designs are generated that produce flux densities 70 % greater than the segmented Halbach array, albeit with increased magnet mass. Three optimization formulations are then explored using ferrite C9 that demonstrate the tradeoff between manufacturability and design sophistication, generating flux densities in the range of 0.366-0.483 T.

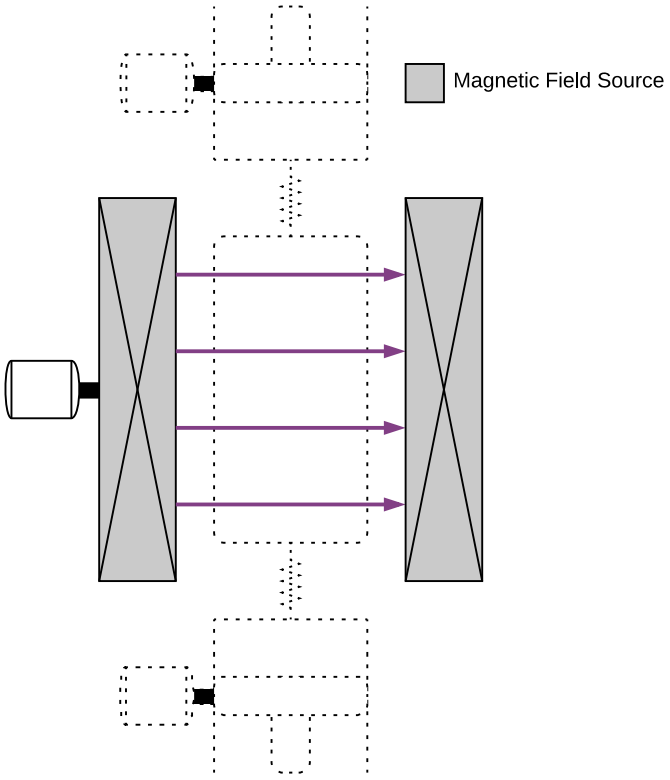

Figure 6.1: Graphical abstract of chapter 6, focusing on the optimization of reduced-rare-earth permanent magnet structures.

Nomenclature

Roman

A	area [m^2]
B	magnetic flux density [T]
B_{rem}	permanent magnet remanence [T]
H	magnetic field strength [A/m]
H_{cj}	polarization coercivity [A/m]
M^*	magnet efficiency [-]
n	number of magnet domains [-]
R	radius [m]
$\vec{x}$	optimization design vector [-]
V_M	magnetic scalar potential [A]

Greek

μ	magnetic permeability [T-m/A]
ρ	local material definition [-]
θ	local remanence orientation [rad]

Subscripts and Superscripts

i	inner (radius)
o	outer (radius)
rem	remanence

6.1 Introduction

The increasing importance of permanent magnets in high-efficiency energy conversion devices has strained strategic material supply chains [142, 143] and raised concerns over state-of-the-art Dy-NdFeB permanent magnets. The US department of energy (DOE) identified dysprosium and neodymium as the most important materials for medium-term clean energy development and noted the supply risk of dysprosium as critical [144]. In addition to exploring new material systems [145, 146, 147, 148, 149] and rare-earth recycling [150], a number of groups are developing rare-earth-free permanent magnet electric machines [151, 152, 153] with a focus on low energy product Ferrite (SrFeO) [154, 155, 156]. The outcomes are mixed; some studies report minimal decreases in efficiency using rare-earth free permanent magnet materials while others report efficiency decreases exceeding 10%. In the latter case, the decreased efficiency is directly correlated with finite coercivity [157].

While new high-energy product and rare-earth-free permanent magnet materials are desired, research and development must also focus on improving magnetic circuits to more efficiently use the materials available today [158]. Of the numerous magnetic circuit designs available [29], Halbach arrays [28, 84, 74, 159] have received significant attention due to their ability to produce a flux density exceeding the permanent magnet remanence. Cylindrical Halbach arrays are used in a number of applications, from electric machines [160] and nuclear magnetic resonance [161, 162, 163] to magnetic refrigeration [73, 164, 75, 22]. The distribution of remanence in a Halbach is defined as [28]:

$$(B_{rem,r}, B_{rem,\theta}) = B_{rem}(\cos(p\theta), \sin(p\theta)) \tag{6.1}$$

where $2p$ is the number of poles, r and θ are the polar coordinate axis and B_{rem} is the magnitude of the remanent flux density. In this work, we focus on the long, dipolar Halbach cylinder ($p = 1$) that produces a field strength of [28]:

$$B = B_{rem}\ln\left(\frac{R_o}{R_i}\right) \tag{6.2}$$

This potential to amplify flux with outer cylinder radius (R_o/R_i) is appealing for lower-remanence permanent magnet materials, however the attainable induction is restricted by finite coercivity [74, 165, 166].

Unlike the continuously varying Halbach array, real permanent magnet structures

are constructed from segments with finite magnetization directions [33, 34] and a number of optimization techniques have been successfully applied. Choi and Yoo (2008) [35] discretized a permanent magnet into finite segments and optimized the distribution of remanence orientations using a sequential linear programming algorithm. The authors later presented differentiable density functions to simultaneously optimize the magnet distribution and local remanence orientation [36]. Isoparametric projection methods have also optimized problems of this nature with success [38, 39]. Bjørk *et al.*(2017) [41] performed a two-material topology optimization (permanent magnet, soft magnetic material) with remanence orientations fixed to that of the theoretical Halbach array to maximize the Λ_{cool} heuristic for magnetic refrigeration applications. Insinga *et al.*(2016) [40] used the reciprocity theorem and the concept of the virtual magnet to optimally design and segment permanent magnet structures for a predefined desired distribution of magnetic flux. While these works have shown promising performance improvements, literature on topology optimization has not considered the permanent magnet failure process stemming from finite coercivity. Instead of an endogenous constraint, it is considered retroactively. Topology optimization that explicitly considers coercivity is needed to identify feasible structures using reduced-rare-earth and rare-earth-free permanent magnet materials.

In the present work, various permanent magnet materials from literature are explored in a segmented cylindrical Halbach array. A mixed-integer topology optimization is then formulated to maximize the flux density of a discretized Halbach cylinder subject to finite coercivity. This computational tool is used to assess the efficacy of low-cost (rare-earth-free ferrite C9), medium-cost (rare-earth-free MnBi) and higher-cost (Dy-free NdFeB) permanent magnet materials. Three scenarios are simulated using ferrite C9 with local remanence orientations: (1) fixed to that of the Halbach cylinder, (2) constrained to the radial and tangential directions, and (3) included as continuous variables in the optimization. The comparison explores the balance between design sophistication and manufacturability in an attempt to exploit recent advances in magnet manufacturing [167, 168].

6.2 Methodology

The magnetic field is numerically evaluated using COMSOL Multiphysics 5.2. The magnetostatics, no current formulation is used in a two-dimensional domain allowing use of the magnetic scalar potential (V_{m}) defined as $\vec{H} = -\nabla V_{\mathrm{M}}$. Substituting the

constitutive relation for permanent magnets ($\vec{B} = \mu\vec{H} + \vec{B}_{\text{rem}}$) into Gauss's law of magnetism ($\nabla \cdot \vec{B} = 0$) yields the PDE governing the magnetic field distribution:

$$\nabla \cdot (\mu \nabla V_{\text{M}} - \vec{B}_{\text{rem}}) = 0 \tag{6.3}$$

where $\mu = \mu_0 \mu_{\text{r}}$, μ_{r} is the relative permeability and $\vec{B}_{\text{rem}}$ is the remanence vector.

When the reverse component of the magnetic field vector, $\vec{H}$, exceeds the polarization coercivity, H_{cj}, a permanent magnet is locally demagnetized. Eq. 6.4 is evaluated throughout the domain and used to determine the required coercivity for the simulated topology [74].

$$H_{\text{cj}} + \vec{H} \cdot \left(\frac{\vec{B}_{\text{rem}}}{||B_{rem}||} \right) \geq 0 \tag{6.4}$$

The optimization is performed in MATLAB using a mixed-integer genetic algorithm, following the implementation of Teyber *et al.* (2017) [22]. Each optimization is performed with a population size of 500, a crossover fraction of 0.4 and is repeated until the objective evaluation fails to improve for three successive runs.

6.3 Results

6.3.1 Material comparison

To establish a benchmark for the topology-optimized designs, rare-earth Dy-NdFeB and SmCo along with rare-earth-free alnico, ferrite and MnBi are simulated in a segmented Halbach array. The magnet grades, remanence, and coercivity are shown in Table 6.1. The coercivity and operating temperature of Dy-NdFeB increase with dysprosium; the N42, N42SH and N42UH grades contain approximately 0, 5 and 8 percent Dy by weight, respectively [143]. With ferrite, the coercivity can be increased by substituting lanthanum and cobalt [169]. The commercial Dy-NdFeB, SmCo, Alnico and C-grade ferrite properties are from Eclipse Magnets, the high-coercivity La-Co free FB9HF ferrite properties are from TDK corporation and the MnBi properties are from Poudyal *et al.* (2016) [170]. Although manganese-aluminum [146, 171, 148, 172] and magnetic steels (e.g. FeC, FeN, FeCoCr) [145, 173] are promising low-cost permanent magnet materials, their properties are currently in the vicinity of C5 Ferrite and Alnico, respectively, and thus not independently investigated here.

The maximum attainable flux density as a function of the outer radius (R_o/R_i) is shown in Fig. 6.2 for a Halbach cylinder with a total of 24 annular segments. The magnetic field ($\bar{B}^{seg}_{max}$) is averaged over the bore and the results are summarized in Table 6.1. The symbols indicate the largest outer radius that can be constructed before insufficient coercivity causes local demagnetization. As suggested by Insinga *et al.*(2015) [165], materials with $\mu_0 H_{cj}/B_{rem} < 1$ (Alnico-5, Alnico-8h, NdFeB-N42, C5 ferrite, C8 ferrite and C10 ferrite) locally demagnetize for all R_o/R_i due to inadequate coercivity. In reality, a Halbach cylinder with these materials will still produce a magnetic flux density in the cylinder bore, however here we disregard any designs with demagnetization.

Table 6.1: Permanent magnet material properties. Maximum attainable magnetic flux density ($\bar{B}^{seg}_{max}$) shown for each material with segmented Halbach cylinder before local demagnetization.

Material	B_{rem} [T]	H_{cj} [kA/m]	$\frac{\mu_0 H_{cj}}{B_{rem}}$	μ_r	$\bar{B}^{seg}_{max}$ [T]
NdFeB-N42	1.28	955	0.937	1.05	ø
Dy-NdFeB-N42SH	1.28	1592	1.563	1.05	1.860
Dy-NdFeB-N42UH	1.28	1989	1.952	1.05	2.367
SmCo-26M	1.02	955	1.176	1.05	1.062
SmCo-26	1.02	1434	1.766	1.05	1.651
SmCo-26H	1.02	1990	2.451	1.05	2.415
Alnico-5	1.25	54	0.054	3.7	ø
Alnico-8H	0.72	152	0.265	2.0	ø
MnBi	0.6	493	1.032	1.2	0.526
ferrite-C5	0.38	199	0.658	1.05	ø
ferrite-C8	0.385	242	0.788	1.05	ø
ferrite-C9	0.38	320	1.058	1.05	0.347
ferrite-C10	0.4	284	0.892	1.05	ø
ferrite-FB9HF	0.405	400	1.241	1.05	0.437

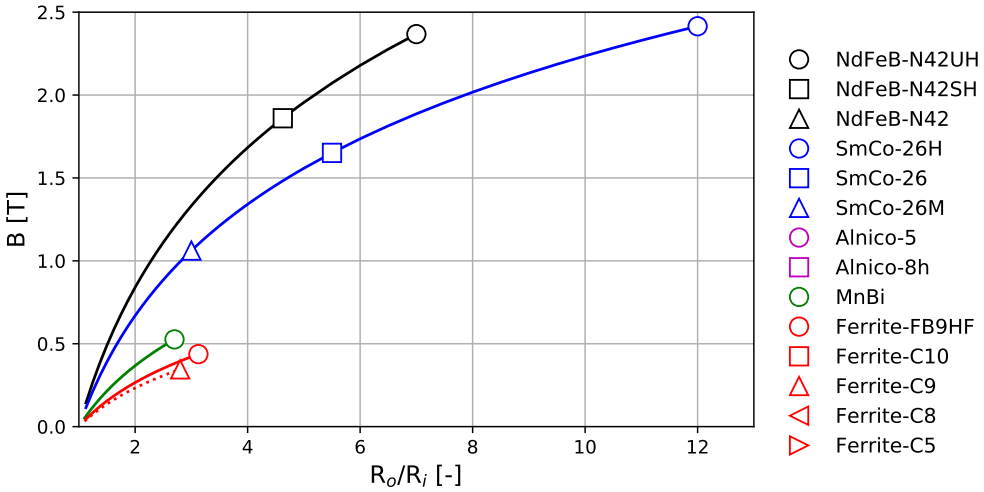

Figure 6.2: Maximum attainable flux density in 24 segment Halbach array before local demagnetization. Each curve corresponds to a fixed remanence strength (e.g. N42-1.28 T), and markers correspond to permanent magnet grades (e.g. N42, N42SH, N42UH). Materials in legend that are absent from figure (NdFeB-N42, Alnico and Ferrite C10, C8 and C5) have local demagnetization for all R_o/R_i; highlighting the importance of coercivity in permanent magnet materials.

6.3.2 Material optimization with fixed remanence orientations

The distribution of permanent magnet material is now optimized with remanence orientations determined by the cylindrical Halbach array, however with each segment assuming a homogeneous magnetization direction (Eq. 6.1 evaluated at the segment center). This is achieved with the following optimization formulation:

$$\begin{aligned} &\text{Maximize } \bar{B}(\vec{x}) \\ &\text{s.t. } H^*_{cj}(\vec{x}) \leq H_{cj} \end{aligned} \tag{6.5}$$

where $\bar{B}(\vec{x})$ is the average bore magnetic flux density, $H^*_{cj}(\vec{x})$ is the required coercivity to avoid permanent demagnetization (Eq. 6.4) and H_{cj} is the permanent magnet coercivity. The design vector, $< x_1, ..., x_i, ..., x_n >$, describes the local material at each of $n = 24$ discretized domains, and in this section, x_i can take integer values of 1 (air) or 2 (permanent magnet).

We investigate rare-earth-free ferrite C9 (B_{rem} = 0.38 T, H_{cj} = 320 kA/m), rare-earth free MnBi (B_{rem} = 0.6 T, H_{cj} = 493 kA/m) and dysprosium-free NdFeB-N42 (B_{rem} = 1.28 T, H_{cj} = 955 kA/m) permanent magnet materials. The optimal magnet designs with ferrite C9 are shown in Fig. 6.3. Average magnetic flux densities of 0.417, 0.486 and 0.562 T are obtained for R_o/R_i = 4, 6 and 8, respectively. These flux densities are a 20.1 %, 40.0 % and 61.9 % improvement over the 0.347 T field produced by the fully segmented Halbach cylinder, as summarized in Table 6.2, albeit with increased magnet mass. While the improvements with R_o/R_i = 8 are obtained by removing material from the outer polar (outer top of domain) and inner equatorial (inner right of domain) positions, nontrivial design features are produced with R_o/R_i = 4 and 6.

The optimal magnet designs with MnBi are shown in Fig. 6.4. Average magnetic flux densities of 0.652, 0.786 and 0.899 T are obtained for R_o/R_i = 4, 6 and 8, respectively; a 23.9 %, 49.4 % and 70.9 % improvement over the 0.526 T induction produced by the fully segmented cylinder (Table 6.1). Although the topologies for R_o/R_i = 6 and 8 are identical, less coercivity is required for R_o/R_i = 6.

The optimal magnet designs with Dy-free NdFeB-N42 are shown in Fig. 6.5. Average magnetic flux densities of 1.127, 1.423 and 1.388 T are obtained for R_o/R_i = 4, 6 and 8, respectively. This affirms the potential of the methodology, as the fully segmented Halbach cylinder demagnetized for all R_o/R_i with this material. Increasing

R_o/R_i from 6 to 8 with NdFeB-N42 yields a *decrease* in magnetic flux density. This is a consequence of the discretization, where the same number of domains ($n = 24$) represent an increased area and, as such, is more susceptible to demagnetization. As with the ferrite C9 and MnBi materials, this improvement is obtained by removing material from the outer polar and inner equatorial positions, however a number of unique design features are present. The NdFeB-N42 topologies have significantly less material in the outer-top region of the magnet design, likely a consequence of $\frac{\mu_0 H_{cj}}{B_{rem}} < 1$ as opposed to $\frac{\mu_0 H_{cj}}{B_{rem}} > 1$ with ferrite C9 and MnBi. Generally speaking, the optimized designs tend to gradually bend lines of magnetic flux by taking the approximate shape of an ellipsoid.

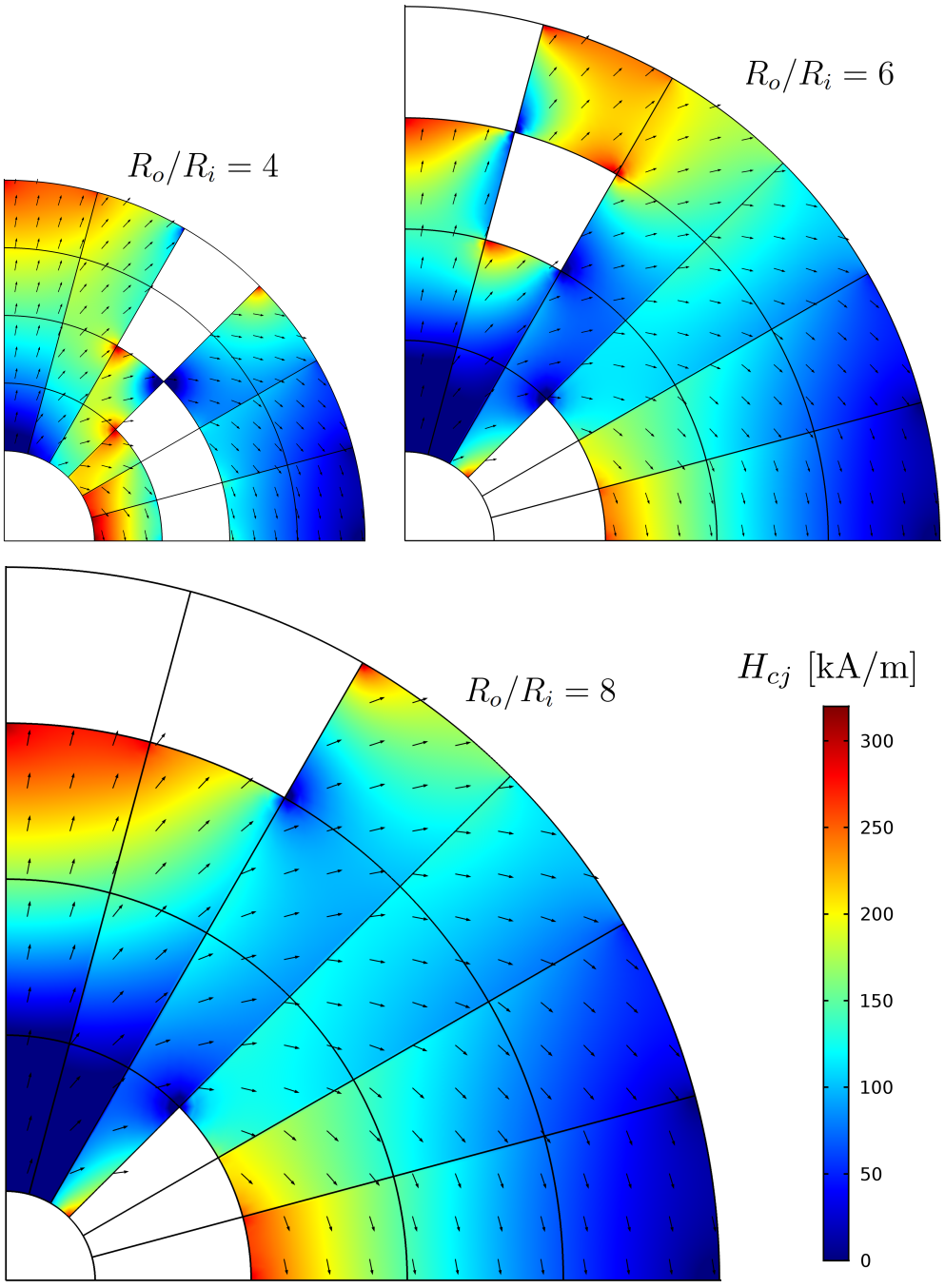

Figure 6.3: Topology optimized Halbach cylinder with ferrite C9 magnet material. Average magnetic flux densities of 0.417, 0.486 and 0.562 are produced for Ro/Ri = 4, 6 and 8, respectively. Color bar shows required coercivity.

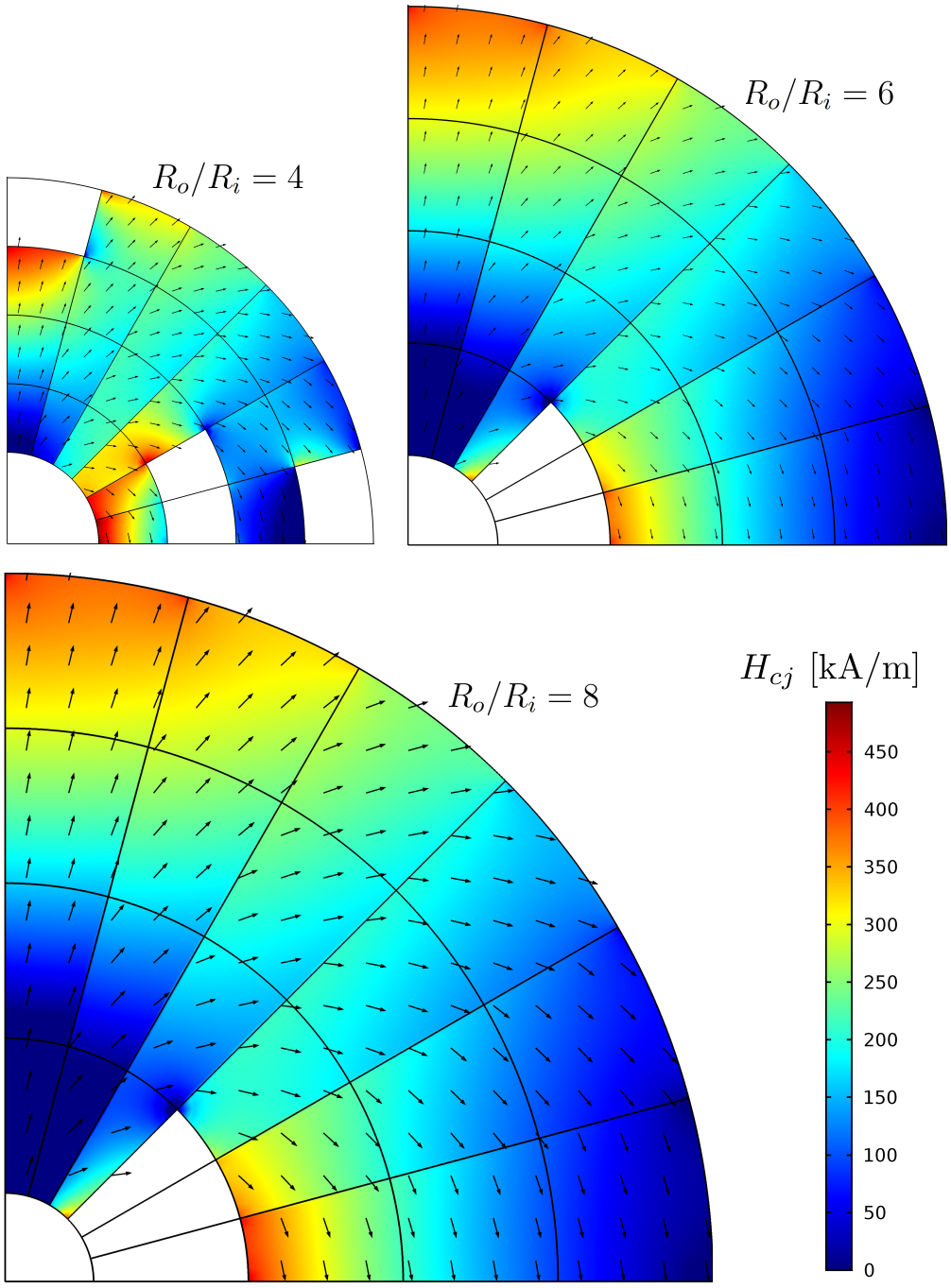

Figure 6.4: Topology optimized Halbach cylinder with MnBi magnet material. Average magnetic flux densities of 0.652, 0.786 and 0.899 are produced for Ro/Ri = 4, 6 and 8, respectively. Color bar shows required coercivity.

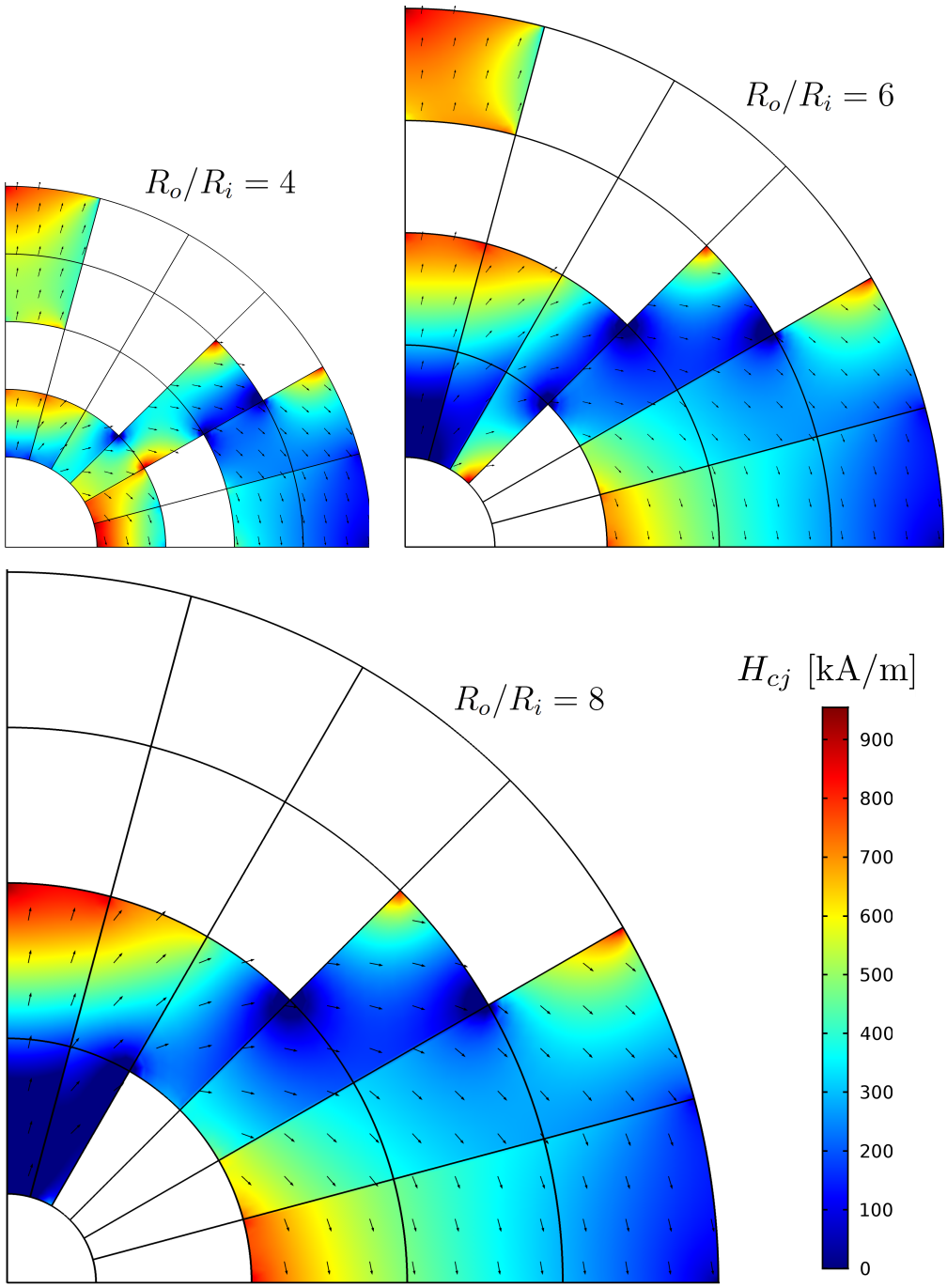

Figure 6.5: Topology optimized Halbach cylinder with Dy-free NdFeB-N42 magnet material. Average magnetic flux densities of 1.127, 1.423 and 1.388 T are produced for Ro/Ri = 4, 6 and 8, respectively. Color bar shows required coercivity.

6.3.3 Material optimization with radial and tangential remanence orientations

We now focus entirely on ferrite C9 with $R_o/R_i = 4$ and constrain the remanence orientations to the radial or tangential directions, as in Lee *et al.* (2017) [38]. This is accomplished with the same formulation above (Eq. 6.5), however, with air, radial and tangential permanent magnets corresponding to $x_i = 1$, 2 and 3, respectively. The optimal distribution of permanent magnet with two magnetization directions is shown in Fig. 6.6. In addition to being a manufacturing-oriented design, the average flux density of 0.366 T presents a 5.5 % improvement over the fully segmented Halbach cylinder as summarized in Table 6.2. Constraining the remanence orientations to the radial and tangential directions does, however, reduce the flux density from the 0.417 T produced in Fig. 6.3.

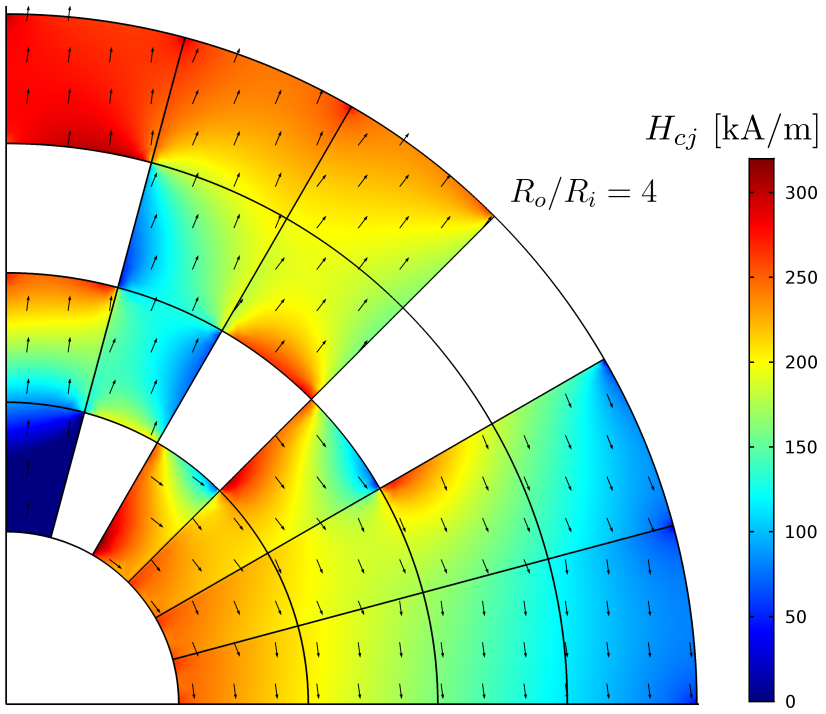

Figure 6.6: Topology optimized permanent magnet with ferrite C9 magnet material and Ro/Ri = 4. Bulk remanence orientations are constrained to radial and tangential directions to facilitate manufacturing. Average magnetic flux density of 0.366 T in bore.

6.3.4 Simultaneous optimization of material distribution and remanence orientation

The required coercivity is correlated with the tendency of a magnet to bend lines of magnetic flux. As such, the design vector is reformulated as $\vec{x} =< \rho_1, ..., \rho_n, \theta_1, ..., \theta_n >$ to include the local remanence orientation as a design variable in the optimization. ρ_i takes integer values of 1 or 2, corresponding to air and permanent magnet, respectively, and θ_i is a continuous variable describing the remanence orientation of each segment. The result is a mixed-integer optimization problem with 48 design variables corresponding to 24 discrete domains. To accommodate the increased design space, the genetic algorithm population size is increased from 500 to 10,000.

The optimal magnet design with ferrite C9 and $R_o/R_i = 4$ is shown in Fig. 6.7. The design produces an average magnetic flux density of 0.483 T, which is a 15.8 %, 32.0 % and 39.2 % improvement over the 0.417, 0.366 and 0.347 T average fields produced by the optimized designs with Halbach orientations (Fig. 6.3), radial-tangential remanence orientations (Fig. 6.6) and the benchmark Halbach cylinder (Table 6.1), respectively, albeit with increased manufacturing complexity. This is summarized in Table 6.2. The remanence orientations deviate most from the Halbach cylinder (Eq. 6.1) at the outer polar and inner equatorial positions. While the final design consists entirely of permanent magnet, it should be emphasized that the optimization procedure iteratively improves upon a feasible design (i.e. a design satisfying the coercivity constraint). This requires a large number of intermediate designs with void fractions resembling the topologies presented above.

Table 6.2: Summary of magnet designs. Areas calculated with R_i=12.5mm

Material	Formulation	R_o/R_i	$\bar{B}$ [T]	A_{mag} [m^2]	M^*[−]
ferrite-C9	Benchmark (A) Fig. 6.2	2.8	0.347	0.00335	0.122
MnBi	Benchmark (A) Fig. 6.2	2.7	0.526	0.00308	0.122
NdFeB-N42	Benchmark (A) Fig. 6.2	ø	ø	ø	ø
ferrite-C9	Halbach (B) Fig. 6.3	4	0.417	0.00578	0.102
ferrite-C9	Halbach (B) Fig. 6.3	6	0.486	0.01424	0.056
ferrite-C9	Halbach (B) Fig. 6.3	8	0.562	0.02523	0.042
MnBi	Halbach (B) Fig. 6.4	4	0.652	0.00595	0.097
MnBi	Halbach (B) Fig. 6.4	6	0.786	0.01618	0.052
MnBi	Halbach (B) Fig. 6.4	8	0.899	0.02931	0.037
NdFeB-N42	Halbach (B) Fig. 6.5	4	1.127	0.00402	0.094
NdFeB-N42	Halbach (B) Fig. 6.5	6	1.423	0.01035	0.058
NdFeB-N42	Halbach (B) Fig. 6.5	8	1.388	0.01600	0.036
ferrite-C9	Rad-tan (C) Fig. 6.6	4	0.366	0.00578	0.078
ferrite-C9	Continuous (D) Fig. 6.7	4	0.483	0.00736	0.108

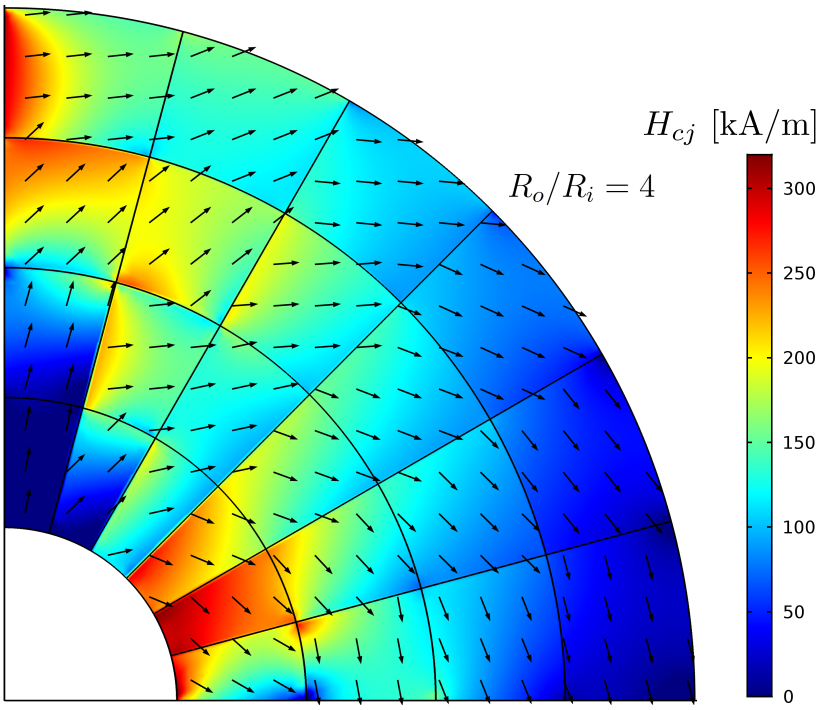

Figure 6.7: Magnet design with material distribution and remanence orientation optimized using ferrite C9 permanent magnet material and Ro/Ri = 4. Average magnetic flux density of 0.483 T is produced in bore.

6.4 Discussion

While flux densities are improved using finite coercivity permanent magnet materials, the required magnet area increases rapidly with field strength. The magnet efficiency, defined as the ratio of magnetic energy in the high field region to the energy stored in the permanent magnet material, is calculated as:

$$M^* \equiv \frac{A_{bore}}{A_{mag}} \left(\frac{\bar{B}}{B_{rem}} \right)^2 \tag{6.6}$$

and is summarized for each design in Table 6.2. Although the proposed methodology allows reduced rare-earth permanent magnet materials to be used in higher-field applications, none of the magnet efficiencies exceed the cylindrical Halbach array.

For well-defined applications, the objective function can be reformulated to minimize cost subject to performance constraints. Teyber *et al.*(2017) [22] found the magnet design minimizing the combined capital and operating costs of a magnetic refrigerator. Unlike the present work, the implementation focused on higher-energy product Dy-NdFeB permanent magnet segments with discrete remanence orientations. Alternatively, applications requiring a homogenous field can minimize standard deviation subject to a predefined average magnetic flux density.

The optimized topologies maximize magnetic induction with rare-earth-free (ferrite C9, MnBi) and reduced-rare-earth (Dy-free NdFeB-N42) materials, however the magnetization and assembly of individual segments can be costly. While the manufacturing complexity is reduced by constraining remanence orientations to the radial and tangential directions, the flux density is increased by 32 % for the same outer radius with spatially varying remanence orientations. New methods for 3D printing permanent magnets are promising and would enable the optimal designs in the present work [167, 168]. Arbitrary magnet shapes can be printed with minimal tooling and near-zero material waste, however present state-of-the-art manufacturing methods cannot produce monolithic magnet structures with the spatially varying remanence orientations of Fig. 6.7.

Finally, it should be noted that the finite coercivity constraint is conservative in that any design experiencing demagnetization is completely disqualified. It may be more practical to penalize designs where, for example, an excess of 1% of the domain demagnetizes. Additionally, future works should implement experimental hysteresis curves for each material. Both of these suggestions, however, add a layer of iteration and increase simulation convergence times.

6.5 Conclusion

While the discovery and improvement of rare-earth-free permanent magnet materials is imperative, the role of magnetic circuit design is becoming increasingly important. Literature on topology optimization, however, has not incorporated the permanent magnet failure process stemming from reduced coercivity. In this work, the flux density in the bore of a Halbach cylinder is maximized using rare-earth-free C9 ferrite, rare-earth-free MnBi and Dy-free NdFeB-N42 magnet materials yielding flux densities 70% stronger than the benchmark Halbach array. Three scenarios are simulated with C9 ferrite that explore the tradeoff between design sophistication and manufacturability. While a magnetic flux density of 0.366 T is obtained with magnet segments constrained to the radial and tangential directions, the induction is improved to 0.483 T by including local remanence orientations in the optimization.

Acknowledgements

The support of the Natural Sciences and Engineering Research Council of Canada and BASF New Business is greatly appreciated.

Chapter 7

Permanent magnet design for magnetic heat pumps using total cost minimization

Journal of Magnetism and Magnetic Materials 442 (2017), 87-96.

Abstract

The active magnetic regenerator (AMR) is an attractive technology for efficient heat pumps and cooling systems. The costs associated with a permanent magnet for near room temperature applications are a central issue which must be solved for broad market implementation. To address this problem, we present a permanent magnet topology optimization to minimize the total cost of cooling using a thermoeconomic cost-rate balance coupled with an AMR model. A genetic algorithm identifies cost-minimizing magnet topologies. For a fixed temperature span of 15 K and 4.2 kg of gadolinium, the optimal magnet configuration provides 3.3 kW of cooling power with a second law efficiency (η_{II}) of 0.33 using 16.3 kg of permanent magnet material.

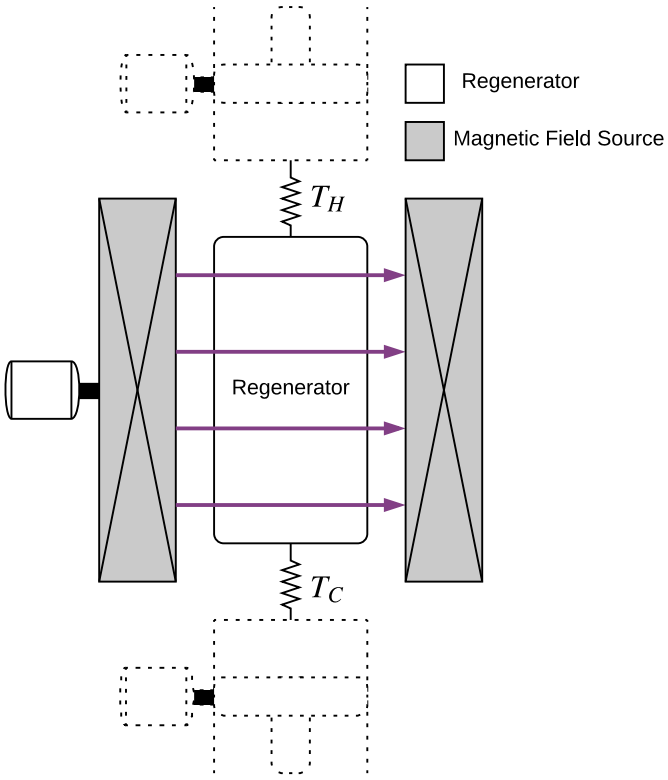

Figure 7.1: Graphical abstract of chapter 7, focusing on the topology optimization of permanent magnet structures to minimize the cost of an active magnetic regenerator.

Nomenclature

Roman

B	magnetic flux density [T]
$\dot{C}$	cost rate [$/h]
$\not{c}$	cost per unit exergy [$/kWh]
c	specific heat [J/kgK]
cf	capacity factor [-]
$\dot{E}x_{\mathrm{Q}}$	exergetic cooling power [W]
f	frequency [Hz]
g	air gap between cylinders [m]
H	magnetic field strength [A/m]
i_{d}	discount rate[-]
L	length [m]
m	mass [kg]
M^*	magnet efficiency [-]
N_{D}	demagnetization factor[-]
$2p$	magnet poles [-]
P	magnet utilization [-]
$\dot{Q}_{\mathrm{c}}$	cooling capacity [W]
r	radius [m]
R	thermal mass ratio [-]
R_{HC}	heat leak thermal resistance [K/W]
T	temperature [K]
t	time [s]
V	Volume [m^3]
$\dot{V}$	volumetric flow rate [$\mathrm{m}^3\mathrm{s}^{-1}$]
V_{D}	displaced volume [cm^3]
V_{M}	Magnetic scalar potential [A]
x	coordinate of regenerator length
$\dot{Z}$	ammortized capital costs [$/h]

Greek

γ	cost per unit mass [\$/kg]
ε	porosity [-]
μ	magnetic permeability [H/m]
κ	effective thermal conductivity [-]
Λ_{cool}	magnet figure of merit [$T^{2/3}$]
η_{II}	second law efficiency [-]
Φ	utilization [-]
Ψ	topology design vector [-]
σ	specific magnetization [Am^2/kg]
τ	cycle period [s]
θ	angular coordinate [rad]
χ	domain material [-]
ζ	reduced magnetocaloric effect [-]

Subscripts and Superscripts

ad	adiabatic
app	applied field
C	cold reservoir or cold side
cj	intrinsic coercivity
csg	regenerator casing
D	displaced
f	fluid
FWA	flow weighted average
geo	geometry
H	hot reservoir or hot side
int	internal field
M	magnetic work
MCM	magnetocaloric material
PMM	permanent magnet material
p	constant pressure
reg	regenerator
rem	remanence
s	solid
SMM	soft magnetic material
span	temperature span

7.1 Introduction

Energy conversion devices using solid-state magnetocaloric materials (MCM) have the potential to reduce energy consumption and mitigate environmental pollutants [16, 12, 13, 17]. Although permanent magnet based active magnetic regenerator (AMR) devices have demonstrated commercially relevant temperatures spans, cooling powers and efficiencies [52, 53, 23, 174, 24], magnetic field generator and refrigerant costs must be reduced for broad market penetration.

A previous assessment of an AMR cooling device showed that the permanent magnet cost is of greatest importance to be competitive with existing air conditioning technologies [175]. The evaluation was based on the cost of cooling in \$/kW, where the device performance was evaluated from the material T-S diagram and the magnetic field was generated using a theoretical Halbach cylinder. Compared with the permanent magnet, the refrigerant cost was found to be almost insignificant when using $La(Fe_{1\text{-x}}Si_{\text{x}})_{13}$ with a cost of 8 \$/kg. Using a similar methodology, Vuarnoz *et al.* (2012) [176] investigated a magnetocaloric heat engine and found the technology to be economically feasible for electricity prices between $0.1 - 0.2$ CHF/kWh.

Bjørk *et al.* (2011) [177] investigated the regenerator configuration, magnetic field source and operating parameters that minimize the capital costs of a refrigerator using a one-dimensional AMR model. A device is optimized for both a theoretical Halbach cylinder and a theoretical magnet with maximum energy efficiency ($M^* = 0.25$) [158].

$$M^* \equiv \frac{V_{\text{bore}}}{V_{\text{mag}}}\left(\frac{B_{\text{bore}}}{B_{\text{rem}}}\right)^2 \tag{7.1}$$

Tura and Rowe (2014) [70] considered both the capital and operating costs of a dual-regenerator AMR with theoretical concentric Halbach arrays. An optimization routine determines the geometry and operating conditions that minimize the total cost of cooling using analytical expressions describing an AMR [115, 116]. With a temperature span of 50 K and a cooling power of 100 W, the optimized design has magnet and refrigerant capital costs of \$100 and \$40, respectively, using an ideal refrigerant with an assumed cost of 150 \$/kg.

More recently, Bjørk *et al.* (2016) [71] designed an operating scheme based on EU-directive 1060/2010 and European A^{+++} standards to minimize both the capital and operating costs of a magnetic refrigerator. A Halbach cylinder is used and the effects of a finite length magnet are included. The simulated lifetime cost of $\$150 - \$400$ is

shown to be competitive with comparable vapor compression devices.

These works couple AMR models with economic assessment tools to optimize the geometry and operating parameters of an AMR. Of the various magnetic circuits available [29, 31], each study uses a Halbach cylinder [28, 74, 75] and concludes that the permanent magnet material (PMM) dominates the capital cost of an AMR. While optimization methods have been proposed for permanent magnet structures [37, 35, 178, 179, 38, 39], none minimize the lifetime cost of an AMR. Instead, the most widely used objective function for magnetic refrigeration field generators is the Λ_{cool} parameter proposed by Bjørk *et al.* (2008) [74].

$$\Lambda_{\text{cool}} = (B_{\text{high}}^{2/3} - B_{\text{Low}}^{2/3}) \frac{V_{\text{bore}}}{V_{\text{mag}}} P_{\text{field}} \tag{7.2}$$

Λ_{cool} resembles Eq. 7.1, but reflects the scaling of the magnetocaloric effect with applied field and the importance of minimizing the low field strength (B_{low}). Although Λ_{cool} encapsulates important design parameters, it is not suitable as an objective function for design optimization: for a theoretical Halbach cylinder, $\Lambda_{\text{cool}} = \frac{r_{\text{in}}^2}{r_{\text{out}}^2 - r_{\text{in}}^2}(B_{\text{rem}} \ln \frac{r_{\text{out}}}{r_{\text{in}}})^{2/3}$ which tends to infinity with increasing r_{in} and decreasing cylinder thickness. This does not yield low cost refrigeration, as will be shown.

Bjørk *et al.* (2010) [164] addresses this shortcoming by defining the air gap size *a priori*, and designs a state of the art magnetic field generator by maximizing Λ_{cool} in a segmented adaptation of the nested quadrupolar Halbach array. The theoretical remanence is defined as

$$< B_{\text{rem},r}, B_{\text{rem},\theta} >= ||B_{\text{rem}}|| < cos(p\theta), sin(p\theta) > \tag{7.3}$$

where $2p$ is the number of poles, r and θ are the polar coordinate axis. The optimized field generator is effective and efficient, however the optimized design uses sophisticated magnet shapes with custom remanence directions that cost several times more than their rectangular counterpart [180]. Bjørk re-investigates the nested Halbach design [41] using a topology optimization to replace continuously oriented permanent magnet material (as in Eq. 7.3) with soft magnetic material (SMM) over a continuous domain to maximize Λ_{cool}. A high figure of merit is presented, however AMR operation, magnet manufacturability and finite coercive strength are not considered.

Monfared *et al.* (2014) [181] reported that magnetic refrigeration can only reduce environmental impacts if permanent magnet material is re-used, demonstrating how manufacturability and the end-of-life recyclability must be considered with the capital

and operating costs. An appealing solution is to use rectangular magnet segments, as the production costs are significantly lower than magnets with custom shapes or remanence orientations. Rectangular magnets are easily re-purposed, through material recycling [142, 150, 182] or a consumer buy-back program where reclaimed magnets directly supply production inventory.

In this paper, we propose a permanent magnet design methodology to minimize the total cost of cooling for a magnetic refrigerator. A commercially oriented magnetic circuit is created by decomposing a sophisticated magnet design into a collection of small, rectangular elements. Each element is assigned the properties of air, soft magnetic material or permanent magnet material with discretized remanence orientations (north, east, south, west). A magnet topology is used to simulate the magnetic field waveform for an AMR model. The performance and topology are used to evaluate the capital and operating costs based on a thermoeconomic cost-rate balance, which serves as the optimization objective function. A genetic algorithm identifies optimal topologies yielding novel magnet configurations oriented towards low-cost refrigeration or heat pumping.

7.2 Methodology

7.2.1 Cost of cooling

The objective of the topology optimization is to minimize the cost of a magnetic refrigerator. A thermoeconomic approach is used, which allots costs to streams with thermodynamic value or exergy. Applying a cost-rate balance to a cooling device, where capital and operating costs are used to provide a cooling service, yields

$$\dot{C}_{\mathrm{Q}} = \dot{C}_{\mathrm{op}} + \dot{Z} \tag{7.4}$$

in \$/h where streams with exergetic value are denoted by $\dot{C}$. The ammortized capital costs, $\dot{Z}$, consist of permanent magnet material (PMM), magnetocaloric material (MCM) and soft magnetic material (SMM). Each cost rate is then decomposed into the product of exergy flux and the cost per unit exergy, e.g. $\dot{C}_{\mathrm{Q}} = \not{c}_{\mathrm{Q}}\dot{E}x_{\mathrm{Q}}$ ($\not{c}$ is used to distinguish costs from specific heat, c). The exergetic cooling power of a refrigerator operating between finite thermal reservoirs is described as

$$\dot{E}x_{\mathrm{Q}} = \dot{Q}_{\mathrm{C}}\frac{T_{\mathrm{span}}}{T_{\mathrm{C}}} \tag{7.5}$$

Following the thermoeconomic approach used by Rowe (2011) [69, 67], the cost per exergetic cooling, $\not{c}_{\mathrm{Q}}$ in \$/kWh, can be expressed as

$$\not{c}_{\mathrm{Q}} = \frac{\mathrm{CRF}}{\dot{E}x_{\mathrm{Q}} \cdot cf}\left(\gamma_{\mathrm{PMM}}\mathrm{m}_{\mathrm{PMM}} + \gamma_{\mathrm{MCM}}\mathrm{m}_{\mathrm{MCM}} + \gamma_{\mathrm{SMM}}\mathrm{m}_{\mathrm{SMM}}\right) + \not{c}_{\mathrm{e}}\left(\frac{\dot{W}_{\mathrm{net}}}{\dot{E}x_{\mathrm{Q}}}\right) \tag{7.6}$$

where γ_{PMM}, γ_{MCM} and γ_{SMM} are the costs of NbFeB permanent magnet material, magnetocaloric material and soft magnetic material in \$/kg, m is the respective mass in kg, $\not{c}_{\mathrm{e}}$ is the cost of electricity in \$/kWh and the capacity factor, cf, is the operating duty cycle. The net work consumption ($\dot{W}_{\mathrm{net}}$) and exergetic cooling power are obtained from a coupled AMR model.

The capital recovery factor (CRF) discounts absolute capital costs into an annual cost rate over the expected lifetime of N years at a rate i_{d}. The discounted annual capital cost is then converted to an hourly value to work with familiar units of energy (e.g. kWh)

$$CRF = \frac{i_{\mathrm{d}}}{1-(1+i_{\mathrm{d}})^{-N}} \tag{7.7}$$

The AMR cooling power and efficiency increase with the applied field strength, reducing the operating cost at the expense of increased permanent magnet mass. The minimum value of $\not{\epsilon}_{\mathrm{Q}}$ describes the optimum balance of capital investment and operating costs, and is the objective function in the present optimization.

7.2.2 Semi-analytic AMR model

The cost per exergetic cooling, $\not{\epsilon}_{\mathrm{Q}}$, is a function of the exergetic cooling power and power consumption which are obtained from an AMR model. State-of-the-art AMR models numerically solve the coupled energy equations for the solid and fluid phases [183, 109, 110, 98, 113, 184] and post-calculate the cooling power and work input from the dynamic temperature distributions. Although these sophisticated modeling tools have shown good agreement with AMR experiments [23, 18, 185, 1, 186], the convergence time is prohibitively large for the proposed topology optimization which required 10^6 simulations.

Rowe (2012) [115, 116] proposed the use of analytical expressions to describe the magnetic work and cooling power in an AMR. These expressions were obtained under the assumption of local thermal equilibrium between the solid and fluid phases in the regenerator matrix, which results in a single differential energy equation for the porous media [82]. An effective conductivity which includes finite convection accounts for the imperfect regenerator having non-equilibrium between solid and fluid. In addition, a constant reduced adiabatic temperature change is assumed along the regenerator length. The derived magnetic work and cooling power expressions yield a fast solution and have been validated with a number of experimental devices [26, 187].

Using the formulation presented by Burdyny *et al* (2014) [117], the semi-analytic cooling power is:

$$\dot{Q}_{\mathrm{C,AMR}} = \left(\frac{m_{\mathrm{MCM}} c_{\mathrm{s}}}{\tau_{\mathrm{cycle}}}\right)\frac{\Phi}{R}\zeta T_{\mathrm{C}}\left[1-\left(\frac{\Phi}{2R}+\left(\frac{\Phi\zeta}{R\kappa}\right)^{-1}\right)\left(\frac{T_{\mathrm{H}}}{T_{\mathrm{C}}}-1\right)\right] \tag{7.8}$$

where m_{MCM} is the mass of magnetocaloric material, c_{s} is the cycle-averaged solid specific heat, τ_{cycle} is the cycle period, T_{H} and T_{C} are the hot and cold reservoir temperatures. Utilization (Φ) is a measure of the displaced fluid volume in a regenerative blow and is defined as the ratio of the fluid to solid thermal mass:

$$\Phi = \frac{m_{\mathrm{d}} c_{\mathrm{p}}}{m_{\mathrm{MCM}} c_{\mathrm{s}}} \tag{7.9}$$

where m_{d} is the mass of displaced fluid and c_{p} is the average fluid specific heat. R is the thermal mass ratio:

$$R = 1 + \frac{m_{\mathrm{f}} c_{\mathrm{p}}}{m_{\mathrm{MCM}} c_{\mathrm{s}}} \tag{7.10}$$

where m_{f} is the entrained fluid mass in the pores. κ is the effective thermal conductivity which contains a contribution from thermal diffusion [188, 189] and a degradation factor to account for finite convective heat transfer. Further implementation details can be found in Burdyny *et al.*(2014) [117].

ζ is the *effective* reduced adiabatic temperature change, which approximates the spatially varying reduced magnetocaloric effect with an equivalent value. In the present work, ζ is the integrated average over the regenerator length which was found to work well with second order magnetocaloric materials [117].

$$\zeta = \frac{1}{T_{\mathrm{H}} - T_{\mathrm{C}}} \int_{T_{\mathrm{C}}}^{T_{\mathrm{H}}} \frac{\Delta T_{\mathrm{ad}}(T)}{T} dT \tag{7.11}$$

The net work input, $\dot{W}_{\mathrm{net}}$, is the sum of the magnetic and pump work, where the average pressure drop is evaluated according to Ergun (1952) [80]. The semi-analytic expression for magnetic work is given by:

$$\dot{W}_{\mathrm{M}} = \left(\frac{\mathrm{m}_{\mathrm{MCM}} c_{\mathrm{s}}}{\tau_{\mathrm{cycle}}}\right) \zeta \left[\frac{R-1}{R} \overline{\Delta T}_{\mathrm{ad}} + \frac{\Phi}{R}(T_{\mathrm{H}} - T_{\mathrm{C}})\right] \tag{7.12}$$

where $\overline{\Delta T}_{\mathrm{ad}}$ is the average adiabatic temperature change. As shown in the AMR energy balance in Fig. 7.2, heat leaks into the cold side are modeled with a thermal resistance (R_{HC}), reducing the delivered cooling power ($\dot{Q}_{\mathrm{C,net}}$) from Eq. 7.8. The cooling power is then multiplied by the number of regenerators in the system.

$$\dot{Q}_{\mathrm{C,net}} = \mathrm{n}_{\mathrm{reg}} (\dot{Q}_{\mathrm{C,AMR}} - \frac{T_{\mathrm{span}}}{R_{\mathrm{HC}}}) \tag{7.13}$$

7.2.3 MCE implementation

In the semi-analytic AMR expressions, the specific heat and adiabatic temperature change are interpolated from discrete low and high magnetic field strengths. The

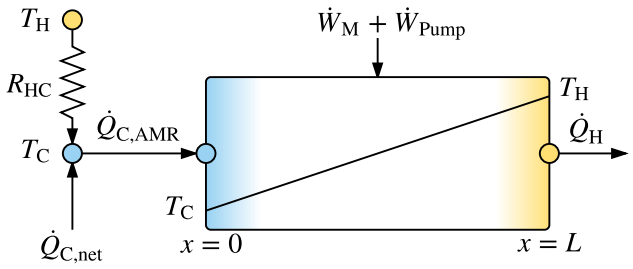

Figure 7.2: Schematic of single AMR showing energy balance with assumed linear temperature distribution. Heat leaks reduce delivered cooling power.

magnetic field waveform, however, is continuous. Instead of averaging the field over the blow periods, the flow-weighted average field (FWA) is used [83].

$$\Delta B_{\mathrm{FWA}} = \frac{1}{V_{\mathrm{D}}}\left(\int_0^{0.5\tau_{\mathrm{cycle}}} |B(t)\dot{V}(t)|dt - \int_{0.5\tau_{\mathrm{cycle}}}^{\tau_{\mathrm{cycle}}} |B(t)\dot{V}(t)|dt\right) \tag{7.14}$$

Demagnetization losses relating the applied field to the internal field are implemented as:

$$B_{\mathrm{int}} = B_{\mathrm{app}} - \mu_0 \rho_{\mathrm{s}} N_{\mathrm{D}} \sigma(\overline{T}, B_{\mathrm{app}}) \tag{7.15}$$

where μ_0 is the permeability of free space, ρ_{s} is the refrigerant density, N_{D} is the average demagnetization factor and σ is the specific magnetization of the refrigerant. The following correlation has been proposed for a bed of packed particles [118]

$$N_{\mathrm{D}} = N_{\mathrm{D,geo}} + (1-\epsilon)(N_{\mathrm{D,csg}} - N_{\mathrm{D,geo}}) \tag{7.16}$$

where $N_{\mathrm{D,geo}} = 1/3$ for a spherical particle, ϵ is the regenerator porosity and $N_{\mathrm{D,csg}}$ is the demagnetization of the regenerator geometry [119]. The required specific heat, specific magnetization and magnetocaloric effect are generated using the Mean Field Theory (MFT) with Gd properties [118, 120]

7.2.4 Magnetic field simulation

The magnetic field is numerically evaluated using COMSOL Multiphysics 5.2 [190]. The magnetostatics, no current formulation is used in a two-dimensional domain allowing use of the magnetic scalar potential (V_{m}) defined as $\vec{H} = -\nabla V_{\mathrm{M}}$. Substituting the constitutive relation for permanent magnets ($\vec{B} = \mu\vec{H} + \vec{B}_{\mathrm{rem}}$) into Gauss's law of magnetism ($\nabla \cdot \vec{B} = 0$) yields the PDE governing the magnetic field distribution in the permanent magnet material

$$\nabla \cdot (\mu \nabla V_{\mathrm{M}} - \vec{B}_{\mathrm{rem}}) = 0 \tag{7.17}$$

where $\mu = \mu_0 \mu_{\mathrm{r}}$, μ_{r} is the relative permeability and $\vec{B}_{\mathrm{rem}}$ is the remanence vector.

Air and NdFeB magnets are modeled with a constant permeability of $\mu_{\mathrm{r}} = 1$ and $\mu_{\mathrm{r}} = 1.05$, respectively. Soft magnetic material is modeled as 1018 steel, and saturation effects are included with experimental data from the COMSOL Multiphysics material library.

When the reverse component of the applied field exceeds the intrinsic coercivity, H_{cj}, a permanent magnet is locally demagnetized. Eq. 7.18 is evaluated throughout the domain and used to determine the required magnet grade for the simulated topology [74, 75].

$$\left(\mu H_{\mathrm{cj}} + \mu\vec{H} \cdot \frac{\vec{B}_{\mathrm{rem}}}{|\vec{B}_{\mathrm{rem}}|}\right) \geq 0 \tag{7.18}$$

7.2.5 Topology optimization

The design vector, $\Psi(\chi_1, ..., \chi_n)$, defines the topology and contains an integer valued design variable, χ, for each of n domains. χ defines the material or magnet direction for the corresponding domain as summarized in Table 7.1.

Table 7.1: Design variable definitions.

χ	1	2	3	4	5	6
Material	air	SMM	PMM $\uparrow$	PMM $\rightarrow$	PMM $\downarrow$	PMM $\leftarrow$

As the objective function is non-differentiable with respect to the design variables, a metaheuristic optimization algorithm (e.g. particle swarm, genetic algorithm, simulated annealing) is required. The topology optimization is implemented in MATLAB using the genetic algorithm based on its stochastic nature and ability to accommodate integer-valued design variables.

The algorithm begins with an initial population of $m = 100$ randomly generated topologies, $[\Psi_1, ..., \Psi_j, ..., \Psi_{100}]$. After evaluating the entire population, individuals with the highest fitness (lowest $\not{\phi}_Q$) are selected as elite and are cloned into the next generation. The number of elite individuals is 20% of the population size. With non-elite individuals, children are produced by either perturbing a single parent (mutation) or combining the topology of two favorable parents (crossover). Mutation encourages design diversity while parent crossover facilitates convergence. A crossover fraction of 0.6 is used in the present work. Convergence is determined when the optimal topology fails to improve for 2,000 generations, which is achieved in three weeks with an AMD FX-8350 processor. Convergence can be accelerated by seeding known designs into the initial population, however the likelihood of a local optima is increased. Further genetic algorithm implementation details can be found in the MATLAB documentation.

As AMR operation is highly sensitive to Φ (Eq. 4.2), the semi-analytical expressions are evaluated over a range of displaced volumes in a sub-optimization loop to identify the minimum cost for each magnet topology. A flow chart of the optimization process is shown in Fig. 7.3.

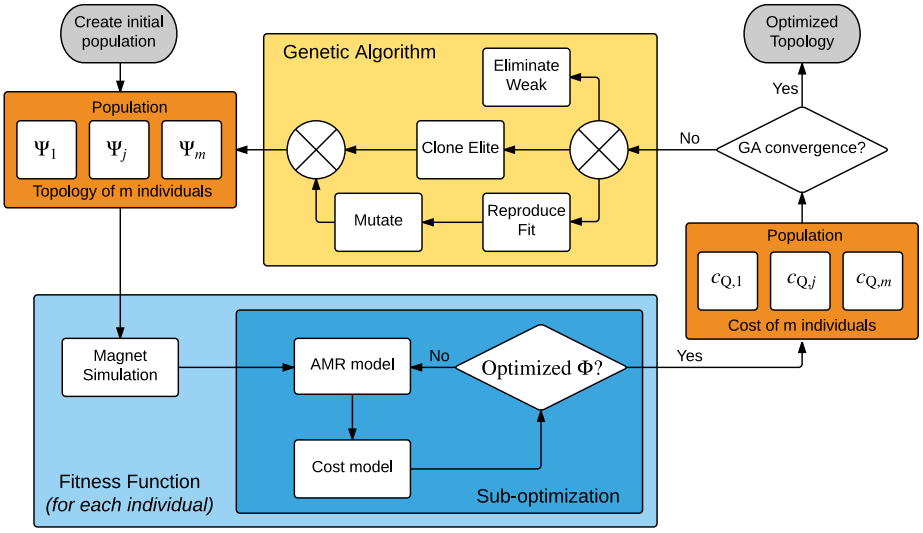

Figure 7.3: Optimization flowchart. Each population is a collection of magnet topologies. The associated cost is determined in the fitness function (blue), which is evaluated for each individual.

7.3 Design configuration

We consider the magnetic field generator designed by Bjørk *et al.* (2010) [164, 56], inspired from the nested quadrupolar Halbach array. The upper region of Fig. 7.4 shows the distribution of remanence with contours of magnetic flux density [32] for a theoretical Halbach cylinder with $p = -2$ nested inside an outer Halbach with $p = 2$ as described by Eq. 7.3 above.

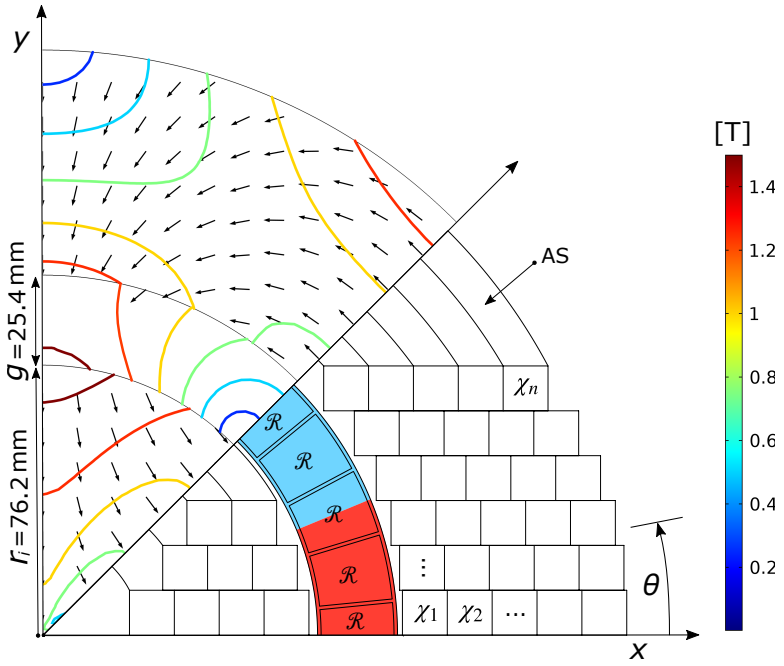

Figure 7.4: Geometry of dual nested Halbach array with theoretical remanence distribution shown next to segmented adaptation for topology optimization. Red and blue shading indicates the high and low field regions, respectively.

A fixed cylinder gap width of $g = 25.4$ mm, an inner radius of $r_i = 76.2$ mm and an external radius of $r_o = 165.1$ mm are considered. Square 12.7 mm magnet segments define a grid of 39 discrete domains that are assigned properties of steel, air or permanent magnet as summarized in Table 7.1. Annular segments (AS) are restricted to steel or air.

Currently, likely applications of permanent magnet refrigeration devices are those requiring low temperature spans, high cooling capacities and quiet operation. As such, we consider a fixed rejection temperature of $T_{\mathrm{H}} = 30°C$ and a cold side temperature of $T_{\mathrm{C}} = 15°C$ (i.e. $T_{\mathrm{span}} = 15°C$). A total of 32 annular regenerators with a 1 mm casing thickness and a length of 76.2 mm fill the magnet air gap as shown in Fig. 7.4.

The regenerator length and geometry are based on previous experiments [61] and entropy generation minimization analysis [25]. To improve field homogeneity, the magnet extends 6.4 mm beyond the regenerator on both ends.

Each regenerator consists of 0.13 kg of 300 μm Gd spheres (4.19 kg total), packed with a porosity of $\epsilon = 0.36$. A heat leak resistance of $R_{\mathrm{HC}} = 10$ K/W per regenerator is used with a cycle operating frequency of 2 Hz and a sinusoidal fluid velocity waveform. The resistive heat leak and frequency are based on Burdyny *et al.*(2014) [187] and Engelbrecht *et al.* (2012) [56], respectively.

The cost of electricity, $\not{c}_{\mathrm{e}}$, is 0.12 \$/kWh based on the US residential average. A capacity factor of 0.35 is assumed over a lifetime of $N = 10$ years with a discount ratio of $i_{\mathrm{d}} = 5\%$, as in Tura and Rowe (2014) [70]. A magnetocaloric material cost of $\gamma_{\mathrm{MCM}} = 20$ \$/kg is considered, as in [71], with a 1018 steel cost of $\gamma_{\mathrm{SMM}} = 5$ \$/kg. The cost of magnetocaloric material reflects optimistic expectations of a mass-produced refrigerant with comparable properties to Gadolinium. N42 grade NdFeB magnets are considered with $B_{\mathrm{rem}} = 1.3\ T$.

The magnet cost as a function of the required intrinsic coercive strength (Eq. 7.18) is shown below in Fig. 7.5. The \$10 increase in cost from N42 to N42SH magnet grades is based on the 4% increase in Dysprosium content [180]. The price increase beyond 1592 kA/m is set arbitrarily high to penalize designs requiring premium magnet grades (e.g. N42UH). Although the proposed methodology is well suited for reusing permanent magnet material, capital recovery is not considered; following the conservative approach in Bjørk *et al.* (2016) [71].

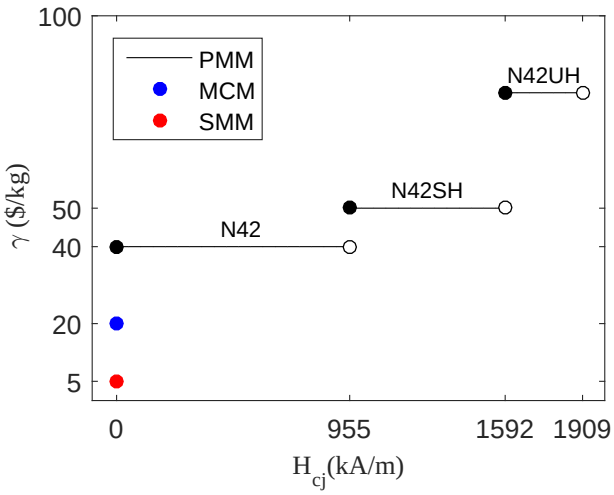

Figure 7.5: Specific cost versus magnet grade and required coercivity. All grades have a remanence magnitude of 1.3 T.

7.4 Results

7.4.1 AMR Results

Fig. 7.6 shows the semi-analytical model results for cooling power (left) and second-law efficiency (right) versus reference utilization (Φ evaluated using peak zero-field specific heat) for a range of applied field strengths. The cooling capacity strictly increases with applied field strength, while a maximum is observed with increasing utilization (Φ_{ref}). The second-law efficiency ($\eta_{\text{II}} = \dot{E}x_{\text{Q}}/\dot{W}_{\text{net}}$) also increases with applied field, however benefits diminish beyond applied field strengths of 0.75 T. Although large cooling powers can be obtained by increasing Φ_{ref} and B_{app}, the efficiency and capital cost are negatively impacted as a result of the increased pump work and permanent magnet mass. This illustrates the competing cost objectives in the objective function (Eq. 7.6).

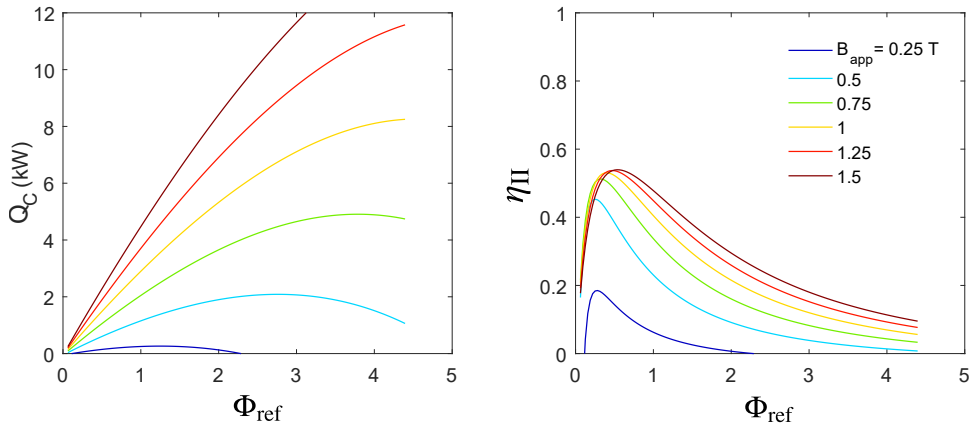

Figure 7.6: AMR performance versus displaced volume (Φ_{ref}) for various applied field strengths.

7.4.2 Topology results

The final magnet topology is shown below in Fig. 7.7, presenting the cost-minimized balance of magnet mass and AMR performance. Red segments indicate permanent magnet material with remanence direction shown by the arrows, and gray segments indicate 1018 steel. Streamlines of magnetic flux intensity are shown with a color scale from 0-1.5 T. The optimized configuration has a cost per exergetic cooling of $\dot{\epsilon}_Q = 0.61$ \$/kWh yielding a second law efficiency of 33% at a reference utilization of 1.26. The resulting capital and lifetime operating costs are $\$1,010$ and $\$1,500$, respectively.

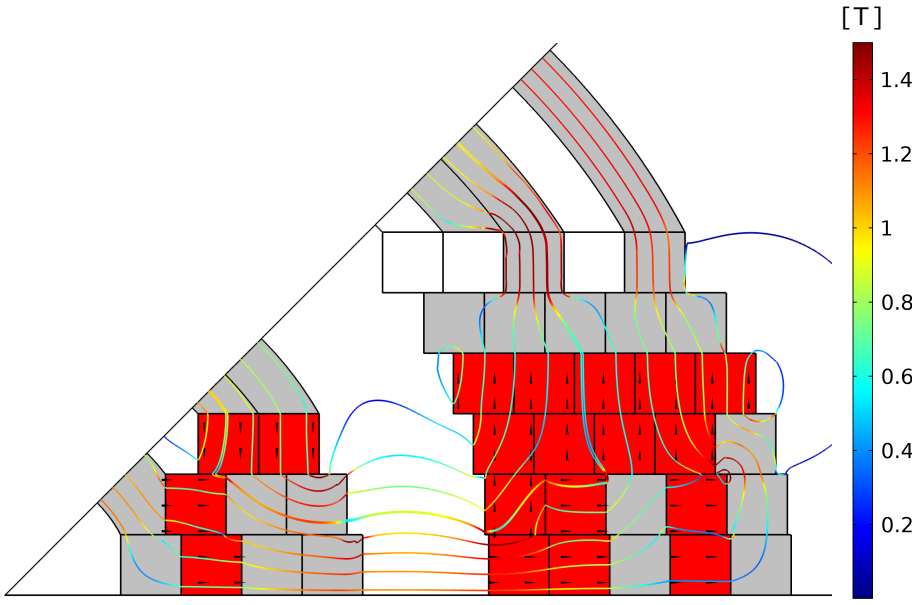

Figure 7.7: Cost-minimized magnetic circuit with streamlines of magnetic flux.

The resulting design is non-trivial and provides insight on: (i) the optimal amount of permanent magnet material for the considered magnetic refrigeration application, and (ii) the magnetic circuit that optimally distributes costly permanent magnet material. Regarding point (i), the peak field strength is of the order reported by Tura and Rowe (2014) [70], however the presented cost-minimized magnetic circuit makes more efficient use of permanent magnet material.

Considering point (ii), several design traits are observed. Both the inner and outer Halbach rings have magnets orthogonal to the air gap (west-east) and flux-focusing magnets perpendicular to the air gap (north-south, south-north). In the inner ring, the main magnets and flux-focusing magnets converge in a soft magnetic pole-piece

that helps distribute the flux as preferred by the outer magnet arrangement. A similar trend is seen in the high field region of the outer ring where the main magnet and flux-focusing magnet branches form two parallel paths for magnetic field lines. The soft magnetic pole-piece is not present, suggesting permanent magnet material is more important in the exterior Halbach ring.

7.4.3 Alternative metrics

The proposed methodology is now applied on the figures of merit presented in Eqs. 7.1 and 7.2. The topology and magnetic field distributions with M^* and Λ_{cool} as objective functions are shown in Fig. 7.8. While the M^* optimized topology resembles the cost-minimized design in Fig. 7.7, the Λ_{cool} optimized magnet contains a single magnet element.

The magnetic field waveforms are shown in Fig. 7.9, where B_{app} is averaged over the regenerator at each θ. The four designs, D_1-D_4, correspond to the theoretical Halbach cylinder (Eq. 7.3) and the c_{Q}, M^* and Λ_{cool} optimized magnetic circuits, respectively. The vertical line at $\theta = 22.5°$ divides the high and low field regions, shown in Fig. 7.4. Although the theoretical Halbach (D_1) generates the strongest magnetic field of 1.4 T, the low-field strength is non-zero which reduces the effective field change.

7.5 Discussion

The magnetic circuit and AMR performance results are shown in Tables 7.2 and 7.3, respectively. At a glance, the M^* optimized circuit appears to be more favorable than the $\not{c}_{\text{Q}}$ optimized circuit, as a 2.5% reduction in applied field strength brings a 10.5% reduction in permanent magnet mass. The required coercivity of 2150 kA/m, however, is beyond what is commercially available with a remanence of 1.3 T and cannot be manufactured with N42-series magnet material.

Table 7.2: Magnet results for three optimized topology strategies.

	$\overline{B_{\text{H}}}$ (T)	$\overline{B_{\text{L}}}$ (T)	ΔB_{FWA} (T)	m_{mag} (kg)	H_{cj} (kA/m)
D_1−HB	1.40	0.36	0.77	47.6	916
$\text{D}_2 - c_{\text{Q}}$	1.13	0.01	0.90	16.3	1450
$\text{D}_3 - M^*$	1.10	0.01	0.88	14.6	2150
$\text{D}_4 - \Lambda_{\text{cool}}$	0.29	0	0.20	0.86	607

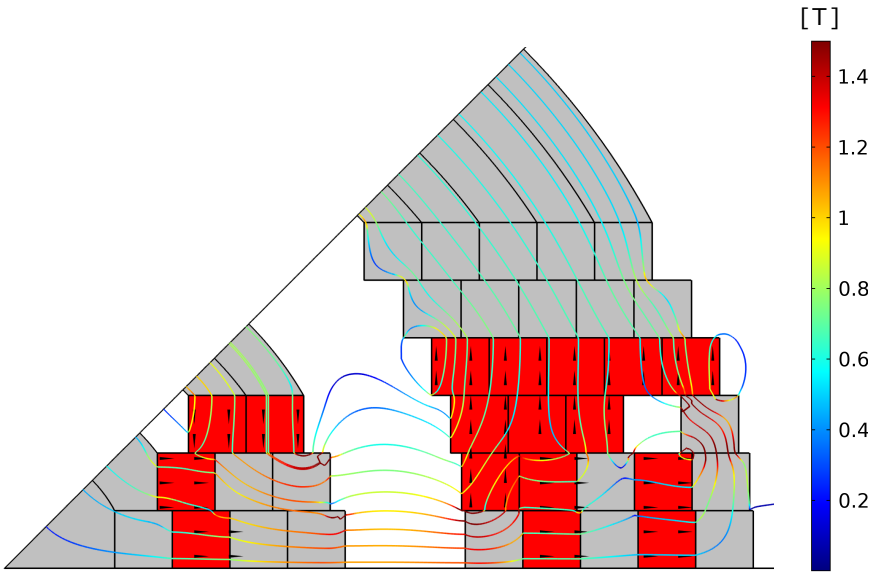

(a)

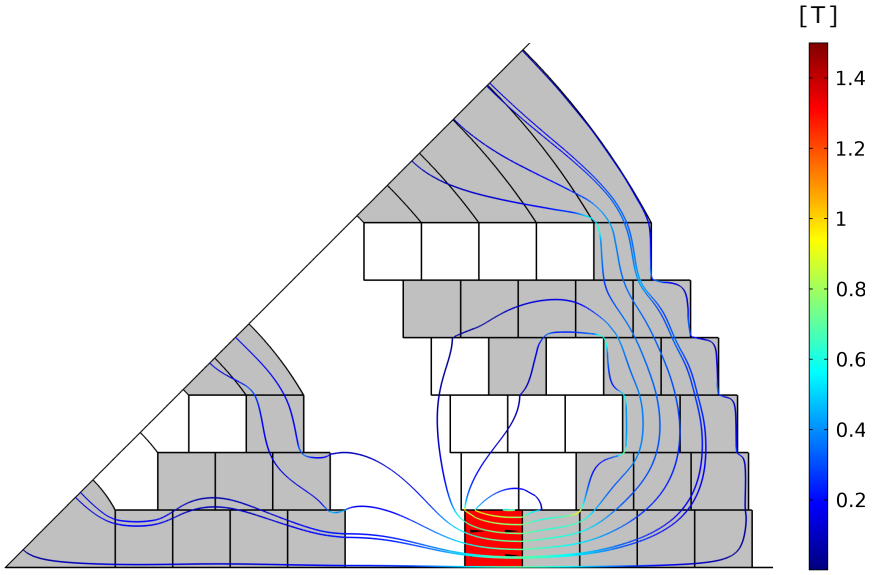

(b)

Figure 7.8: (a) M^* and (b) Λ_{cool} optimized magnet topologies.

Table 7.3: AMR results for three fitness functions.

	Q_{c} (kW)	W_{net} (kW)	η_{II}
D_1−HB	2.87	0.50	0.30
$\text{D}_2 - c_{\text{Q}}$	3.32	0.52	0.33
$\text{D}_3 - M^*$	3.23	0.52	0.32
$\text{D}_4 - \Lambda_{\text{cool}}$	0.09	0.08	0.06

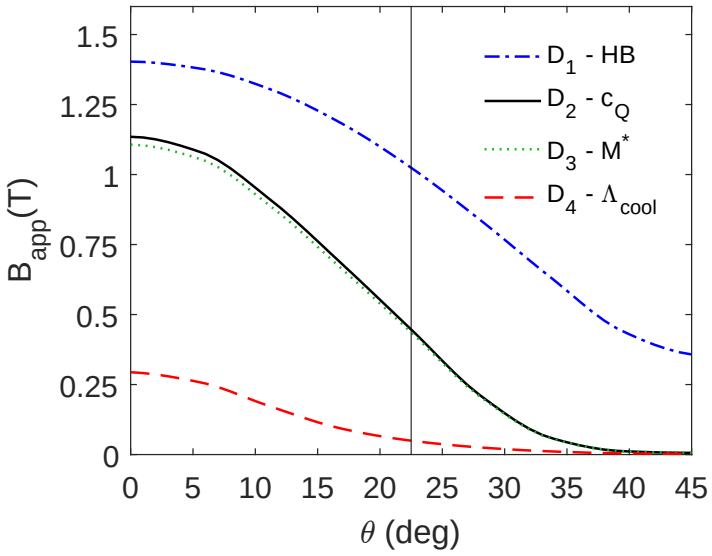

Figure 7.9: Magnetic field waveforms.

While the $\not\epsilon_{\mathrm{Q}}$ optimized circuit contains more magnet mass than the alternative metrics (D_3-D_4), it produces the greatest magnetic field variation ($\Delta B_{\mathrm{FWA}} = 0.9$ T), cooling power and second-law efficiency. This presents the ideal compromise of raw material investment, operating cost and cooling power with the added advantage that the $\not\epsilon_{\mathrm{Q}}$ optimized circuit can be manufactured with N42SH grade magnet material costing 10 \$/kg more than the base grade.

The three objective functions are shown in Table 7.4 along with the capital investment and net present value (NPV) of the operating costs. As described above, the NPV is evaluated with a discount rate of $i_{\mathrm{d}} = 5\%$ over ten years at a capacity factor of 0.35. As the metrics are evaluated with the flow weighted average field change (FWA), care must be taken when comparing the presented results with literature considering only the maximum field strength. Although the permanent magnet mass of 0.86 kg makes the Λ_{cool} optimized circuit appealing, the 0.2 T effective field change does not yield substantial cooling power. Even with reduced capital costs, the cost per unit cooling is significant. Costs are not presented for the M^* optimized refrigerator, given that the required magnet grade is not commercially available.

The $\not\epsilon_{\mathrm{Q}}$ optimized circuit aligns with expectations for magnetocaloric heat pumps: high initial investment with reduced lifetime operating costs. Consider an inexpensive, one-ton ($\dot{Q}_{\mathrm{C}}$=3.5 kW) air conditioner with an energy efficiency ratio (EER) of 11. The NPV of the devices electrical consumption is \$3,000 over the considered lifetime

of 10 years. While not a direct comparison, the operating cost alone exceeds the capital and operating cost of the $\not\epsilon_Q$ optimized magnetic refrigerator.

Table 7.4: Comparison of metrics. Refrigerant capital cost is \$84 for each metric.

	$\not\epsilon_Q$ (\$/kWh)	M^*	Λ_{cool}	Capital (\$)	Operating (\$)
D_1−HB	0.96	0.042	0.010	1990	1420
$D_2 - c_Q$	0.61	0.065	0.048	1010	1500
$D_3 - M^*$	**	0.070	0.053	**	1480
$D_4 - \Lambda_{cool}$	4.7	0.059	0.34	284	217

Fig. 7.10 illustrates how the optimized circuit would be implemented in a cooling device, where blue and red segments indicate magnet material in the main and flux focusing circuits, respectively. Streamlines of magnetic flux show the high and low field regions of the rotating regenerator wheel. To operate as an AMR, a pump-valve combination [56] or a piston-based system [61] would be paired with Fig. 7.10 to oscillate fluid in the regenerators.

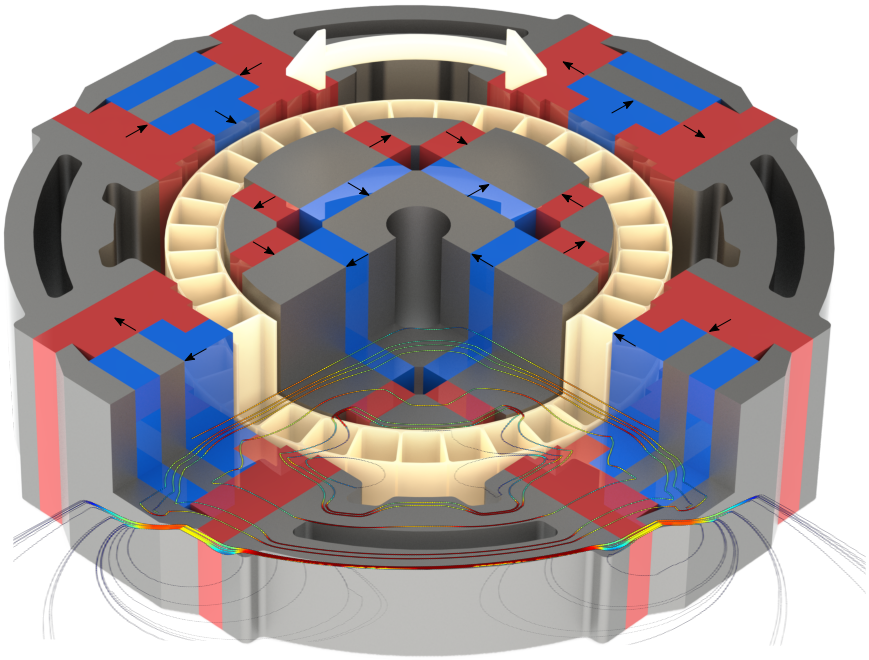

Figure 7.10: Example magnetic refrigerator with optimized magnet topology.

$\not\epsilon_Q$ has proven to be a valuable objective function, as a myriad of phenomena are related to cost. Using insights from the cost-minimizing quantity and distribution of permanent magnet material, future works will explore alternative discretizations of

Fig. 7.4, incorporate the effects of a finite-length magnet, extend the methodology to three-dimensions and explore a wider range of AMR operating parameters.

7.6 Conclusions

To improve the feasibility of a magnetic refrigeration device, a topology optimization is applied on a magnetic circuit to minimize the cost of cooling. For each magnet topology, capital and operating costs are evaluated from an AMR model and magnetic field simulation. A genetic algorithm breeds favorable designs to converge on a cost-minimized magnetic circuit.

The methodology produces a novel magnet design with the optimal distribution and amount of permanent magnet material. The effects of finite coercivity are shown to have a strong impact on the design feasibility and should be included for magnetic circuits with discrete remanence directions. A refrigerator with the optimized magnet topology is able to provide 3.3 kW of cooling power at a temperature span of 15 degrees, using 16.3 kg of permanent magnet material. The result is $0.61 per delivered kWh of exergetic cooling, an improvement over alternative magnet optimization metrics.

Acknowledgments

The support of the Natural Sciences and Engineering Research Council of Canada and BASF New Business is greatly appreciated. The authors would additionally like to thank Alexander Barcza (Vacuumschmelze GmbH & Co. KG) for assistance with permanent magnet pricing.

Chapter 8

Conclusions

The objective of this dissertation is to improve the performance and lifetime costs of active magnetic regenerators. To accomplish this, the active magnetic regenerator is presented as a device comprised of a (1) magnetocaloric regenerator, (2) a fluid flow system and a (3) magnetic field source. A combined experimental and numerical approach is employed to explore improvements at both the subsystem and device scale. This is illustrated in 8.1 below, where the contributions of each chapter are associated with an AMR subsystem or subsystems. The circle diameter corresponds to the relative importance, red text denotes increasing performance and blue text denotes decreasing cost.

Fluid flow waveforms, multilayering and operating parameter optimization are explored as the primary means to increase performance with acceptable cost. The dissertation first focuses on fluid flow systems (Chapter 2), where the impact of fluid flow waveforms on active magnetic regenerator performance is experimentally investigated. A parametric investigation of the regenerative blow duration with fixed utilization yields an 11.2 % increase in exergetic cooling power over the sinusoidal fluid flow waveform. Flow unbalance is shown to be detrimental to AMR performance, and is identified by the measured regenerator temperature distribution. It is hypothesized that numerous under-performing AMR devices in literature suffer from unbalanced flow effects.

The focus shifts to two-layered regenerators and AMR operating parameters (Chapter 3). A parametric investigation of the Curie temperature spacing reveals that while multilayering increases no-load temperature spans, the benefits decrease rapidly with applied load. Furthermore, the largest Curie temperature spacing does not produce the largest temperature span and, using interface temperature measurements, it was

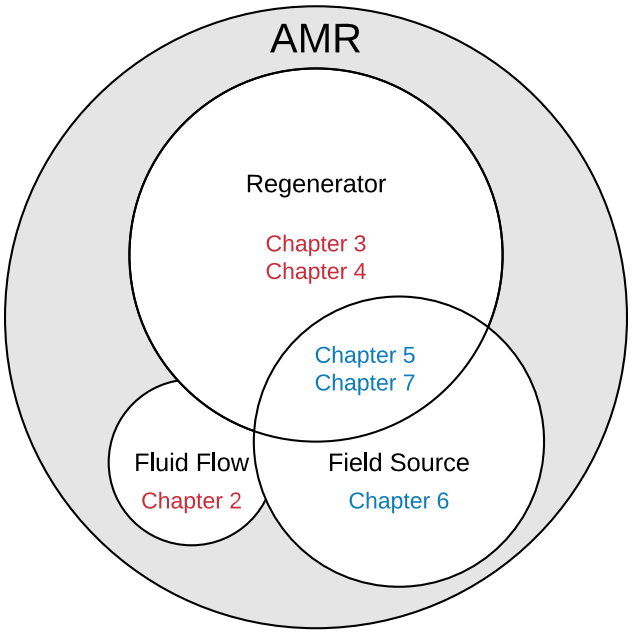

Figure 8.1: Relation between chapter contributions and AMR subsystems. Red and blue text denote objectives of increasing performance and decreasing cost, respectively.

shown that the warm layer fails to fully activate the cold layer. Finally, nonlinear temperature distributions are observed, and negative layer spans are measured while maintaining positive regenerator spans.

The results suggest that while multilayering can improve AMR performance without increasing cost, the large parameter space must be modeled in detail. This is considered in Chapter 4, where a highly efficient AMR modeling framework is presented and validated with the aforementioned experiments. The macroscopic device performance (temperature span, cooling power) and the regenerator temperature distribution is accurately predicted for a wide range of regenerator compositions, applied heat loads, displaced fluid volumes and heat rejection temperatures. Insights from the model are used to inform device modifications. Enabled by the models fast convergence time, an optimization is performed and a no-load temperature span of 40 K is measured in close proximity to the simulated optimum; one of the highest in literature. The modeling framework is shown to be effective in designing regenerator compositions for targeted applications.

To decrease costs, the magnetic field source and its interaction with the regenerator is explored. First, a superconducting magnetic field generator is investigated for cryogenic liquefaction applications (Chapter 5). Measurements reveal that regen-

erator forces can exceed a thousand pounds, even though the thermodynamic cycle work is small. To increase active magnetic regenerative liquefier efficiency and to minimize the magnet heating problem impeding large scale devices, the distribution of soft magnetic material is optimized and nearly ideal balancing characteristics are simulated.

Chapter 6 focuses on cost reductions by investigating the potential of reduced rare-earth permanent magnet materials. A topology optimization is formulated that considers demagnetization as an endogenous constraint. The optimized magnet topologies give insight on magnet designs for reduced cost, reduced rare-earth permanent magnet materials. Although inexpensive magnet designs are generated with ferrite for flux densities in the vicinity of 0.4 T, the required magnet volumes suggest Dy-free NdFeB may be an equitable compromise in the ongoing performance vs. material criticality debate. Furthermore, compared to magnet segments constrained to the radial and tangential directions, the maximum magnetic flux density is increased from 0.366 to 0.483 T by including the local remanence orientation as optimization design variables. While high energy-product, rare-earth-free permanent magnet materials are desired, this highlights the importance of permanent magnet manufacturing advances that enable optimized designs to be realized in commercial applications.

Finally, the regenerator and magnet design problems are coupled in a permanent magnet topology optimization to minimize the combined capital and operating costs of an AMR (Chapter 7). Square magnet shapes with discrete remanence orientations are chosen to facilitate the deconstruction and reclamation of permanent magnet materials. The optimization simultaneously produces the optimal magnetic field waveform and the optimal means of producing this waveform. The lifetime operating costs of the optimized AMR device are shown to be in the realm of existing entry-level cooling devices. Although inexpensive permanent magnet structures with low flux densities can be produced, the lifetime operating costs associated with the decreased operating efficiency are shown to be prohibitive.

8.1 Recommendations for future work

The following studies, presented as additions to the Chapter 7 framework, are recommended to further the pursuit of AMR devices with increased performance and reduced cost.

- Caloric materials are a significant and uncertain component of system cost. For this reason, a number of materials with first order transitions are of interest as they are comprised of low-cost, rare-earth free constituents. Future studies should replace the single material gadolinium regenerator with multilayered first order magnetocaloric materials, and include the regenerator composition in the optimization.

- The optimal magnet topology was found for a single regenerator geometry and temperature span. Future studies should include the regenerator length and thickness (i.e. gap between Halbach cylinders) as variables in the optimization, and explore the impact of temperature span on the optimal design and lifetime cost.

- Chapter 7 considers packed spherical particle beds, and the results indicate that the pump work is a significant component of the lifetime cost. Future studies should investigate regenerator matrix geometries (e.g. 3D printed micro-structures) to explore the impact of increased porosity on the combined capital and operating costs.

- The magnet optimization technique in Chapter 7 is robust and effective, however it is intrinsically naive and inefficient. Future studies should investigate how to couple the magnet optimization methodologies developed by Insinga *et al.* [43] or Lee *et al.* [39] with the cost optimization framework of Chapter 7.

- Permanent magnets have yet to produce the flux densities required for high-efficiency liquefaction applications. Future studies should extend the methodology to superconducting magnets with temperature spans pertaining to cryogen liquefaction.

- Although the methodology in Chapter 7 is enabled by efficient AMR modelling tools, the semi-analytic AMR model reduces the spatially varying field waveform to average high and low field values. Future works should implement a 1-D numerical AMR model (such as in Chapter 3) to improve the treatment of the magnetic field waveform.

The following will enable these investigations:

- The AMR model must be validated with experiments before implementing first order materials in the methodology of Chapter 7.
- More computational resources are required to increase the optimization design space. The evolutionary optimization algorithm can be spread across many cores in a clustered computing facility. If this is pursued, it is recommended that the COMSOL Multiphysics permanent magnet simulation is replaced with an open source finite-element solver (FEniCS, Elmer).

Appendix A

List of publications

A comprehensive list of publications can be found on Google Scholar or ResearchGate.

First-authored journal papers

1. Experimental Performance Investigation of an Active Magnetic Regenerator Subject to Different Fluid Flow Waveforms, International Journal of Refrigeration 74 (2017), 38-46. (http://doi.org/10.1016/j.ijrefrig.2016.10.001)

2. Performance evaluation of two-layer active magnetic regenerators with second-order magnetocaloric materials, Applied Thermal Engineering 106 (2016), 405-414. (http://doi.org/10.1016/j.applthermaleng.2016.06.029)

3. Semi-analytic AMR element model, Applied Thermal Engineering 128 (2018), 1022-1029. (http://doi.org/10.1016/j.applthermaleng.2017.09.082)

4. Passive force balancing of an Active Magnetic Regenerative Liquefier, Journal of Magnetism and Magnetic Materials 451 (2018), 79-86. (http://doi.org/10.1016/j.jmmm.2017.11.002)

5. Topology optimization of reduced rare-earth permanent magnet arrays with finite coercivity, Journal of Applied Physics 123 (2018) 193903. (https://doi.org/10.1063/1.5026862)

6. Permanent Magnet Design for Magnetic Heat Pumps using Total Cost Minimization, Journal of Magnetism and Magnetic Materials 442 (2017), 87-96. (http://doi.org/10.1016/j.jmmm.2017.06.039)

Co-authored journal papers

7. Magnetic heat pumps: An overview of design principles and challenges, Science and Technology for the Built Environment 22 (2016), 507-519. (http://doi.org/10.1080/23744731.2016.1171632)

8. Impacts of configuration losses on active magnetic regenerator device performance, Applied Thermal Engineering 106 (2016), 601-612. (http://doi.org/10.1016/j.applthermaleng.2016.06.039)

9. Material screening metrics and optimal performance of an active magnetic regenerator, Journal of Applied Physics 121 (2017), 064902. (http://doi.org/10.1063/1.4975833)

10. A concise approach for building the S-T diagram for Mn-Fe-P-Si hysteretic magnetocaloric material, Journal of Physics D: Applied Physics 50 (2017) 365001 (http://doi.org/10.1088/1361-6463/aa7bcd)

11. Experimental investigation of $MnFeP_{1-x}As_x$ multilayer active magnetic regenerators, Journal of Physics D: Applied Physics 50 (2017) 315001. (http://doi.org/10.1088/1361-6463/aa7a33)

12. Experimental study of 2-layer regenerators using Mn-Fe-Si-P materials, Journal of Physics D: Applied Physics 50 (2017) 105002. (http://doi.org/10.1088/1361-6463/aaaba7)

13. Multiple points of equilibrium for active magnetic regenerators using first order magnetocaloric material, Journal of Applied Physics 123 (2018) 204901. (https://doi.org/10.1063/1.5026633)

14. Investigation of bypass fluid flow in an Active Magnetic Regenerative Liquefier, Cryogenics 93 (2018) 34-40. (https://doi.org/10.1016/j.cryogenics.2018.05.010)

First-authored conference papers

15. Heat exchanger design for heat flux measurement in Thermag 6 (2014), Victoria, Canada.

16. Investigation of an active magnetic regenerator subject to different fluid flow waveforms in Thermag 7 (2017), Turin, Italy.

17. Experimental evaluation of two-material active magnetic regenerators in Thermag 7 (2017), Turin, Italy.

18. Permanent magnet design for magnetic heat pumps using total cost minimization: initial implementation in ECOS (2017), San Diego, United States.

Appendix B

Material properties

Although the discovery, synthesis and characterization of low-cost, high-performing magnetocaloric materials is imperative, the present dissertation decouples the *device* problem from the *material* problem by focusing entirely on second-order (i.e. gadolinium-like) magnetocaloric materials with molecular mean field theory (MFT) generated properties. The MFT model used here is described in the masters thesis of Oliver Campbell [3]. The field and temperature dependent adiabatic temperature change, specific heat and specific magnetization are shown in Fig. B.1.

Section 1.1 above outlines how the entropy change and adiabatic temperature change are obtained from magnetization data. MFT simplifies the magnetization to the average value of a non-interacting spin system as a function of field and temperature [12]:

$$M(T,H) = N_s g J \mu_B B_J(\alpha) \tag{B.1}$$

where N_s is the number of spins per unit mass, g is the Lande factor, J is the total angular momentum, μ_B is the Bohr magneton and $B_J(\alpha)$ is the Brillouin function.

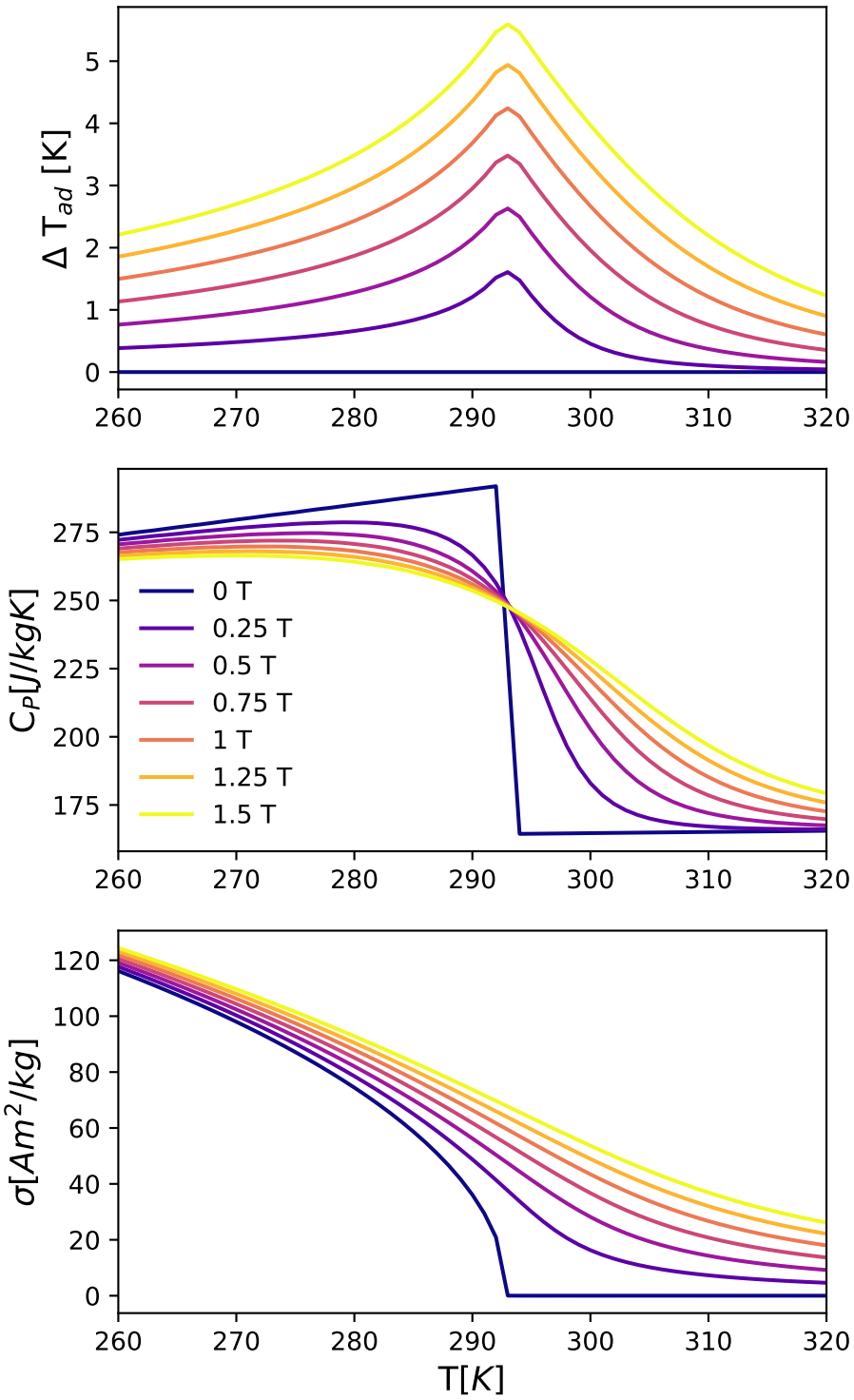

Figure B.1: Adiabatic temperature change, specific heat and specific magnetization as a function of temperature and applied field ($\mu_0 H = 0, 0.25, 0.5, 0.75, 1, 1.25$ and 1.5 T) produced with molecular mean field theory (MFT) [3].

Appendix C

Numerical Halbach simulation

In the work above, COMSOL Multiphysics was used to evaluate magnetic fields. Here, a numerical solution to the dipolar Halbach array is presented. In a theoretical Halbach array [28, 74, 22], the remanence (e.g. permanent magnet orientation) continuously varies as:

$$< B_{rem,r}, B_{rem,\theta} >= ||B_{rem}|| < cos(p\theta), sin(p\theta) > \tag{C.1}$$

where $2p$ is the number of poles, $||B_{\text{rem}}||$ is the magnitude of the remanence, r and θ are the polar coordinate axis. The distribution of remanence with p=1 is shown in Fig. C.1 below.

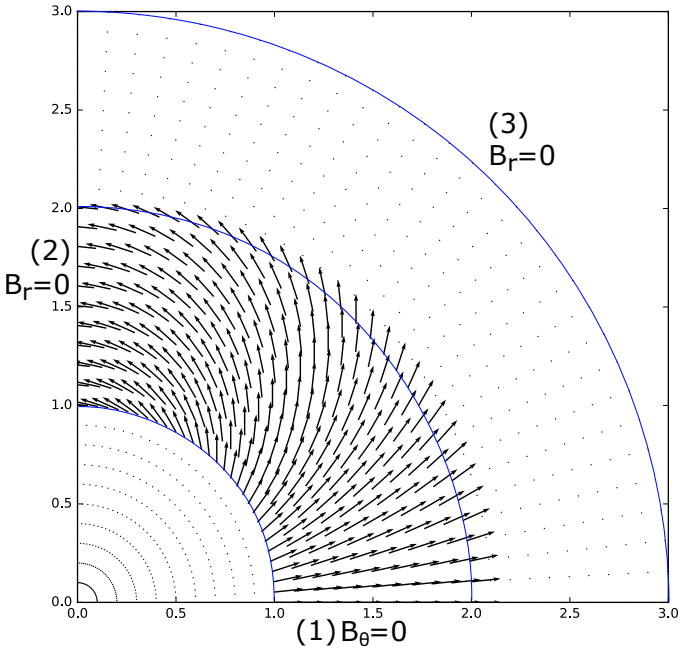

Figure C.1: Computational domain for Halbach array with p=1. Blue lines denote geometry: inner air bore, permanent magnet and outer air. Boundaries denoted by (1), (2) and (3) refer to the bottom, left and outer boundaries, respectively, with conditions (1) $B_\theta = 0$, (2) $B_r = 0$, (3) $B_r = 0$.

Bjørk *et al.* (2010) [32] analytically solved the governing partial differential equation using a Fourier series solution for the simplifying case of constant permeability ($\mu_r = 1$). For the case of a constant permeability and p=1, the distribution of radial (B_r) and tangential (B_θ) flux density inside the magnet bore (region I) and inside the permanent magnet material (region II) are given as:

$$
\begin{aligned}
B_r^I &= B_{rem} ln\Big(\frac{R_o}{R_i}\Big) cos(\theta) \\
B_\theta^I &= -B_{rem} ln\Big(\frac{R_o}{R_i}\Big) sin(\theta) \\
B_r^{II} &= B_{rem} ln\Big(\frac{R_o}{r}\Big) cos(\theta) \\
B_\theta^{II} &= -B_{rem}\Big(ln\Big(\frac{R_o}{r}\Big) - 1\Big) sin(\theta)
\end{aligned}
\tag{C.2}
$$

C.1 Mathematical Formulation

For magnetostatics, Maxwell's equations reduce to:

$$\nabla \times \vec{H} = 0 \tag{C.3}$$

$$\nabla \cdot \vec{B} = 0 \tag{C.4}$$

which implies that the magnetic field is irrotational. As such, a scalar potential function must exist such that:

$$\vec{H} = -\nabla \vec{V}_M \tag{C.5}$$

where $\vec{V}_M$ is the magnetic scalar potential. In a 2-D domain, the magnetic scalar potential takes the form:

$$\vec{V}_M =< 0, 0, V_M > \tag{C.6}$$

The constitutive relation for magnetic materials is:

$$\vec{B} = \mu \vec{H} + \vec{B}_{rem} \tag{C.7}$$

where $\vec{B}_{rem}$ is the remanence vector or local permanent magnet orientation and $\mu = 4\pi 10^{-7}$ is the permeability of free space. Combining Eq. C.7 with Eq. C.4 yields the governing equation:

$$\nabla \cdot (\mu \nabla V_M - \vec{B}_{rem}) = 0 \tag{C.8}$$

In polar coordinates, the gradient and divergence are:

$$\nabla V_M =< \frac{\partial V_M}{\partial r}, \frac{1}{r}\frac{\partial V_M}{\partial \theta} > \tag{C.9}$$

$$\nabla \cdot \vec{f} = \frac{f_r}{r} + \frac{\partial f_r}{\partial r} + \frac{1}{r}\frac{\partial f_\theta}{\partial \theta} \tag{C.10}$$

Expanding the gradient in the governing equation (Eq. C.8) yields

$$\nabla \cdot \Big(\begin{bmatrix} \mu \frac{\partial V_M}{\partial r} - B_{rem,r} \\ \frac{\mu}{r}\frac{\partial V_M}{\partial \theta} - B_{rem,\theta} \end{bmatrix} \Big) = \begin{bmatrix} 0 \\ 0 \end{bmatrix} \tag{C.11}$$

and evaluating the divergence yields:

$$\frac{\mu \frac{\partial V_M}{\partial r} - B_{rem,r}}{r} + \frac{\partial}{\partial r}\Big(\mu \frac{\partial V_M}{\partial r} - B_{rem,r}\Big) + \frac{1}{r}\frac{\partial}{\partial \theta}\Big(\frac{\mu}{r}\frac{\partial V_M}{\partial \theta} - B_{rem,\theta}\Big) = 0 \tag{C.12}$$

Applying a chain rule (μ_r and $\vec{B}_{rem}$ can be spatially dependent) yields:

$$\mu \frac{\partial^2 V}{\partial r^2} + \frac{\mu}{r^2}\frac{\partial^2 V}{\partial \theta^2} + \frac{\partial V}{\partial r}\Big(\frac{\mu}{r} + \frac{\partial \mu}{\partial r}\Big) + \frac{1}{r^2}\frac{\partial V}{\partial \theta}\frac{\partial \mu}{\partial \theta} = \frac{1}{r}\Big(B_{r,r} + \frac{\partial B_{r,r}}{\partial r} + \frac{\partial B_{r,\theta}}{\partial \theta}\Big) \tag{C.13}$$

where $B_{rem,r}$, $B_{rem,\theta}$ have been written as $B_{r,r}$, $B_{r,\theta}$ for brevity. Once the solution V is known, the magnetic flux density is post-calculated as ($\vec{B} = \vec{B}_{rem} - \mu \nabla V$):

$$\begin{aligned} B_r &= B_{r,r} - \mu \frac{\partial V}{\partial r} \\ B_\theta &= B_{r,\theta} - \frac{\mu}{r}\frac{\partial V}{\partial \theta} \end{aligned} \tag{C.14}$$

C.2 Boundary Conditions

Boundary conditions are imposed to ensure conservation of magnetic flux lines ($\vec{n} \cdot \vec{B} = 0$). This implies that the vector $\vec{B}$ is tangent to all boundaries as shown in Fig. C.1, except at the left anti-symmetric boundary (2) where the vector $\vec{B}$ is *perpendicular*. Along the bottom boundary (1), $B_\theta = 0$. The constitutive relation of Eq. C.7 with the definition of the magnetic scalar potential yields $B_\theta = 0 = B_{r,\theta} - \mu(\frac{\partial V}{\partial \theta})/r$. As the remanence $B_{r,\theta} = 0$ is zero along boundary (1), the Neumann boundary condition is:

$$\frac{\partial V}{\partial \theta} = 0|_{(1)} \tag{C.15}$$

Along the left boundary (2), $B_r = 0$ which indicates that $\frac{\partial V}{\partial r} = 0$. This is satisfied with the simple Dirichlet condition $V = 1$.

$$V = 1|_{(2)} \tag{C.16}$$

Along the outer boundary (3), $B_r = 0$ yielding the Neumann boundary condition:

$$\frac{\partial V}{\partial r} = 0|_{(3)} \tag{C.17}$$

C.3 Discretization

Eq. C.13 is solved using finite differences. A uniform grid is considered where the spacing $\Delta\theta$ is independent from Δr to allow a finer grid in the radial direction where a discontinuity exists in the remanence (boundaries between air and magnet). Each of the terms in Eq. C.13 above are discretized as follows, where subscripts i and j refer to r and θ, respectively:

$$\mu\frac{\partial^2 V}{\partial r^2} = \frac{\mu_{i,j}}{\Delta r^2}\Big(V_{i+1,j} - 2V_{i,j} + V_{i-1,j}\Big) + O(\Delta r^2) \tag{C.18}$$

$$\frac{\mu}{r^2}\frac{\partial^2 V}{\partial \theta^2} = \frac{\mu_{i,j}}{r_i^2\Delta\theta^2}\Big(V_{i,j+1} - 2V_{i,j} + V_{i,j-1}\Big) + O(\Delta\theta^2) \tag{C.19}$$

Using centered differences for first derivatives:

$$\frac{\partial V}{\partial r}\Big(\frac{\mu}{r} + \frac{\partial \mu}{\partial r}\Big) = \Big(\frac{V_{i+1,j} - V_{i-1,j}}{2\Delta r}\Big)\Big(\frac{\mu_{i,j}}{r_i} + \frac{\mu_{i+1,j} - \mu_{i-1,j}}{2\Delta r}\Big) + O(\Delta r^2) \tag{C.20}$$

$$\frac{1}{r^2}\frac{\partial V}{\partial \theta}\frac{\partial \mu}{\partial \theta} = \frac{1}{r_i^2}\Big(\frac{V_{i,j+1} - V_{i,j-1}}{2\Delta\theta}\Big)\Big(\frac{\mu_{i,j+1} - \mu_{i,j-1}}{2\Delta\theta}\Big) + O(\Delta\theta^2) \tag{C.21}$$

Since the remanence is defined *a priori*, the following can be grouped into a bulk term ($P_{i,j}$) that is calculated before the numerical solution:

$$\begin{aligned} \frac{1}{r}\Big(B_{r,r} + r\frac{\partial B_{r,r}}{\partial r} + \frac{\partial B_{r,\theta}}{\partial \theta}\Big) = P_{i,j} = ... \\ ...\frac{1}{r_i}\Big(B_{i,j}^{r,r} + \frac{r_i}{2\Delta r}(B_{i+1,j}^{r,r} - B_{i-1,j}^{r,r}) + \frac{1}{2\Delta\theta}(B_{i,j+1}^{r,\theta} - B_{i,j-1}^{r,\theta})\Big)... \\ ... + O(\Delta\theta^2) + O(\Delta r^2) \end{aligned} \tag{C.22}$$

Substituting these discretized formulas into the governing equation (Eq. C.13) yields the lengthy expression for the update term $V_{i,j}$:

$$\begin{aligned} V_{i,j} = \Big[&\frac{\mu_{i,j}}{\Delta r^2}\big(V_{i+1,j} + V_{i-1,j}\big) + \frac{\mu_{i,j}}{r_i^2 \Delta\theta^2}\big(V_{i,j+1} + V_{i,j-1}\big) + ... \\ &... + \big(\frac{\mu_{i+1,j} - \mu_{i-1,j}}{2\Delta r} + \frac{\mu_{i,j}}{r_i}\big)\big(\frac{V_{i+1,j} - V_{i-1,j}}{2\Delta r}\big) + ... \\ &... + \big(\frac{1}{4r_i^2\Delta\theta^2}\big)\big(\mu_{i,j+1} - \mu_{i,j-1}\big)\big(V_{i,j+1} - V_{i,j-1}\big) - P_{i,j}\Big] ... \\ &... \Big(\frac{2\mu_{i,j}}{\Delta r^2} + \frac{2\mu_{i,j}}{r_i^2\Delta\theta^2}\Big)^{-1} \\ &... + O(\Delta\theta^2) + O(\Delta r^2) \end{aligned} \tag{C.23}$$

Boundary conditions are directly enforced in Eq. C.23 above. Along the bottom boundary (1), $\frac{\partial V}{\partial \theta} = 0$ which indicates that $V_{i,j+1} = V_{i,j-1}$. Along the left boundary (2), $V = 1$ and along the outer boundary (3), $V_{i+1,j} = V_{i-1,j}$.

As with all cylindrical coordinate systems, a singularity exists at $r = 0$. While possible treatments involve the use of L'hopital's rule at the origin or forcing a nonzero radius ($r(0) = \epsilon$), in the present work the origin is treated as an axisymmetric line ($V = 1$, as with boundary (2) in Fig. C.1 above). B_r and B_θ are then post-calculated as the mean of the neighboring elements.

C.4 Algorithm Description

An iterative finite difference scheme is used to solve the governing partial differential equation. Given some initial guess V^0, an improved solution is obtained by solving Eq. C.24 at each mesh point in the domain:

$$\begin{aligned} V_{i,j}^1 = \Big[&\frac{\mu_{i,j}}{\Delta r^2}\big(V_{i+1,j}^0 + V_{i-1,j}^0\big) + \frac{\mu_{i,j}}{r_i^2 \Delta\theta^2}\big(V_{i,j+1}^0 + V_{i,j-1}^0\big) + ... \\ &... + \big(\frac{\mu_{i+1,j} - \mu_{i-1,j}}{2\Delta r} + \frac{\mu_{i,j}}{r_i}\big)\big(\frac{V_{i+1,j}^0 - V_{i-1,j}^0}{2\Delta r}\big) + ... \\ &... + \big(\frac{1}{4r_i^2\Delta\theta^2}\big)\big(\mu_{i,j+1} - \mu_{i,j-1}\big)\big(V_{i,j+1}^0 - V_{i,j-1}^0\big) - P_{i,j}\Big] ... \\ &... \Big(\frac{2\mu_{i,j}}{\Delta r^2} + \frac{2\mu_{i,j}}{r_i^2\Delta\theta^2}\Big)^{-1} \end{aligned} \tag{C.24}$$

This is repeated until the following criterion is satisfied:

$$e = \max_{i,j} |V^1 - V^0| < 10^{-6} \tag{C.25}$$

C.5 Results

The numerical solution of V is shown below in Fig. C.2 for $n_r = 200$ nodes, $n_\theta = 100$ nodes, $R_i = 0.5$, $R_o = 2$, $||B_{rem}|| = 1.3$ (corresponding to N42 grade NdFeB permanent magnet) and $\mu_r = 1$.

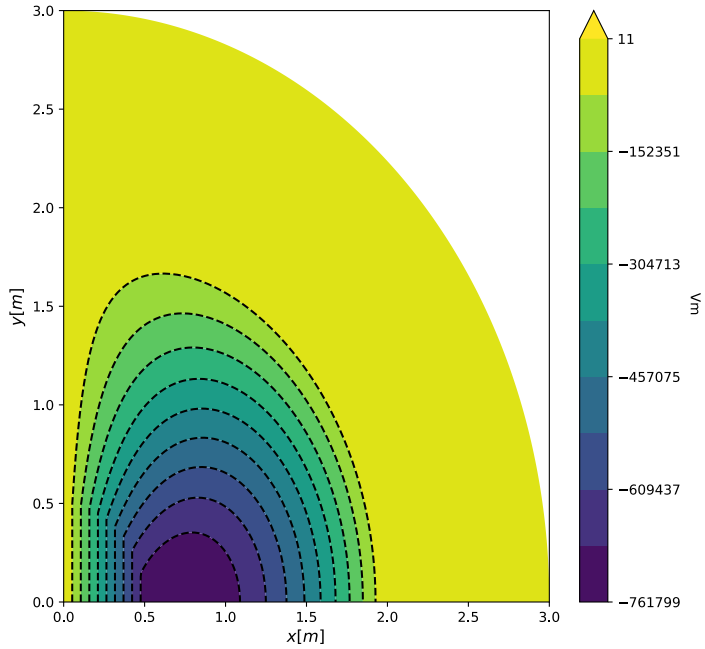

Figure C.2: Distribution of magnetic vector potential (V) from numerical solution.

The magnitude of the flux density (i.e. $||B||_2 = \sqrt{B_r^2 + B_\theta^2}$) is shown below in Fig. C.3 (a) and the corresponding analytic solution using Eq. C.2 is shown in Fig. C.3 (b). Both numerical and analytic solutions indicate a homogenous high-field region inside the cylinder bore with a flux density near 1.8 T. The distribution of $||B||_2$ is more sophisticated inside the permanent magnet material (e.g. $0.5 < r < 2$), however the numerical and analytic solutions are in good agreement. Outside of the Halbach cylinder, the magnetic flux density drops to 0.

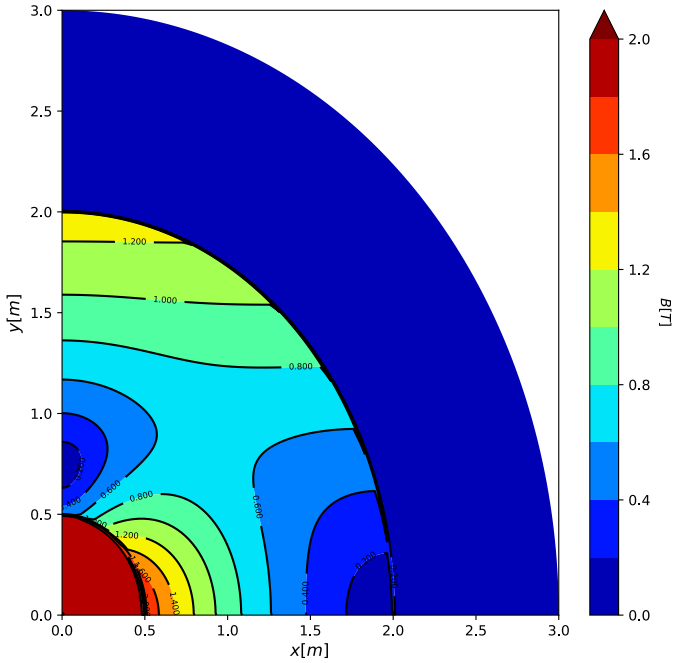

(a)

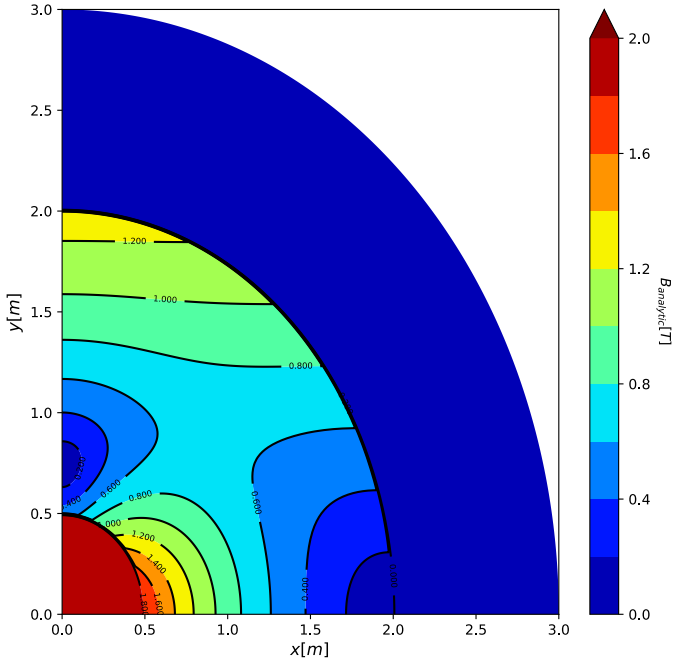

(b)

Figure C.3: (a) Distribution of magnetic flux density post-calculated from numerical solution of magnetic vector potential. (b) Analytic solution.

Bibliography

[1] R. Teyber, P. V. Trevizoli, T. V. Christiaanse, P. Govindappa, I. Niknia, A. Rowe, Performance evaluation of two-layer active magnetic regenerators with second-order magnetocaloric materials, Applied Thermal Engineering 106 (2016) 405–414.

[2] Demagnetization (BH) curves for neodymium magnets, https://www.kjmagnetics.com/bhcurves.asp.

[3] O. Campbell, Investigation of calculated adiabatic temperature change of Mn-FePAs alloys, Master's thesis, University of Victoria (2015).

[4] EIA, How is electricity used in u.s. homes?, Tech. rep., U.S. Energy Information Administration (2014).
URL https://www.eia.gov/tools/faqs/faq.php?id=96&t=3

[5] K. Nawaz, B. Shen, A. Elatar, V. Baxter, O. Abdelaziz, R290 (propane) and R600a (isobutane) as natural refrigerants for residential heat pump water heaters, Applied Thermal Engineering 127 (2017) 870–883.

[6] N. N. A. Bakar, M. Y. Hassan, H. Abdullah, H. A. Rhman, M. P. Abdullah, F. Hussin, M. Bandi, Energy efficiency index as an indicator for measuring building energy performance: A review, Renewable and Sustainable Energy Reviews 44 (2015) 1–11.

[7] J. M. Calm, The next generation of refrigerants - Historical review, considerations, and outlook, International Journal of Refrigeration 31 (2008) 1123–1133.

[8] A. Mota-Babiloni, J. Navarro-Esbrí, Á. Barragán-Cervera, F. Molés, B. Peris, Analysis based on EU Regulation No 517/2014 of new HFC/HFO mixtures as alternatives of high GWP refrigerants in refrigeration and HVAC systems, International Journal of Refrigeration 52 (2015) 21–31.

[9] B. Palm, Hydrocarbons as refrigerants in small heat pump and refrigeration systems - A review, International Journal of Refrigeration 31 (2008) 552–563.

[10] C. Zilio, J. S. Brown, G. Schiochet, A. Cavallini, The refrigerant R1234yf in air conditioning systems, Energy 36 (2011) 6110–6120.

[11] V. K. Pecharsky, K. A. Gschneidner, Jr., Advanced magnetocaloric materials: What does the future hold?, International Journal of Refrigeration 29 (2006) 1239–1249.

[12] A. Smith, C. R. H. Bahl, R. Bjørk, , K. Engelbrecht, K. K. N. N. Pryds, Materials challenges for high performance magnetocaloric refrigeration devices, Advanced Energy Materials 2 (2012) 1288–1318.

[13] A. Kitanovski, J. Tusek, U. Tomc, U. Plaznik, M. Ozbolt, A. Poredos, Magnetocaloric Energy Conversion: From Theory to Applications, Springer International Publishing, 2015.

[14] M. Balli, S. Jandl, P. Fournier, A. Kedous-Lebouc, Advanced materials for magnetic cooling: Fundamentals and practical aspects, Applied Physics Reviews 4 (2017) 021305.

[15] C. R. H. Bahl, K. K. Nielsen, The effect of demagnetization on the magnetocaloric properties of gadolinium, Journal of Applied Physics 105 (2009) 013916(1–5).

[16] J. A. Barclay, W. A. Steyert, Active magnetic regenerator. US-Patent 4332135. (1982).

[17] P. V. Trevizoli, T. V. Christiaanse, P. Govindappa, I. Niknia, R. Teyber, J. R. Barbosa Jr., A. Rowe, Magnetic heat pumps: an overview of design principles and challenges, Science and Technology for the Built Environment 22 (2016) 507–519.

[18] K. K. Nielsen, C. R. H. Bahl, A. Smith, R. Bjørk, N. Pryds, J. Hattel, Detailed numerical modeling of a linear parallel-plate active magnetic regenerator, International Journal of Refrigeration 32 (2009) 1478–1486.

[19] A. Tura, K. K. Nielsen, A. Rowe, Experimental and modeling results of a parallel-based active magnetic regenerator, International Journal of Refrigeration 35 (2012) 1518–1527.

[20] T. Lei, K. Engelbrecht, K. K. Nielsen, C. T. Veje, Study of geometries of active magnetic regenerators for room temperature magnetocaloric refrigeration, Applied Thermal Engineering 111 (2017) 1232–1243.

[21] P. V. Trevizoli, A. T. Nakashima, G. F. Peixer, J. R. Barbosa, Performance assessment of different porous matrix geometries for active magnetic regenerators, Applied Energy 187 (2017) 847–861.

[22] R. Teyber, P. V. Trevizoli, T. V. Christiaanse, P. Govindappa, I. Niknia, A. Rowe, Permanent magnet design for magnetic heat pumps using total cost minimization, Journal of Magnetism and Magnetic Materials 442 (2017) 87–96.

[23] S. Jacobs, J. Auringer, A. Boeder, J. Chell, L. Komorowski, J. Leonard, S. Russek, C. Zimm, The performance of a large-scale rotary magnetic refrigerator, International Journal of Refrigeration 37 (2014) 84–91.

[24] D. Eriksen, K. Engelbrecht, C. R. H. Bahl, R. Bjørk, Exploring the efficiency potential for an active magnetic regenerator, Science and Technology for the Built Environment 22 (5) (2016) 527–533.

[25] P. V. Trevizoli, J. R. Barbosa, Jr., Entropy generation minimization analysis of oscillating-flow regenerators, International Journal of Heat and Mass Transfer 87 (2015) 347–358.

[26] T. Burdyny, A. Rowe, Simplified modeling of active magnetic regenerators, International Journal of Refrigeration 36 (2013) 932–940.

[27] P. V. Trevizoli, Development of thermal regenerators for magnetic cooling applications, Ph.D. thesis, Federal University of Santa Catarina (2015).

[28] K. Halbach, Design of permanent multipole magnets with oriented rare earth cobalt material, Nuclear Instruments and Methods 169 (1980) 1–10.

[29] J. M. D. Coey, Permanent magnet applications, Journal of Magnetism and Magnetic Materials 248 (2002) 441–456.

[30] R. Bjørk, C. R. H. Bahl, A. Smith, N. Pryds, Review and comparison of magnet designs for magnetic refrigeration, International Journal of Refrigeration 33 (2010) 437–448.

[31] R. Bjørk, C. R. H. Bahl, A. Smith, N. Pryds, Comparison of adjustable permanent magnetic field sources, Journal of Magnetism and Magnetic Materials 322 (2010) 3664–3671.

[32] R. Bjørk, A. Smith, C. R. H. Bahl, Analysis of the magnetic field, force and torque for two-dimensional Halbach cylinders, Journal of Magnetism and Magnetic Materials 322 (2010) 133–141.

[33] H. A. Leupold, G. F. McLane, Fabrication of multipolar magnetic field sources, Journal of Applied Physics 76 (1994) 6253.

[34] H. A. Leupold, A. Tilak, E. P. Ii, Permanent magnet spheres : Design , construction , and application, Journal of Applied Physics 87 (2000) 4730.

[35] J. S. Choi, J. Yoo, Design of a Halbach magnet array based on optimization techniques, IEEE Transactions on Magnetics 44 (10) (2008) 2361–2366.

[36] J. S. Choi, J. Yoo, Simultaneous structural topology optimization of electromagnetic sources and ferromagnetic materials, Computer Methods in Applied Mechanics and Engineering 198 (2009) 2111–2121.

[37] S. Cheng, D. P. Arnold, Optimization of permanent magnet assemblies using genetic algorithms, IEEE Transactions on Magnetics 47 (10) (2011) 4104–4107.

[38] J. Lee, T. Nomura, E. M. Dede, Topology optimization of Halbach magnet arrays using isoparametric projection, Journal of Magnetism and Magnetic Materials 432 (2017) 140–153.

[39] J. Lee, M. Yoon, T. Nomura, E. M. Dede, Topology optimization for design of segmented permanent magnet arrays with ferromagnetic materials, Journal of Magnetism and Magnetic Materials 449 (2018) 571–581.

[40] A. R. Insinga, R. Bjørk, A. Smith, C. R. Bahl, Globally Optimal Segmentation of Permanent-Magnet Systems, Applied Physical Review 5 (064014).

[41] R. Bjørk, C. R. H. Bahl, A. R. Insinga, Topology optimized permanent magnet systems, Journal of Magnetism and Magnetic Materials 437 (2017) 78–85.

[42] R. Bjørk, Designing a magnet for magnetic refrigeration, Ph.D. thesis, Risoe DTU (2010).

[43] A. R. Insinga, Optimising magnetostatic assemblies, Ph.D. thesis, Technical University of Denmark (2016).

[44] D. S. Arnold, A. Tura, A. Rowe, Experimental analysis of a two-material active magnetic regenerator, International Journal of Refrigeration 34 (2011) 178–191.

[45] Y. Kim, I. Park, S. Jeong, Experimental investigation of two-stage active magnetic regenerative refrigerator operating between 77 K and 20 K, Cryogenics 57 (2013) 113–121.

[46] J. Holladay, K. Meinhardt, E. Polikarpov, E. Thomsen, J. Barclay, J. Cui, I. Anderson, B. Jensen, MagnetoCaloric Hydrogen Liquefaction, DOE Annual Merit Review (2017) (PD131).

[47] H. Maeda, Y. Yanagisawa, Recent developments in high-temperature superconducting magnet technology (review), IEEE Transactions on Applied Superconductivity 24 (3) (2014) 4602412.

[48] Y. Zhang, Progress in production and performance of second generation (2G) hts wire for practical applications, IEEE Transactions on Applied Superconductivity 24 (5) (2014) 7500405.

[49] I. Park, C. Lee, J. Park, S. Kim, S. Jeong, Ramping Operation of the Conduction-Cooled High-Temperature Superconducting Magnet for an Active Magnetic Regenerator System, IEEE Transactions on Applied Superconductivity 26 (4) (2016) 4600505.

[50] I. Park, S. Jeong, Development of the active magnetic regenerative refrigerator operating between 77 K and 20 K with the conduction cooled high temperature superconducting magnet, Cryogenics 88 (2017) 106–115.

[51] I. Park, C. Lee, J. Park, S. Kim, S. Jeong, Performance of the Fast-Ramping High Temperature Superconducting Magnet System for an Active Magnetic

Regenerator, IEEE Transactions on Applied Superconductivity 27 (4) (2017) 4601105.

[52] D. S. Arnold, A. Tura, A. Ruebsaat-Trott, A. Rowe, Design improvements of a permanent magnet active magnetic refrigerator, International Journal of Refrigeration 37 (2014) 99–105.

[53] P. V. Trevizoli, A. T. Nakashima, G. F. Peixer, J. R. Barbosa, Performance evaluation of an active magnetic regenerator for cooling applications-part i: Experimental analysis and thermodynamic performance, International Journal of Refrigeration 72 (2016) 192–205.

[54] C. Zimm, A. Boeder, J. Chell, A. Sternberg, A. Fujita, S. Fujieda, K. Fukamichi, Design and performance of a permanent-magnet rotary refrigerator, International Journal of Refrigeration 29 (2006) 1302–1306.

[55] T. Okamura, K. Yamada, N. Hirano, S. Nagaya, Performance of a room-temperature rotary magnetic refrigerator, International Journal of Refrigeration 29 (2006) 1327–1331.

[56] K. Engelbrecht, D. Eriksen, C. R. H. Bahl, R. Bjrk, J. Geyti, J. A. Lozano, K. K. Nielsen, F. Saxild, A. Smith, N. Pryds, Experimental results for a novel rotary active magnetic regenerator, International Journal of Refrigeration 35 (2012) 1498–1505.

[57] Y. Miyazaki, H. Hasegawa, K. Nagashima, N. Hirano, S. Bae, H. Takata, T. Okamura, Y. Noguchi, H. Wada, T. Kawana, Characterization of a kW class magnetic refrigerator, in: Proceedings in the 6th International Conference on Magnetic Refrigeration at Room Temperature, Victoria, Canada, 2014.

[58] J. A. Lozano, M. S. Capovilla, P. V. Trevizoli, K. Engelbrecht, C. R. H. Bahl, J. R. Barbosa Jr., Development of a novel rotary magentic regenerator, International Journal of Refrigeration 68 (2016) 187–197.

[59] A. T. Nakashima, S. L. Dutra, J. R. B. Jr., Experimental evaluation of the flow imbalance in an active magnetic regenerator, in: Proceedings in the 9th World Conference on Experimental Heat Transfer, Fluid Mechanics and Thermodynamics, 2017.

[60] D. Eriksen, K. Engelbrecht, C. R. H. Bahl, R. Bjrk, K. K. Nielsen, A. R. Insinga, N. Pryds, Design and experimental tests of a rotary active magnetic regenerator prototype, International Journal of Refrigeration 58 (2015) 14–21.

[61] R. Teyber, P. V. Trevizoli, I. Niknia, T. V. Christiaanse, P. Govindappa, A. Rowe, Experimental performance investigation of an active magnetic regenerator subject to different fluid flow waveforms, International Journal of Refrigeration 74 (2017) 36–44.

[62] A. Nakashima, G. Hoffmann, J. A. Lozano, J. R. B. Jr., S. L. Dutra, Using electrovalves as a flow distribution system for an active magnetic regenerator, in: Proceedings in the 24th ABCM International Congress of Mechanical Engineering, 2017.

[63] D. Eriksen, K. Engelbrecht, C. R. H. Bahl, R. Bjørk, K. K. Nielsen, Effects of flow balancing on active magnetic regenerator performance, Applied Thermal Engineering 103 (2016) 1–8.

[64] P. V. Trevizoli, M. S. Capovilla, G. Peixer, A. Nakashima, J. Lozano, J. Barbosa, Influence of void volume and inlet flow maldistribution on the performance of thermal regenerators, in: Proceedings in the 7th International Conference on Magnetic Refrigeration at Room Temperature, 2016.

[65] P. V. Trevizoli, G. F. Peixer, A. T. Nakashima, M. S. Capovilla, J. A. Lozano, J. R. B. Jr., Influence of inlet flow maldistribution and carryover losses on the performance of thermal regenerators, Applied Thermal Engineering 133 (2018) 472–482.

[66] J. Lozano, K. Engelbrecht, C. Bahl, K. Nielsen, D. Eriksen, U. Olsen, J. Barbosa Jr., A. Smith, A. Prata, N. Pryds, Performance analysis of a rotary active magnetic refrigerator, Applied Energy 111 (2013) 669 – 680.

[67] A. Rowe, Configuration and performance analysis of magnetic refrigerators, International Journal of Refrigeration 34 (2011) 168–177.

[68] Y. A. ¸Cengel, M. Boles, Thermodynamics: An Engineering Approach, Mcgraw Hill Higher Education, 2006.

[69] A. Bejan, G. Tsatsaronis, M. Moran, Thermal Design and Optimization, John Wiley & Sons, Inc., 1996.

[70] A. Tura, A. Rowe, Concentric halbach cylinder magnetic refrigerator cost, International Journal of Refrigeration 37 (2014) 106–116.

[71] R. Bjørk, C. R. H. Bahl, K. K. Nielsen, The lifetime cost of a magnetic refrigerator, International Journal of Refrigeration 63 (2016) 48–62.

[72] A. Tura, A. Rowe, Permanent magnet magnetic refrigerator design and experimental characterization, International Journal of Refrigeration 34 (2011) 628–639.

[73] S. J. Lee, J. M. Kenkel, V. K. Pecharsky, D. C. Jiles, Permanent magnet array for the magnetic refrigerator, Journal of Applied Physics 91 (2002) 8894–8896.

[74] R. Bjørk, C. R. H. Bahl, A. Smith, N. Pryds, Optimization and improvement of Halbach cylinder design, Journal of Applied Physics 104 (2008) 13910.

[75] P. V. Trevizoli, J. A. Lozano, G. F. Peixer, J. R. Barbosa, Jr., Design of nested Halbach cylinder arrays for magnetic refrigeration applications, Journal of Magnetism and Magnetic Materials 395 (2015) 109–122.

[76] P. V. Trevizoli, J. R. Barbosa, Jr., A. Tura, D. Arnold, A. Rowe, Modeling of thermo-magnetic phenomena in active magnetocaloric regenerators, Journal of Thermal Science and Engineering Applications 6 (2014) 031016.

[77] R. Bjørk, K. Engelbrecht, The influence of the magnetic field on the performance of an active magnetic regenerator (AMR), International Journal of Refrigeration 34 (2011) 192–203.

[78] U. Plaznik, J. Tusek, A. Kitanovski, A. Poredos, Numerical and experimental analyses of different magnetic thermodynamic cycles with an active magnetic regenerator, Applied Thermal Engineering 59 (2013) 52–59.

[79] R. Teyber, P. V. Trevizoli, T. V. Christiaanse, P. Govindappa, I. Niknia, A. Rowe, Experimental evaluation of two-material active magnetic regenerators, in: Proc. 7th Int. Conf. Magn. Refrig. at Room Temp.: THERMAG VII, Turin, Italy, 2016.

[80] S. Ergun, Fluid flow through packed collumn, Chemical Engineering Progress 48 (1952) 89–94.

[81] W. S. Janna, Design of fluid thermal systems, CL-Engineering, 1998.

[82] M. Kaviany, Principles of Heat Transfer in Porous Media, 2nd Edition, Springer, 1995.

[83] I. Niknia, O. Campbell, T. V. Christiaanse, P. Govindappa, R. Teyber, P. V. Trevizioli, A. Rowe, Impacts of configuration losses on active magnetic regenerator device performance, Applied Thermal Engineering 106 (2016) 601–612.

[84] T. R. N. Mhíocháin, D. Weaire, S. M. McMurry, J. M. D. Coey, Analysis of torque in nested magnet cylinders, Journal of Applied Physics 86 (1999) 6412–6424.

[85] J. P. Holman, Experimental Methods for Engineers, eighth Edition, McGraw-Hill, New York, 2006.

[86] G. Nellis, S. Klein, Heat Transfer, Cambridge University Press, 2009.

[87] N. Wakao, S. Kaguei, Heat and mass transfer in packed beds, Gordon and Breach Science, New York, 1982.

[88] B. Yu, M. Liu, P. W. Egolf, A. Kitanovski, A review of magnetic refrigerator and heat pump prototypes built before the year 2010, International Journal of Refrigeration 33 (2010) 1029–1060.

[89] M. A. Richard, A. Rowe, R. Chahine, Magnetic refrigeration: Single and multimaterial active magnetic regenerator experiments, Journal of Applied Physics 95 (2004) 2146–2150.

[90] A. Rowe, A. Tura, Experimental investigation of a three-material layered active magnetic regenerator, International Journal of Refrigeration 29 (2006) 1286–1293.

[91] K. Engelbrecht, C. R. H. Bahl, K. K. Nielsen, Experimental results for a magnetic refrigerator using three different types of magnetocaloric material regenerators, International Journal of Refrigeration 34 (2011) 1132–1140.

[92] J. Tusek, A. Kitanovski, U. Tomc, C. Favero, A. Poredos, Experimental comparison of multi-layered La-Fe-Co-Si and single-layered Gd active magnetic regenerators for use in a room-temperature magnetic refrigerator, International Journal of Refrigeration 37 (2014) 117–126.

[93] O. Campbell, A. Rowe, P. Govindappa, Experimental studies of layered AMRs using $MnFeP_{1-x}As_x$, in: Proceeding in 6th International Conference on Magnetic Refrigeration at Room Temperature (THERMAG VI), Victoria, Canada, 2014.

[94] K. K. Nielsen, C. R. H. Bahl, K. Engelbrecht, A. Smith, N. Pryds, J. Hattel, Numerical modeling of graded active magnetic regenerators, in: Proceeding in 4th International Conference on Magnetic Refrigeration at Room Temperature (THERMAG IV), Baotou, China, 2010.

[95] B. Monfared, B. Palm, Optimization of layered regenerator of a magnetic refrigeration device, International Journal of Refrigeration 57 (2015) 103–111.

[96] T. Burdyny, Simplified modeling of active magnetic regenerators, Master's thesis, University of Victoria (2012).

[97] C. H. Li, B. A. Finlayson, Heat transfer in packed beds - a reevaluation, Chemical Engineering Science 32 (1977) 1055–1066.

[98] K. K. Nielsen, J. Tusek, K. Engelbrecht, S. Schopfer, A. Kitanovski, C. R. H. Bahl, A. Smith, N. Pryds, A. Poredos, Review on numerical modeling of active magnetic regenerators for room temperature applications, International Journal of Refrigeration 34 (2011) 603–616.

[99] P. Govindappa, P. V. Trevizoli, O. Campbell, I. Niknia, T. V. Christiaanse, R. Teyber, M. A. Schwind, D. van Asten, L. Zhang, A. Rowe, Experimental investigation of MnFeP1-xAsx multilayer active magnetic regenerators, Journal of Physics D: Applied Physics. 50 (31) (2017) 315001.

[100] U. Legait, F. Guillou, A. Kedous-lebouc, M. Almanza, An experimental comparison of four magnetocaloric regenerators using three different materials, International Journal of Refrigeration 37 (2014) 147–155.

[101] A. T. Saito, H. Nakagome, Room-temperature magnetic refrigeration: from basic research to development for application, in: Proc. 7th Int. Conf. Magn. Refrig. at Room Temp.: THERMAG VII, Turin, Italy, 2016.

[102] C. Aprea, A. Greco, A. Maiorino, A numerical analysis of an active magnetic regenerative refrigerant system with a multi-layer regenerator, Energy Conversion and Management 52 (2011) 97–107.

[103] I. Park, Y. Kim, J. Park, S. Jeong, Design method of the layered active magnetic regenerator (AMR) for hydrogen liquefaction by numerical simulation, Cryogenics 70 (2015) 57–64.

[104] T. Lei, K. Engelbrecht, K. K. Nielsen, N. N. Bez, C. R. H. Balh, Study of multi-layer active magnetic regenerators using magnetocaloric materials with first and second order phase transition, Journal of Physics D: Applied Physics. 49 (2016) 345001.

[105] J. E. Cararo, J. A. Lozano, P. V. Trevizoli, R. Teyber, A. Rowe, J. R. B. Jr, Optimization of active magnetic regenerators with two and three layers of Gd and Gd-alloys, in: Proc. 7th Int. Conf. Magn. Refrig. at Room Temp.: THERMAG VII, Turin, Italy, 2016.

[106] M. A. Benedict, S. A. Sherif, D. G. Beers, M. Schroeder, A new model of first-order magnetocaloric materials with experimental validation, International Journal of Refrigeration 70 (2016) 138–147.

[107] M. S. Kamran, H. Ali, M. Farhan, Y. B. Tang, Y. G. Chen, H. S. Wang, Performance optimisation of room temperature magnetic refrigerator with layered/multi-material microchannel regenerators, International Journal of Refrigeration 68 (2016) 94–106.

[108] T. E. Oliphant, Python for scientific computing, Computing in Science & Engineering 9 (2007) 10–20.

[109] C. Aprea, A. Maiorino, A flexible numerical model to study an active magnetic refrigerator for near room temperature applications, Applied Energy 87 (2010) 2690–2698.

[110] T. Kawanami, S. Hirano, K. Fumoto, S. Hirasawa, Evaluation of fundamental performance on magnetocaloric cooling with active magnetic regenerator, Applied Thermal Engineering 31 (2011) 1176–1193.

[111] C. Aprea, A. Greco, A. Maiorino, Geothermag: A geothermal magnetic refrigerator, International Journal of Refrigeration 59 (2015) 75–83.

[112] P. V. Trevizoli, A. T. Nakashima, J. R. Barbosa Jr., Performance evaluation of an active magnetic regenerator for cooling applications - Part II: Mathematical

modeling and thermal losses, International Journal of Refrigeration 72 (2016) 206–217.

[113] J. Tusek, A. Kitanovski, I. Prebil, A. Poredos, Dynamic operation of an active magnetic regenerator (AMR): Numerical optimization of a packed-bed AMR, International Journal of Refrigeration 34 (2011) 1507–1517.

[114] C. Aprea, A. Greco, A. Maiorino, An application of the artificial neural network to optimise the energy performances of a magnetic refrigerator, International Journal of Refrigeration 82 (2017) 238–251.

[115] A. Rowe, Thermodynamics of active magnetic regenerators: Part I, Cryogenics 52 (2012) 111–118.

[116] A. Rowe, Thermodynamics of active magnetic regenerators: Part II, Cryogenics 52 (2012) 119–128.

[117] T. Burdyny, D. Arnold, A. Rowe, AMR thermodynamics: Semi-analytic modeling, Cryogenics 62 (2014) 177–184.

[118] J. M. D. Coey, Magnetism and magnetic materials, Cambridge University Press, 2010.

[119] M. Sato, Y. Ishii, Simple and approximate expressions of demagnetizing factors of uniformly magnetized rectangular rod and cylinder, Journal of Applied Physics 66 (1989) 983–985.

[120] S. M. Benford, G. V. Brown, T-S diagram for gadolinium near the curie temperature, Journal of Applied Physics 52 (1981) 2110–2112.

[121] A. Rowe, T. V. Christiaanse, P. Govindappa, I. Niknia, R. Teyber, P. V. Trevizoli, Active caloric regenerator cycles: an analytic element model, in: Proc. 7th Int. Conf. Magn. Refrig. at Room Temp.: THERMAG VII, Turin, Italy, 2016.

[122] D. J. Durbin, C. Malardier-Jugroot, Review of hydrogen storage techniques for on board vehicle applications, International Journal of Hydrogen Energy 38 (2013) 14595–14617.

[123] R. Barron, Cryogenic Systems, 2nd Edition, Oxford University Press, 1985.

[124] T. Numazawa, K. Kamiya, T. Utaki, K. Matsumoto, Magnetic refrigerator for hydrogen liquefaction, Cryogenics 62 (2014) 185–192.

[125] R. Teyber, P. V. Trevizoli, T. V. Christiaanse, P. Govindappa, I. Niknia, A. Rowe, Semi-analytic AMR element model, Applied Thermal Engineering 128 (2018) 1022–1029.

[126] C. B. Zimm, J. W. Johnson, R. W. Murphy, Test results on a 50 K magnetic refrigerator, Advances in Cryogenic Engineering 41 (1996) 1675–1682.

[127] A. Rowe, A. Tura, Cryogenic testing of an active magnetic regenerative refrigerator, AIP Conference Proceedings 985 (2008) 1292–1298.

[128] J. A. Barclay, K. Oseen-Senda, L. Ferguson, A. Cousins, J. Pouresfandiary, H. Ralph, T. Hampton, Active Magnetic Regenerative Liquefier, Final Report (2016), DOE Design Award Number: DE-FG36-08GO18064.

[129] J. A. Barclay, M. Schneider, C. R. Cross, F. C. Prenger, W. F. Stewart, C. B. Zimm, Design limitations on magnetic refrigerators imposed by magnetic forces, in: Proc. 4th Int. Cryocooler Conf., Vol. Easten, MD, 1986.

[130] A. M. Rowe, J. A. Barclay, Static and dynamic force balancing in reciprocating active magnetic refrigerators, AIP Conference Proceedings 613 (2002) 1003–1010.

[131] O. Peksoy, A. Rowe, Demagnetizing effects in active magnetic regenerators, Journal of Magnetism and Magnetic Materials 288 (2005) 424–432.

[132] A. Rowe, A. Tura, Active magnetic regenerator performance enhancement using passive magnetic materials, Journal of Magnetism and Magnetic Materials 320 (2008) 1357–1363.

[133] A. Mira, T. de Larochelambert, C. Espanet, S. Giurgea, P. Nika, C. R. H. Bahl, R. Bjørk, K. K. Nielsen, Influence of magnetization on the applied magnetic field in various AMR regenerators, Journal of Applied Physics 122 (2017) 133901.

[134] K. Kamiya, T. Numazawa, K. Matsumoto, H. Nozawa, T. Yanagitani, Design and Build of Magnetic Refrigerator for Hydrogen Liquefaction, AIP Conference Proceedings 823 (2006) 591–597.

[135] F. Allab, A. Kedous-Lebouc, J. P. Yonnet, J. M. Fournier, A magnetic field source system for magnetic refrigeration and its interaction with magnetocaloric material, International Journal of Refrigeration 29 (2006) 1340–1347.

[136] M. Balli, C. Mahmed, P. Bonhôte, O. Sari, On the magnetic forces in magnetic cooling machines: Numerical calculations and experimental investigations, IEEE Transactions on Magnetics 47 (10) (2011) 3383–3386.

[137] S. Gama, L. D. R. Ferreira, C. V. X. Bessa, O. Horikawa, A. A. Coelho, F. C. Gandra, R. Araujo, P. W. Egolf, Analytic and Experimental Analysis of Magnetic Force Equations, IEEE Transactions on Magnetics 52 (7) (2016) 9401504.

[138] K. J. Meessen, J. J. H. Paulides, E. A. Lomonova, Force calculations in 3-D cylindrical structures using fourier analysis and the maxwell stress tensor, IEEE Transactions on Magnetics 49 (1) (2013) 536–545.

[139] A. Kitanovski, P. W. Egolf, Thermodynamics of magnetic refrigeration, International Journal of Refrigeration 29 (2006) 3–21.

[140] S. Y. Dan´kov, A. M. Tishin, V. K. Pecharsky, K. A. Gschneidner, Jr., Magnetic phase transitions and the magnetothermal properties of gadolinium, Physical Review B 57 (1998) 3478–3490.

[141] P. Kittel, Eddy current heating in magnetic refrigeration, Advances in Cryogenic Engineering 35 (1990) 1141–1148.

[142] O. Gutfleisch, M. A. Willard, E. Brück, C. H. Chen, S. G. Sankar, J. P. Liu, Magnetic materials and devices for the 21st century: Stronger, lighter and more energy efficient, Advanced Materials 23 (2011) 821–842.

[143] M. J. Kramer, R. W. McCallum, I. A. Anderson, S. Constantinides, Prospects for non-rare earth permanent magnets for traction motors and generators, Jom 64 (7) (2012) 752–763.

[144] U.S. DOE Critical Materials Strategy (2011).
URL https://www.energy.gov/policy/downloads/2011-critical-materials-strategy

[145] J. M. Coey, Permanent magnets: Plugging the gap, Scripta Materialia 67 (6) (2012) 524–529.

[146] J. M. Coey, New permanent magnets; Manganese compounds, Journal of Physics: Condensed Matter 26 (6) (2014) 064211.

[147] Y. L. Ma, X. B. Liu, K. Gandha, N. V. Vuong, Y. B. Yang, J. B. Yang, N. Poudyal, J. Cui, J. P. Liu, Preparation and magnetic properties of MnBi-based hard/soft composite magnets, Journal of Applied Physics 115 (2014) 17A755.

[148] H. Jian, K. P. Skokov, O. Gutfleisch, Microstructure and magnetic properties of Mn-Al-C alloy powders prepared by ball milling, Journal of Alloys and Compounds 622 (2015) 524–528.

[149] K. Skokov, O. Gutfleisch, Heavy rare earth free, free rare earth and rare earth free magnets - Vision and reality, Scripta Materialia (2018) Article in press.

[150] K. Binnemans, P. T. Jones, B. Blanpain, T. V. Gerven, Y. Yang, A. Walton, M. Buchert, Recycling of rare earths: a critical review, Journal of Cleaner Production 51 (2013) 1–22.

[151] J. D. Widmer, R. Martin, M. Kimiabeigi, Electric vehicle traction motors without rare earth magnets, Sustainable Materials and Technologies 3 (2015) 7–13.

[152] J. R. Riba, C. López-Torres, L. Romeral, A. Garcia, Rare-earth-free propulsion motors for electric vehicles: A technology review, Renewable and Sustainable Energy Reviews 57 (2016) 367–379.

[153] S. J. Galioto, P. B. Reddy, A. M. EL-Refaie, Effect of magnet types on performance of high speed spoke interior permanent magnet machines designed for traction applications, 2014 IEEE Energy Conversion Congress and Exposition, ECCE 2014 51 (3) (2014) 4513–4522.

[154] S. Morimoto, S. Ooi, Y. Inoue, M. Sanada, Experimental evaluation of a rare-earth-free PMASynRM with ferrite magnets for automotive applications, IEEE Transactions on Industrial Electronics 61 (10) (2014) 5749–5756.

[155] H. Cai, B. Guan, L. Xu, Low-cost ferrite PM-assisted synchronous reluctance machine for electric vehicles, IEEE Transactions on Industrial Electronics 61 (10) (2014) 5741–5748.

[156] P. Zhang, G. Y. Sizov, D. M. Ionel, N. A. O. Demerdash, Establishing the relative merits of interior and spoke-type permanent-magnet machines with ferrite or NdFeB through systematic design optimization, IEEE Transactions on Industry Applications 51 (4) (2015) 2940–2948.

[157] H. A. Khazdozian, R. L. Hadimani, D. C. Jiles, Development of rare earth free permanent magnet generator using Halbach cylinder rotor design, Renewable Energy 112 (2017) 84–92.

[158] J. H. Jensen, M. G. Abele, Maximally efficient permanent magnet structures, Journal of Applied Physics 79 (1996) 1157–1163.

[159] R. Bjørk, The ideal dimensions of a Halbach cylinder of finite length, Journal of Applied Physics 109 (2011) 013915.

[160] Z. Zhu, D. Howe, Halbach permanent magnet machines and applications: a review, IEE Proceedings - Electric Power Applications 148 (4) (2001) 299–308.

[161] G. Moresi, R. Magin, Miniature permanent magnet for table-top NMR, Concepts in Magnetic Resonance Part B: Magnetic Resonance Engineering 19 (2003) 35–43.

[162] H. Raich, P. Blümler, Design and construction of a dipolar Halbach array with a homogeneous field from identical bar magnets: NMR mandhalas, Concepts in Magnetic Resonance Part B: Magnetic Resonance Engineering 23 (2004) 16–25.

[163] J. Chen, C. Xu, An improved discrete configuration of a cylinder magnet for portable nuclear magnetic resonance instruments, Journal of Applied Physics 101 (2007) 123926.

[164] R. Bjørk, C. R. H. Bahl, A. Smith, D. V. Christensen, N. Pryds, An optimized magnet for magnetic refrigeration, Journal of Magnetism and Magnetic Materials 322 (2010) 3324–3328.

[165] A. R. Insinga, C. R. H. Bahl, R. Bjørk, A. Smith, Performance of Halbach magnet arrays with finite coercivity, Journal of Magnetism and Magnetic Materials 407 (2015) 369–376.

[166] R. Bjørk, A. Smith, C. R. Bahl, The efficiency and the demagnetization field of a general Halbach cylinder, Journal of Magnetism and Magnetic Materials 384 (2015) 128–132.

[167] L. Li, A. Tirado, I. C. Nlebedim, O. Rios, B. Post, V. Kunc, R. R. Lowden, E. Lara-Curzio, R. Fredette, J. Ormerod, T. A. Lograsso, M. P. Paranthaman, Big Area Additive Manufacturing of High Performance Bonded NdFeB Magnets, Scientific Reports 6 (2016) 36212.

[168] C. Huber, C. Abert, F. Bruckner, M. Groenefeld, I. Teliban, C. Vogler, D. Suess, Topology Optimized and 3D Printed Polymer Bonded Permanent Magnets for a Predefined External Field, Journal of Applied Physics 122 (2017) 053904.

[169] P. Tenaud, A. Morel, F. Kools, J. M. Le Breton, L. Lechevallier, Recent improvement of hard ferrite permanent magnets based on La-Co substitution, Journal of Alloys and Compounds 370 (2004) 331–334.

[170] N. Poudyal, X. Liu, W. Wang, V. V. Nguyen, Y. Ma, K. Gandha, K. Elkins, J. P. Liu, K. Sun, M. J. Kramer, J. Cui, Processing of MnBi bulk magnets with enhanced energy product, AIP Advances 6 (2016) 056004.

[171] T. Saito, Magnetic properties of Mn-Al-C alloy powders produced by mechanical grinding, Journal of Applied Physics 97 (2005) 10F304.

[172] W. Lu, J. Niu, T. Wang, K. Xia, Z. Xiang, Y. Song, H. Zhang, S. Yoshimura, H. Saito, Low-energy mechanically milled τ-phase MnAl alloys with high coercivity and magnetization, Journal of Alloys and Compounds 675 (2016) 163–167.

[173] S. Jin, G. Y. Chin, Fe-Cr-Co magnets, IEEE Transactions on Magnetics 23 (5) (1987) 3187–3192.

[174] C. R. H. Bahl, K. Engelbrecht, D. Eriksen, J. A. Lozano, R. Bjørk, G. Jørgen, K. Nielsen, A. Smith, N. Pryds, Development and experimental results from a 1 kW prototype AMR, International Journal of Refrigeration 37 (2014) 78–83.

[175] S. L. Russek, C. B. Zimm, Potential for cost effective magnetocaloric air conditioning systems, International Journal of Refrigeration 29 (2006) 1366–1373.

[176] D. Vuarnoz, A. Kitanovski, C. Gonin, Y. Borgeaud, M. Delessert, M. Meinen, P. W. Egolf, Quantitative feasibility study of magnetocaloric energy conversion utilizing industrial waste heat, Applied Energy 100 (2012) 229–237.

[177] R. Bjørk, A. Smith, C. R. H. Bahl, N. Pryds, Determining the minimum mass and cost of a magnetic refrigerator, International Journal of Refrigeration 34 (2011) 1805–1816.

[178] R. Bjørk, C. R. H. Bahl, A. Smith, N. Pryds, Improving magnet designs with high and low field regions, IEEE Transactions on Magnetics 47 (6) (2011) 1687–1692.

[179] A. R. Insinga, R. Bjørk, A. Smith, C. R. H. Bahl, Optimally segmented permanent magnet structures, IEEE Transactions on Magnetics 52 (12) (2016) 7210306.

[180] A. Barcza, Vacuumschmelze GmbH & Co. KG (2016), Personal Communication.

[181] B. Monfared, R. Furberg, B. Palm, Magnetic vs. vapour-compression household refrigerators: A preliminary comparative life cycle assessment, International Journal of Refrigeration 42 (2014) 69–76.

[182] K. Habib, H. Wenzel, Exploring rare earths supply constraint for the emerging clean energy technologies and the role of recycling, Journal of Cleaner Production 84 (2014) 348–359.

[183] K. Engelbrecht, G. Nellis, S. Klein, Predicting the performance of an active magnetic regenerator refrigerator used for space cooling and refrigeration, HVAC&R Research 12 (5) (2006) 1077–1095.

[184] S. Roy, S. Poncet, M. Sorin, Sensitivity analysis and multiobjective optimization of a parallel-plate active magnetic regenerator using a genetic algorithm, International Journal of Refrigeration 75 (2017) 276–285.

[185] J. Dikeos, A. Rowe, Validation of an active magnetic regenerator test apparatus, International Journal of Refrigeration 36 (2013) 921–931.

[186] C. Aprea, G. Cardillo, A. Greco, A. Maiorino, C. Masselli, A comparison between experimental and 2d numerical results of a packed-bed active magnetic regenerator, Applied Thermal Engineering 90 (2015) 376–383.

[187] T. Burdyny, A. Ruebsaat-Trott, A. Rowe, Performance modeling of AMR refrigerators, International Journal of Refrigeration 37 (2014) 51–62.

[188] J. Dikeos, Development and validation of an active magnetic regenerator refrigeration cycle simulation, Master's thesis, University of Victoria (2006).

[189] K. Engelbrecht, A numerical model of an active magnetic regenerator refrigerator with experimental validation, Ph.D. thesis, University of Wisconsin-Madison (2008).

[190] COMSOL Multiphysics v. 5.2. (2017).
URL www.comsol.com